UNIVERSITY OF CALIFORNIA,
IRVINE

Raman Based Dispersive Systems for Short Pulse Generation and Optical Signal Processing

DISSERTATION

submitted in partial satisfaction of the requirements
for the degree of

DOCTOR OF PHILOSOPHY

in Electrical and Computer Engineering

by

Salih Kagan Kalyoncu

Dissertation Committee:
Associate Professor Ozdal Boyraz, Chair
Associate Professor Filippo Capolino
Associate Professor Gultekin Gulsen

2013

TABLE OF CONTENTS

LIST OF FIGURES

LIST OF TABLES

ACKNOWLEDGMENTS

I would like to express the deepest appreciation to my committee chair Professor Ozdal Boyraz, who has the attitude and the substance of a genius: he continually and convincingly conveyed a spirit of adventure in regard to research and scholarship, and an excitement in regard to teaching. Without his guidance and persistent help this dissertation would not have been possible.

I would like to thank my committee members, Professor Filippo Capolino and Professor Gultekin Gulsen, whose work demonstrated to me that concern for global affairs supported by an “engagement” in comparative literature and modern technology should always transcend academia and provide a quest for our times.

I gratefully acknowledge the research fellowship received from the Scientific and Technological Research Council of Turkey (TUBITAK) for the first 2 years towards my PhD.

I would like to show my gratitude to many of my colleagues, En Kuang Tien, Feng Qian, Qi Song, and Yuewang Huang, who helped me in many ways.

In addition, special thanks to my lovely wife Guldane Durukan Kalyoncu and my parents Ikram Kalyoncu and Raziye Kalyoncu, my sister Sule Kalyoncu, for supporting and encouraging me to pursue this degree. Without their guidance and continuous help this thesis would not have been possible.

CURRICULUM VITAE

SALIH KAGAN KALYONCU

EDUCATION

Doctor of Philosophy in Electrical and Computer Engineering **January, 2013**
University of California Irvine *Irvine, California*

Master of Science in Electrical Engineering **June, 2010**
University of California Irvine *Irvine, California*

Bachelor of Science in Electrical Engineering **June 2008**
Bogazici University *Istanbul , Turkey*

RESEARCH EXPERIENCE

Graduate Student Researcher **2008-2012**
APDSL Laboratory
University of California Irvine *Irvine, California*

REFEREED JOURNAL PUBLICATIONS

J1. **Salih K. Kalyoncu**, Yuewang Huang, Qi Song and Ozdal Boyraz, "Fast arbitrary waveform generation by using digital micro mirror arrays", (IEEE Photonics Journal, 2013, in print).
J2. **Salih K. Kalyoncu**, Yuewang Huang, Qi Song and Ozdal Boyraz, "Analytical study on arbitrary waveform generation by MEMS micro-mirror arrays", Optics Express, Vol.20, No. 25 (2012).
J3. **Salih K. Kalyoncu**, Shiming Gao, En-Kuang Tien, Yuewang Huang, Dogukan Yildirim, Enver Adas, Stefan Wabnitz and Ozdal Boyraz, "Stability analysis of pulsed cascaded Raman lasers in dispersion-managed systems", J. Opt. Soc. Am. B / Vol. 28, No. 11 / November 2011.
J4. Y. Huang, E. K. Tien, S. Gao, **Salih K. Kalyoncu**, Q. Song, F. Qian, E. Adas, D. Yildirim and O. Boyraz, "Electrical signal-to-noise ratio improvement in indirect detection of mid-IR signals by wavelength conversion in silicon-on-sapphire waveguides", Applied Physics Letters, Vol.99, Issue: 18/181122, DOI: 10.1063/1.3651292, Published: OCT 31 2011.
J5. Feng Qian, Qi Song, En-Kuang Tien, **Salih K. Kalyoncu**, Yuewang Huang, and Ozdal Boyraz, "Effects of Design Geometries and Nonlinear Losses on Gain in Silicon Waveguides with Erbium-Doped Regions", IEEE JOURNAL OF QUANTUM ELECTRONICS, VOL. 47, NO. 3 MARCH 2011.

J6. Shiming Gao, En-Kuang Tien, Qi Song, Yuewang Huang, **Salih K. Kalyoncu**, Ozdal Boyraz "Experiment of C-band wavelength conversion in a silicon waveguide pumped by dispersed femtosecond laser pulse", Chin. Phys. Lett., 2010, 27.

J7. En-Kuang Tien, Yuewang Huang, Shiming Gao, Qi Song, Feng Qian, **Salih K. Kalyoncu**, and Ozdal Boyraz, "Discrete parametric band conversion in silicon for mid-infrared applications", 11 October 2010 / Vol. 18, No. 21 / OPTICS EXPRESS.

J8. Feng Qian, Qi Song, En-Kuang Tien, **Salih K. Kalyoncu**, Ozdal Boyraz "Real-time optical imaging and tracking of micron-sized particles", Optics Communications 282 (2009) 4672–4675

REFEREED CONFERENCE PUBLICATIONS

C1. **Salih K. Kalyoncu**, Yuewang Huang, Qi Song and Ozdal Boyraz, "Fast arbitrary waveform generation by using digital micro mirror arrays", IEEE Photonics Conference, TuK4, San Francisco 2012.

C2. Y. Huang, **S. K. Kalyoncu**, Q. Song, and O. Boyraz, "Silicon-on-sapphire Waveguides Design for Mid-IR Evanescent Field Absorption Gas Sensors," in CLEO: Applications and Technology, OSA Technical Digest (online) (Optical Society of America, 2012), paper JW2A.122.

C3. Shiming Gao, Lizhong Cao, En-Kuang Tien, Yuewang Huang, Qiang Liu, Qi Song, **Salih K. Kalyoncu**, Sailing He, Boyraz Ozdal, "Two-pump four-wave mixing in silicon waveguides for broadband wavelength conversion", Proceedings of the SPIE, Vol. 8120 pp. 81200O , 2011.

C4. Yuewang Huang, En-Kuang Tien, Shiming Gao, **Salih K. Kalyoncu**, Qi Song, Feng Qian, Ozdal Boyraz, Quasi-phase matching in SOI and SOS based parametric wavelength converters", Proceedings of the SPIE, Vol. 8120 pp. 81200F , 2011.

C5. Y. Huang, **S. K. Kalyoncu**, E. K. Tien, S. Gao, Q. Song, F. Qian, E. Adas, D. Yildirim and O. Boyraz, "eSNR improvement in indirect detection of mid-IR signals by wavelength conversion in SOS waveguides", Proc. SPIE 8155, 81550U (2011)

C6. **Salih K. Kalyoncu**, Yuewang Huang, En-Kuang Tien, Adas E.,Yildirim D., Ozdal Boyraz, "Noise Performance of Time Stretch System with Distributed and Discrete Amplifiers", in CLEO:2011 - Laser Applications to Photonic Applications, OSA Technical Digest (CD) (Optical Society of America, 2011), paper CTuA7.

C7. **Salih K. Kalyoncu**, Shiming Gao, En-Kuang Tien, Yuewang Huang, Yildirim, D., Adas, E., Wabnitz, S., Ozdal Boyraz, "Stability analysis of second order pulsed Raman laser in dispersion managed systems", Proceedings of the SPIE, Vol. 8071 pp. 807116 , 2011

C8. En-Kuang Tien, Feng Qian, Qi Song, **Salih K. Kalyoncu**, Yuewang Huang, Ozdal Boyraz, "Discrete parametric band conversion in silicon for mid-infrared applications", Conference on Optical Fiber Communication OFC/NFOEC Pages: 3 pp. Published: 2010.

ABSTRACT OF THE DISSERTATION

Raman Based Dispersive Systems for Short Pulse Generation and

Optical Signal Processing

By

Salih Kagan Kalyoncu

Doctor of Philosophy in Electrical and Computer Engineering

University of California, Irvine, 2013

Associate Professor Ozdal Boyraz, Chair

Spatiotemporal dispersive systems have been widely utilized for nonlinear optics and optical signal processing applications. This thesis is dedicated to the investigation of dispersive and nonlinear properties of optical fibers, temporal dispersion for real time operation and spatially dispersed pulse shaping systems. In particular, this thesis is focused on Raman based dispersive systems based on such promising techniques as dispersion management, photonic time stretching and space-to-wavelength mapping for synchronous pulse generation and all-optical RF arbitrary waveform generation incorporated with mature MEMS technology.

The first part of this thesis discusses a novel technique of using dispersion managed system for synchronous first and second order pulsed Raman lasers that can achieve frequency spacing of up to 1000 cm^{-1}, which are widely utilized for CARS microscopy applications. In particular, I focus on analytical and numerical analysis of pulsed stability derived for Raman lasers by using dispersion-managed telecom fibers and pumping at near 1530 nm telecom wavelengths. I show the evolution of the first and second order Stokes signals at the output for

different peak pump power and the net anomalous dispersion combinations. I determine the stability condition for dispersion-managed synchronous Raman lasers up to second order.

In the second part of the thesis, the noise performance of the amplified time stretched systems is investigated. Amplified time stretched systems enabling real time applications such as high-speed analog-to-digital converters, RF arbitrary waveform generation and dispersive imaging are performance limited by the noise cumulated in the system. In particular, I analyze the noise performance and hence the effective number of bits (ENOB) performance of time stretch ADCs with distributed and lumped amplifications. I estimate that distributed amplification in time stretch system with >10GHz analog bandwidth exhibit up to 16dB higher SNR corresponding to ~2.5 bit higher resolution.

The last part of the thesis introduces a novel technique of using MEMS based digital micro mirror technology as a digital spatial light modulator for fast programmable all-optical RF arbitrary waveform generation. In particular, the detailed procedure is described and the analytical modeling that discusses the limits of the proposed technique in terms achievable temporal resolution, repetition rate, modulation index and the rise/fall times of the final waveform is calculated as figure of merit. Experimental generation of square and sawtooth waveforms is demonstrated as a proof-of concept. By using the state of the art MEMS technology arbitrary waveforms up to 1GHz rate and reconfigurable in ~30µs are achievable.

INTRODUCTION

The advent of low loss silica fibers, <0.2dB/km near 1550nm [1] which is limited by the fundamental Rayleigh scattering, has revolutionized the field of optical fiber communication and led to the development of the new field of nonlinear fiber optics [2-3]. Optical fibers exhibit various nonlinear and linear phenomena such as Kerr effect and Raman effect, and the chromatic dispersion, which result from the intensity and the frequency dependency of the refractive index of the dielectric material (silica), and stimulated inelastic scattering, respectively.

In particular chromatic dispersion is the phenomenon in which the index of refraction changes with the frequency, namely emphasizing the wavelength dependency of the group-velocity [4]. Any medium or system with such characteristics is called dispersive medium or system. Material and waveguide dispersions are the two main sources of dispersion, which results from the frequency dependent response of the material and the geometrical structure of the medium, respectively [5]. Dispersion can be observed either in free space in the form of spatial separation of different wavelength components by prisms or diffraction gratings; or in optical fibers as temporal broadening of ultrafast pulses.

The nonlinear phenomena in fibers result from the nonlinear response of the dielectric to the intense electromagnetic fields. The anharmonic motion of the bound electrons under the influence of applied field causes nonlinear response of total polarization [6-9]. Due to the inversion symmetry of the silica (SiO_2), the lowest order nonlinear effects in optical fibers arise from the third order susceptibility (χ^3), which causes such nonlinear effects as third-harmonic generation, four wave mixing (FWM) and nonlinear refraction [7]. The parametric wave mixing processes, however, require phase matching conditions which are not efficient in optical fibers. The major nonlinear effects in silica optical fibers, therefore, derive from the nonlinear refraction, which attribute to the intensity dependency of the refractive index change characterized by the nonlinear-index coefficient (n_2) typically 2.7×10^{-16} cm^2/W [10]. Self-phase modulation (SPM) and the cross-phase modulation (XPM) are the two main nonlinear effects occur in silica fibers based on the self-induced intensity dependent phase shift and asymmetric phase shift due to other fields with different wavelength, different polarization and direction, respectively. These nonlinear phase shift effects lead to the pulse compression [11], spectral broadening and soliton formation [12].

A second class of fiber nonlinearity in fibers relays on the inelastic scattering. Contrary to such elastic nonlinear effects as SPM and XPM where the optical field energy is preserved, a part of energy is exchanged between the optical field and the dielectric material in inelastic scattering according to vibrational excitation states of the dielectric. Stimulated Raman scattering (SRS) and the stimulated Brillion scattering (SBS) are the two main inelastic nonlinear scattering phenomena observed in optical fibers [13-15]. In a quantum mechanical approach, the excited electrons of the dielectric material by incident photons of the optical field reemit photons at lower frequency. The residual energy is emitted as either acoustic phonons in SBS or optical phonons in SRS to preserve the total energy and momentum. In fibers, stimulated Raman scattering has a wide gain bandwidth extending up to ~30THz with a peak gain $g_R \approx 7\times10^{-14}$m/W and peak frequency shift of 13.5THz at pump wavelength near 1550nm [12]. Raman scattering with the advantage of its being obtained in any nonlinear medium at any wavelength by synchronous pumping, can act as a suitable gain mechanism and laser source. Raman amplifiers [16-19] and Raman lasers [20-23] have been demonstrated in silica fibers and have great potential for wavelength tunable, cost efficient, flexible amplifiers and lasers. In recent years, Raman fiber lasers have retrieved strong interest due to their capability of serving as pump sources in gain-flattened amplifiers for optical communication systems and as widely tunable sources to characterize the optical devices at longer wavelengths.

The dispersive effects in optical fibers, which treat them as a linear medium, mainly originate from the frequency dependency of the dielectric material, namely material dispersion. The bound electrons of the dielectric oscillate at specific resonance frequencies which cause the medium response depends on the optical frequency [24]. Briefly, the refractive index becomes a function of optical frequency, which causes different spectral components travel at different speeds inside the fiber causing temporal broadening, namely called the chromatic dispersion. Chromatic dispersion is characterized by the group velocity dispersion (GVD), which defines the change in the group velocity with respect to wavelength.

The GVD plays a crucial factor in degradation of the bit rate-distance product (i.e. capacity per km) of communication systems and leads to a walk-off effect that prevents the synchronous propagation (this leads to weaker nonlinear interaction) of ultrafast pulses at different wavelengths [25]. Various types of fibers such as dispersion shifted [26] (adjusting the zero dispersion wavelength near 1550nm) and dispersion flattened [27] fibers providing broadband, uniform, low dispersion profiles have been engineered for the dispersion compensation especially for single channel communication systems. However, for the dense wavelength-division-multiplexed systems, cascaded laser systems or the parametric wave mixing applications, GVD still becomes a serious concern. The technique of dispersion management via combining different fibers with different dispersion profiles to compensate the average dispersion over the broadband spectral window provides an excellent solution to this dilemma [28].

Despite the detrimental effects of dispersion, on the other hand, GVD can be utilized for pulse compression especially in soliton formation via interplay with the nonlinear effects in fibers and photonic time stretching concept based on time-to-wavelength mapping in which each frequency component corresponds to a different temporal point across the pulse to realize real-time operation using a single-detector and single-shot measurement. The photonic time stretching is a novel technique that can slow down, amplify, and capture fast events [29-30]. The second part of this dissertation focuses on the concept of photonic time-stretch technique and its applications to real-time high-speed instrumentation. Real-time instrumentation is highly desired for wide range of fields varying from industrial and scientific to medical applications enabling detection and diagnostics of transient and rare-occurring events with fine time resolution and long record length. In the context of optics, for example, real-time instruments are required to capture especially non-repetitive high frequency RF signals, calibration of fast transient errors in optical communication systems and metastatic cancer cells in biological imaging systems [31]. It provides a functional tool for many applications such as analog-to-digital conversion [29-30], optical arbitrary waveform generation, spectroscopy [32] and imaging [33-35].

The second category of dispersive systems is based on the spatial dispersion. Similar to time stretching and time-to-wavelength mapping analogy, the spatial dispersion is based on the space-wavelength mapping technique in which different spectral components are directed to different lateral spatial positions. The light beams such as the ultra short laser pulses which are represented in time domain and frequency domain via Fourier transform, can be processed in optical domain via different open loop or closed loop schemes. The pulse shaping in terms of such optical pulse properties as the phase, amplitude and the polarization can be manipulated either in the frequency or time domain. Space wavelength mapping achieved by dispersing broadband optical source by using diffractive optical elements such as prisms and diffraction gratings in a 4-f zero-dispersion configuration provides a successful technique for frequency domain processing [36-37]. The wavelength information mapped over the Fourier plane can be directly intensity and phase modulated in spatial domain by using spatial light modulators (SLM). Digital spatial light modulators provide pixelated structure, allowing 2D light modulation by controlling the individually addressable pixels arrays each of which can individually control the phase or amplitude of light in a transmission or reflective manner. Based on the physical principles they work, various types of SLMs such as most widely used a liquid crystal display (LCD) [37-39] which reorients the long-stretched liquid crystal molecules between the two glass plates to modulate the refractive index for transmitted light, acousto-optical modulator (AOM) [40-41] which modulates the light by an acoustic wave in an appropriate crystal, deformable mirrors rotated by piezo stage motors [42] and micro-machined mirror arrays [43-44] have been proposed. Both time-to-wavelength mapping and the space-to-wavelength mapping techniques can be cooperated in the same system to achieve space-time-wavelength mapping to provide real-time optical signal processing applications such as spectroscopy, optical arbitrary waveform generation and fastest optical imaging applications.

This thesis summarizes my research of nonlinear fiber optics and microwave photonics emphasizes on Raman based dispersive systems for short pulse and RF arbitrary waveform generation. I propose a novel dispersion managed system for pulsed cascaded Raman laser with ~1000cm^{-1} frequency separation. The walk-off penalty due to group velocity dispersion (GVD) that limits the synchronous propagation of higher order Stokes pulses is engineered by using dispersion managed cavity. In addition, I study the noise performance of amplified time stretch systems with discrete and distributed amplification. Finally, I propose a novel method for fast all-optical RF arbitrary waveform generation by using MEMS based digital micro mirror technology.

The organization of this thesis is as follows: chapter 1 provides an analytical model of the linear and nonlinear interactions in fibers including the group-velocity dispersion (GVD), self-phase modulation (SPM), cross phase modulation (XPM) and the stimulated Raman scattering (SRS) effects. A novel cascaded fiber Raman laser system up to second order by using dispersion-managed cavity is proposed and investigated numerically in chapter 2. A powerful variational analysis as an alternative to time consuming numerical simulations is conducted to analytically investigate the intra-cavity pulse dynamics. In addition, a detailed stability analysis is carried to obtain the contours for achievable second Stokes pulse parameters. In chapter 3, I study the amplified time stretch systems utilized for such many applications as all-optical analog to digital converter, real time dispersive imaging and RF arbitrary waveform generation. A detailed and comparative noise performance analysis is conducted for both discrete and distributed amplification cases. In chapter 4, a novel method for fast all-optical RF arbitrary waveform generation is proposed and experimentally demonstrated by using MEMS based digital micro mirror device (DMD). Additionally, an analytical study that describes the detailed procedure is conducted to investigate the limits of the proposed system.

CHAPTER 1

Nonlinear interactions in fibers and theory of Raman

The optical pulses while propagating inside a fiber are influenced by both linear dispersive and nonlinear effects. Fiber as a dielectric dispersive medium becomes nonlinear especially for intense pulses with high peak power and short pulse duration ranging from ~10ns to 10fs. Both nonlinear and the dispersive effects cause changes in pulse shape and spectra. The propagation of the optical field as an electromagnetic wave inside the fiber is governed by Maxwell's equations [4,45].

$$\nabla\times E = -\frac{\partial B}{\partial t} \tag{1.1a}$$

$$\nabla\times H = \mathcal{J} + \frac{\partial D}{\partial t} \tag{1.1b}$$

$$\nabla\cdot \mathrm{D} = \rho_f \tag{1.1c}$$

$$\nabla\cdot \mathrm{B} = 0 \tag{1.1d}$$

where E and H are the electric and the magnetic field vectors; D and B are the electric and the magnetic flux densities that are related to corresponding fields vectors through such equations:

$$\begin{gathered} D = \varepsilon_0 E + P \\ B = \mu_0 H + M \end{gathered} \tag{1.2}$$

where ε_0 is the electric permittivity and μ_0 is the vacuum permeability which are related as $\varepsilon_0\mu_0 = \frac{1}{c^2}$. P and M are the induced electric and magnetic polarization vectors, respectively. Since the fiber is a non-magnetic medium ($M = 0$) absence of free charges ($\rho_f = 0$) and free current ($\mathcal{J}$

=0). Substituting Eq. (1.2) into Maxwell's equations and taking the curl of Eq. (1.1a), the wave equation that describes the propagation of light inside the fiber can be obtained as:

$$\nabla^2 E(r,t) - \frac{1}{c^2}\frac{\partial^2 E(r,t)}{\partial t^2} = \mu_0 \frac{\partial^2}{\partial t^2}[P_L(r,t) + P_{NL}(r,t)] \tag{1.3}$$

where $P_L$and P_{NL} are the linear and the nonlinear parts of the induced electric polarization defined as:

$$\begin{gathered} P_L(r,t) = \varepsilon_0 \int_{-\infty}^{\infty} \chi^{(1)}(t-t')E(r,t')dt' \\ P_{NL}(r,t) = \varepsilon_0 \left[\iint_{-\infty}^{\infty} \chi^{(2)}(t-t')E^2(r,t')dt' + \iiint_{-\infty}^{\infty} \chi^{(3)}(t-t')E^3(r,t')dt' + \cdots \right. \end{gathered} \tag{1.4}$$

where $\chi^{(n)}$ is the n$^{\text{th}}$ order susceptibility of the dielectric medium. Due to inversion symmetry of silica fibers, second order nonlinear term vanishes and the third order susceptibility $\chi^{(3)}$ becomes dominant that creates such main nonlinear effects as the Self Phase Modulation (SPM) and Raman scattering [4]. Thus, P_L and P_{NL} are approximated as:

$$\begin{gathered} P_L = \varepsilon_0 \chi^{(1)} E(r,t) \\ P_{NL} \approx \varepsilon_0 \varepsilon_{NL} E(r,t) \quad where \quad \varepsilon_{NL} = \frac{3}{4}\chi^3 |E(r,t)|^2 \end{gathered} \tag{1.5}$$

In order to solve the wave equation (Eq.1.3) the following assumptions are made [4]:

1. The induced nonlinear polarization (P_{NL}) is so weak (causes <10^{-6} changes in refractive index) and treated as a small perturbation.
2. The polarization is preserved through the propagation.
3. Since the bandwidth of the optical field is much smaller than the central frequency, namely thought as a quasi-monochromatic field $\left(\frac{\Delta\omega}{\omega_0} \ll 1\right)$, the wave equation is obtained assuming slowly varying envelope approximation.

In addition to the simplifying assumptions, the propagation equation is adopted more conveniently in the Fourier domain and transforms to:

$$\nabla^2 E(r,\omega) + \varepsilon(\omega) k_0^2 E(r,\omega) = 0 \tag{1.6}$$

where $k_0 = \frac{\omega_0}{c}$ and $\varepsilon(\omega) = \varepsilon_0\left(1 + \tilde{\chi}^{(1)}(\omega) + \tilde{\chi}^{(3)}(\omega) + \tilde{\chi}^{(5)}(\omega) + \cdots\right)$ and $\tilde{\chi}^{(n)}$ is the Fourier transform of $\chi^{(n)}$. The refractive index (n) and the absorbtion coefficient (α) are derived from the dielectric constant by using $\varepsilon = \left(n + i\frac{\alpha}{2k_0}\right)^2 = (n_L + \Delta n)^2$. The refractive index and the absorbtion coefficient, as a result, consists of both linear and nonlinear terms described by $n = n_L + n_{NL} = n_L + n_2|E|^2$, and $\alpha = \alpha_L + \alpha_{NL} = \alpha_L + \alpha_2|E|^2$ where $n_2 = \frac{3}{8n} Re\{\chi^{(3)}\}$ is the nonlinear index coefficient and the $\alpha_2 = \frac{3\omega_0}{4nc} Im\{\chi^{(3)}\}$ is the two-photon absorbtion coefficient. The dielectric constant is approximated by the refractive index and the absorbtion loss is treated as a small perturbation to refractive index as $\varepsilon = (n_L + \Delta n)^2$ where $\Delta n = n_2|E|^2 + i\frac{\alpha}{2k_0}$. The Helmholtz equation is solved more conveniently in Fourier domain by using the method of separation of variables such that the solution is assumed in the form of:

$$E(r,\omega) = F(x,y) A(z,\omega) \exp(i\beta_0 z) \tag{1.7}$$

where $F(x,y)$ is the mode field distribution, $A(z,\omega)$ is the slowly varying envelope and the β_0 is the wave number. Substituting the Eq. (1.7) into Eq. (1.6), two separate equations can be derived for the mode field distribution and the propagation envelope, respectively.

$$\frac{\partial^2 F(x,y)}{\partial x^2} + \frac{\partial^2 F(x,y)}{\partial y^2} + \left(\varepsilon k_0^2 - \bar{\beta}^2\right) F = 0 \tag{1.8}$$

$$2i\beta_0 \frac{\partial A}{\partial z} + \left(\bar{\beta}^2 - \beta_0^2\right) A = 0 \tag{1.9}$$

The Eq. (1.8) is solved by assuming $\varepsilon = (n_L + \Delta n)^2 \approx n_L^2$ and treating Δn as a first order perturbation to derive the mode field distribution $F(x,y)$ which is not affected by the nonlinear perturbation (Δn). The wave number is also defined as $\bar{\beta}(\omega) = \beta(\omega) + \Delta\beta(\omega)$ where $\beta(\omega)$ is the linear and $\Delta\beta(\omega)$ is the nonlinear terms.

$$\Delta\beta(\omega) = \frac{\omega^2 n(\omega)}{c\overline{\beta(\omega)}} \frac{\iint_{-\infty}^{\infty} \Delta n(\omega)|F(x,y)|^2 dxdy}{\iint_{-\infty}^{\infty} |F(x,y)|^2 dxdy} = -i\frac{\alpha}{2} + \gamma|A|^2 \tag{1.10}$$

where $\gamma = \frac{\omega n_{NL}(\omega)}{cA_{eff}}$ is the nonlinear parameter and $A_{eff} = \frac{\left[\iint_{-\infty}^{\infty}|F(x,y)|^2 dxdy\right]^2}{\iint_{-\infty}^{\infty}|F(x,y)|^4 dxdy}$ is the effective mode area. By using Taylor series expansion around the carrier frequency ω_0 , $\beta(\omega)$ and $\Delta\beta(\omega)$ are expanded as:

$$\beta(\omega) = \beta_0 + \sum_{j=1}^{\infty} \frac{1}{j!}\beta_j(\omega - \omega_0)^j$$

$$\Delta\beta(\omega) \approx \Delta\beta_0 \tag{1.11}$$

$$\bar{\beta}(\omega) \approx \beta_0 + \sum_{j=1}^{\infty} \frac{1}{j!}\beta_j(\omega - \omega_0)^j + \Delta\beta_0$$

where β_j are the higher order linear dispersive terms and $\Delta\beta_0$ is the zeroth order nonlinear term.

By approximating $\left(\bar{\beta}^2 - \beta_0^2\right)$ by $2\beta_0\left[\bar{\beta}(\omega) - \beta_0\right]$ and substituting $\bar{\beta}(\omega)$ with Eq. (1.11), Eq. (1.9) simplifies to

$$\frac{\partial A}{\partial z} + \sum_{j=1}^{\infty} \frac{1}{j!}\beta_j(\omega - \omega_0)^j A = i\Delta\beta_0 A \tag{1.12}$$

Further by substituting $\Delta\beta_0 = \left[-i\frac{\alpha}{2} + \gamma|A|^2\right]$ and taking the inverse Fourier transform of both sides of Eq. (1.11), using the Fourier transform property of $\left[\frac{\partial^j}{\partial t^j} \xrightarrow{\Im} (i\omega)^j\right]$, the well known Nonlinear Schrodinger Equation (NLS) for $A(z,t)$ is derived as:

$$\frac{\partial A}{\partial z}+\sum_{j=1}^{\infty}\frac{1}{j!}\beta_i\frac{\partial^j A}{\partial t^j}=i\Delta\beta(\omega_0)A=-i\frac{\alpha}{2}A+\gamma(\omega_0)|A|^2A \tag{1.13}$$

For ultra short pulses with bandwidth >0.1THz, the validity of the slowly varying envelope assumption vanishes and the higher order terms of the $\Delta\beta(\omega)$ become effective. Including such higher order nonlinear terms as intra-pulse Raman scattering and the self-steepening, the Nonlinear Schrodinger Equation (NLS) becomes:

$$\frac{\partial A}{\partial z}+\sum_{j=1}^{\infty}\frac{1}{j!}\beta_i\frac{\partial^j A}{\partial t^j}-\frac{\alpha}{2}A=i\gamma|A|^2A+\frac{i\gamma}{\omega_0}\frac{\partial}{\partial T}(|A|^2A)-i\gamma T_R A\frac{\partial|A|^2}{\partial T} \tag{1.14}$$

The Nonlinear Schrodinger Equation (NSE) by neglecting the higher order dispersion $(\beta_j=0,\ j>3)$ and the nonlinear terms simplifies to:

$$\frac{\partial A}{\partial z}+\beta_1\frac{\partial A}{\partial t}-i\frac{1}{2}\beta_2\frac{\partial^2 A}{\partial t^2}+\frac{\alpha}{2}A+i\gamma|A|^2A=0 \tag{1.15}$$

The different terms in the simplified NLS equation (Eq. 1.14) describe the effects of group velocity, group velocity dispersion (GVD), fiber loss, and fiber non-linearity. The $\beta_1\left(\frac{s}{m}\right)$ is the reciprocal of group velocity and the $\beta_2\ \left(\frac{ps^2}{m}\right)$ is the GVD parameter of the propagation medium 4].

1.1 Group Velocity Dispersion (GVD)

Group velocity is defined as the effective velocity of wave envelope which has different frequency components. An optical medium in which the waves having different frequencies travel at different velocity is called dispersive medium. Dispersion may originate from the nature of the material (material dispersion) used for light propagation and design of the optical waveguides such as its geometry and materials used in core and cladding part of the waveguide 4,45]. In an optical fiber, phase velocity of the waves can be defined as $v_g=c/n(\omega)$ in terms of frequency. Dispersion is generally thought either normal or anomalous dispersion in which the lower frequencies (red-shifted) travel faster than higher frequencies (blue shifted) or vice verse, respectively. Since each frequency component travels at different speed, the wave starts to broaden. The effect of GVD on the pulse propagation in a linear medium can be studied by eliminating all the nonlinear terms in Schrödinger equation 4, 45]. Then the NLS equation is simplified as:

$$i\frac{\partial A}{\partial z} = -\frac{\beta_2}{2}\frac{\partial^2 A}{\partial t^2} \tag{1.16}$$

This differential equation is easily solved by Fourier transform method. The normalized pulse of arbitrary shape in time domain $A(z,t)$ and its spectrum $\hat{A}(z,t)$ in frequency domain are related by Fourier transform as:

$$A(z,t) = \frac{1}{2\pi}\int_{-\infty}^{\infty} \hat{A}(z,\omega)\exp\left(-i\omega t\right)d\omega \tag{1.17}$$

By taking the Fourier transform of both sides and using the relevant property of $\frac{\partial^n}{\partial t^n} \rightarrow (i\omega)^n$, equation (1.14) transforms into an ordinary differential equation:

$$i\frac{\partial \hat{A}}{\partial z} = -\frac{1}{2}\beta_2\omega^2\hat{A} \tag{1.18}$$

with having a solution of:

$$\hat{A}(z,\omega) = \hat{A}(0,\omega)exp\left(\frac{i}{2}\beta_2\omega^2 z\right) \tag{1.19}$$

By looking at the solution, it is seen that GVD changes the phase of initial pulse spectrum by adding phase to each component proportional to its frequency and propagation length. This phase change in spectrum modifies the pulse shape in time domain 4]. The corresponding time domain solution is evaluated by substituting Eq. (1.18) into Eq. (1.16).

$$A(z,t) = \frac{1}{2\pi}\int_{-\infty}^{\infty} \hat{A}(0,\omega)\exp\left(\frac{i}{2}\beta_2\omega^2 z\right)\exp(-i\omega t)\,d\omega \tag{1.20}$$

In the simulations, Gaussian pulses are used as an initial pump pulse. Thus, the effect of GVD on the Gaussian pulses can be summarized in following equations. A normalized Gaussian pulse having amplitude of unity defines the initial pulse:

$$A(0,t) = \exp\left[\frac{1+iC}{2}\left(\frac{t}{T_0}\right)^2\right] \tag{1.21}$$

where C is the initial chirp parameter and T_0 is the half width at 1/e intensity point and related to full width at half maximum as $T_{FWHM} = 1.665 * T_0$. The final pulse after propagation becomes:

$$A(z,t) = \exp\left[\frac{T_0}{\sqrt{T_0^2 - i\beta_2 z(1+iC)}} exp\left(-\frac{(1+iC)t^2}{2(T_0^2 - i\beta_2 z(1+iC))}\right)\right] \tag{1.22}$$

It is easily seen that both unchirped ($C = 0$) and chirped ($C \neq 0$) Gaussian pulses preserve their shapes after propagation. However, the pulse width T_1 (defined similar toT_0) and the chirp parameter C_1 of the final pulse change due to GVD as [1-2]:

$$\frac{T_1}{T_0} = \left[1 + \left(\frac{C\beta_2 z}{T_0^2}\right)^2 + \left(\frac{\beta_2 z}{T_0^2}\right)^2\right]^{1/2} \tag{1.23}$$

$$C_1(z) = C + (1 + C^2)\frac{\beta_2 z}{T_0^2} \tag{1.24}$$

According to the results, it is obvious that initial pulse starts to broaden due to GVD independent of whether the medium is normal ($\beta_2 > 0$) or anomalous ($\beta_2 < 0$) if there is no initial chirp on the pulse. If there is an initial chirp and($\beta_2 C > 0$), pulse broadens at a rate faster than unchirped pulse. However, if($\beta_2 C < 0$), then the pulse drastically starts to compress to compensate the effect of initial chirp and then starts to broaden again.

1.2 Nonlinear optical effects

When the intensity of electromagnetic field (laser) increases due to small core area of the fiber and high peak power of the ultra short pulses, the optical medium response becomes nonlinear. Two basic nonlinear effects are Self Phase Modulation (SPM) and Cross Phase Modulation (XPM).

1.2.1 Self Phase Modulation (SPM)

Refractive index of the dielectric medium is not only dependent to frequency but also it is dependent to intensity. When the intensity of light inside the medium increases, the index profile becomes nonlinear. As a result, the pulse experiences both GVD and nonlinear effects while propagating in fiber. The dominant effect, however, is directly related with the comparison between the dispersion length $\left(L_D = \frac{T_0^2}{|\beta_2|}\right)$ and the nonlinear length $\left(L_{NL} = \frac{1}{\gamma P_0}\right)$ where γ is the nonlinearity parameter and P_0 is the peak power of the pulse [1]. There are three different scenarios as:

i) If $L>L_D$ and $L>L_{NL}$ both GVD and SPM is effective.

ii) If $L_D>>L>L_{NL}$ then GVD is negligible.

iii) If $L_{NL}>>L>L_D$ then SPM is negligible.

Thus, the individual effect of SPM can be studied by eliminating the GVD, assuming the second scenario, in NLS equation as:

$$\frac{\partial A}{\partial z} = ie^{-\alpha z}\gamma P_0|A|^2 A \tag{1.25}$$

According to this equation, it is seen that the SPM induces an intensity dependent nonlinear phase on the pulse without changing the pulse shape in time domain but the spectrum is drastically distorted. The solution to this ordinary differential equation is simply

$$A(z = L, t) = A(0, t) \cdot exp[i\emptyset_{NL}(z = L, t)] \tag{1.26}$$

where $\phi_{NL}(L,t) = |A(0,t)|^2 \gamma P_0 L_{eff}$ is the nonlinear phase and $L_{eff} = \frac{[1-\exp(-\alpha L)]}{\alpha}$ is the effective length. The maximum phase shift occurs at the center of the pulse, namely at the peak intensity point which is given by $\phi_{max} = \gamma P_0 L_{eff}$ 4].

Due to Fourier theorem, any time dependent phase on the signal generates new frequency components in frequency domain. In other words, temporally changing phase across the pulse makes the instantaneous frequency deviates from its center value w_0 causing a spectral broadening. The amount of SPM induced spectral shift, also called frequency chirp ($\delta\omega$) is obtained by taking the derivative of nonlinear phase.

$$\delta\omega(t) = -\frac{\partial \phi_{NL}}{\partial t} = -\gamma P_0 L_{eff} \frac{\partial}{\partial t} |A(0,t)|^2 \tag{1.27}$$

For Gaussian pulses the SPM induced frequency shift is:

$$\delta\omega(t) = -\frac{2}{T_0^2} \frac{L_{eff}}{L_{NL}} t \exp\left(-\frac{t^2}{T_0^2}\right) \tag{1.28}$$

with a maximum shift of $\delta\omega_{max} = 0.86 \Delta\omega_0 \phi_{max}$ where $\Delta\omega_0 = T_0^{-1}$.

1.2.2 Cross Phase Modulation (XPM)

XPM is another nonlinear phenomenon that causes spectral broadening of the pulses when two or more optical beams having different carrier frequencies are simultaneously launched into a medium. When they interact with each other by inducing an additional nonlinear phase, each optical beam experiences a refractive index which is not only affected by the intensity of that beam but also the intensity of other beams 4]. Their effect on each other through XPM is actually two times more effective than SPM for the same intensity. To summarize, in a medium where N optical pulses with different frequencies propagate simultaneously, the total nonlinear phase seen by each pulse due to SPM and XPM becomes:

$$\varphi_j(t) = \gamma_j \left[L \left| A_j(0,t) \right|^2 + 2 \sum_{j \neq k} \int_0^L |A_k(0, t - zd)|^2 dz \right] \tag{1.29}$$

where $j = 1 - N$. Time dependence of the nonlinear phase due to XPM also implies an additional frequency shift $\delta\omega$ in frequency domain. As seen in the Eq. (1.15), XPM is also dependent to the relative positions of the pulses $(t - zd)$. Since the pulses travel at different velocities in a dispersive medium, they only overlap in a certain time window. The walk-off between the pulses affects the spectral changes and broadening due to XPM [46].

1.3 Numerical solutions to Nonlinear Schrödinger Equation

In general, there is no analytical solution to full wave Maxwell equation for nonlinear optical medium. Numerical solutions on the other hand, because of dimensionality problem are very difficult to apply. However, an approximate solution can be obtained due to some predefined conditions and assumptions. There are basically two kinds of numerical methods as pseudo spectral and finite difference methods. The main difference between them is the elimination of carrier frequency. Because the finite difference methods involve the carrier frequency, they can account for forward and backward propagating waves with more accurately than SSFM [47]. Split Step Fourier Method (SSFM) is one of the pseudo-spectral numerical methods which is easier to implement and computationally faster compared to other numerical methods. SSFM has been an extensively used numerical method aims to solve NLS equation for the propagation of pulses 4].

1.3.1 Split Step Fourier Method (SSFM)

The basic principle behind the SSFM is that it tries to solve the NLS equation as combination of linear and nonlinear terms by treating each part separately. Both linear and nonlinear parts have analytical solutions but NLS equation including both parts does not have an analytical solution. Thus, by dividing the propagation distance into small steps (h), two parts can be solved separately with a small numerical error. Briefly, the linear term due to dispersion and nonlinear term due to nonlinear optical effects are defined respectively as:

$$D = -\frac{\alpha}{2} - \sum_{m=2} \frac{i^{m-1}}{2^{m-1}} \beta_m \frac{\partial^m}{\partial T_m}$$
$$N = i\gamma \left[|A(z,t)|^2 + \frac{2i}{\omega_0 A(z,t)} \frac{\partial}{\partial t} \left[|A(z,t)|^2 |A(z,t)| \right] \right] \tag{1.30}$$

where $A(z,t)$ is the complex field envelope at distance (z) and time (t). Thus the NLS equation can be written in the form as [48]:

$$\frac{\partial A(z,t)}{\partial z} = (D+N)A(z,t) \tag{1.31}$$

with a general solution of

$$A(z+h,t) = \exp\,[h(D+N)]A(z,t) \tag{1.32}$$

The solution to this partial differential equation is approximated by propagating the optical fields over small distance (h) where the dispersive and nonlinear effects are assumed to act independently. In other words, propagation from z to z+h can be held in two steps in which dispersion and nonlinearity acts alone.

$$\exp\,[h(D+N)] = \exp\,[hD]\exp\,[hN] \tag{1.33}$$

The dispersion (D) effect is analyzed in frequency domain rather than taking derivative in time domain to reduce the computational time. Thus, taking the Fourier Transform of both sides and using the Fourier transform property $\frac{\partial^m}{\partial T^m} \to (i\omega)^m$ derivative with respect to time transforms to multiplicative operators and NLS equation reduces to:

$$\frac{\partial A(z,\omega)}{\partial z} = -\frac{\alpha}{2}A(z,\omega) + \sum_{m=2} \frac{i^{m-1}}{2^{m-1}}\beta_m (i\omega)^m A(z,\omega) \tag{1.34}$$

with the solution of

$$\mathrm{A(z+h,\omega)} = A(z,\omega)\; exp\left\{h\left[-\frac{\alpha}{2} - \sum_{m=2} \frac{i^{m-1}}{2^{m-1}}\beta_m (i\omega)^m\right]\right\}$$
$$A(z+h,t) = \mathfrak{I}^{-1}\{A(z+h,\omega)\} \tag{1.35}$$

To reduce the error accumulation more, a new version of SSFM called symmetrized SSFM is used in simulations. The general procedure applied in symmetrized SSFM at every h distance is as follows:

1. Dispersion and loss is calculated over h/2 by setting N=0.

$$A\left(z+\frac{h}{2},T\right) = \mathfrak{I}^{-1}\left\{exp\left[\frac{h}{2}D(i\omega)\right]\mathfrak{I}\{A(z,T)\}\right\}$$

2. At the midpoint of step size, nonlinearity is calculated by setting D=0.

$$A\left(z+\frac{h}{2},T\right)=A\left(z+\frac{h}{2},T\right)\exp\left(hN\right)$$

3. Dispersion and loss is calculated over the second half by setting N=0.

$$A\left(z+\frac{h}{2},T\right)=\mathfrak{I}^{-1}\left\{exp\left[\frac{h}{2}D(i\omega)\right]\mathfrak{I}\{A(z,T)\}\right\}$$

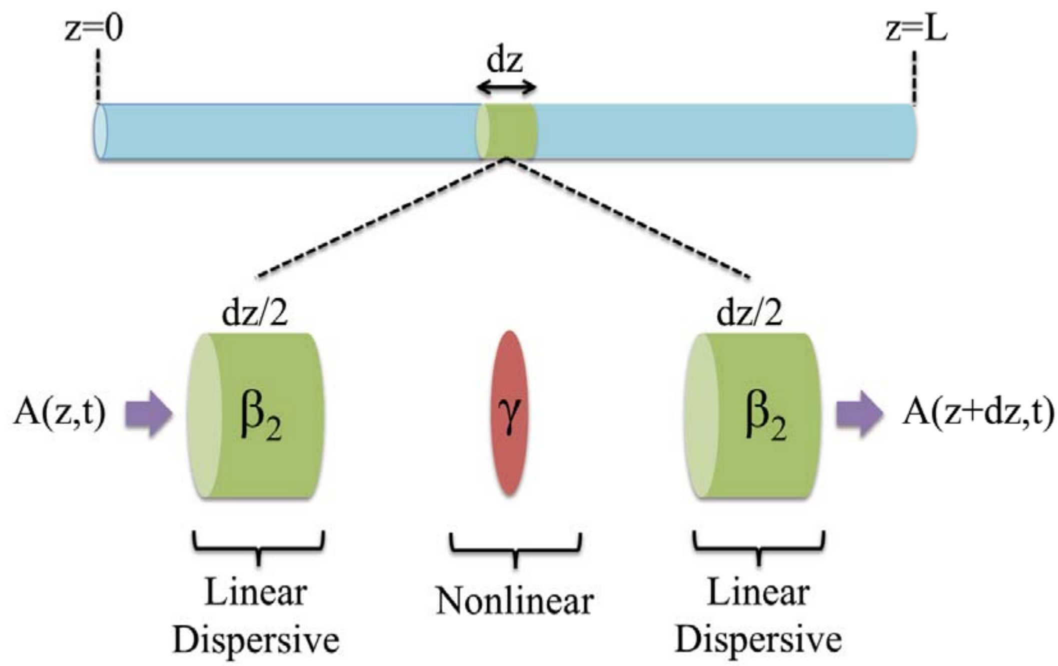

Fig.1.1 Schematics of Split Step Fourier Method. [48]

1.4 Stimulated Raman Scattering (SRS)

Stimulated Raman Scattering is another non-linear and simultaneous process that occurs in any molecular medium [49]. In fibers, Raman scattering has been widely utilized to operate optical fibers as an amplifier or tunable laser by transferring energy from one beam (pump) to others (Stokes) [50-53]. In other words, the weak-low frequency probe beam, also called Stokes wave, is amplified by the intense-higher frequency pump beam trough SRS process. The amount of energy transferred from incident field to scattered field is determined by the vibrational modes of the medium, Fig 1.2.

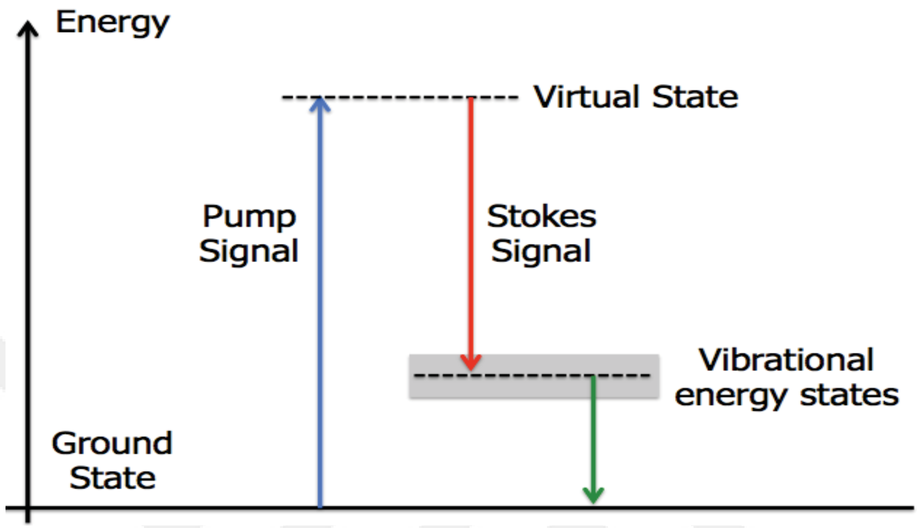

Fig. 1.2 Energy Diagram of Raman Scattering [54].

When both the pump and the probe (Stokes) waves simultaneously propagate inside a fiber, the Stokes wave starts to be amplified due to Raman induced energy transfer, namely due to the Raman gain characterized by Raman gain coefficient (g_R). Raman gain coefficient (g_R) is a function of frequency shift ($\Omega = \omega_p - \omega_s$) between the pump and Stokes waves, and generally depends on the composition of the fiber core, relative polarization of both fields (co-polarized or orthogonally polarized) and the pump wavelength [52]. The Raman gain in silica fibers due to its amorphous nature has a very wide gain spectrum (up to 40THz) with the first peak at nearly 13.2THz and the second peak at 14.7THz due to non-crystalline nature of silica glass, Fig 1.3 [55-56].

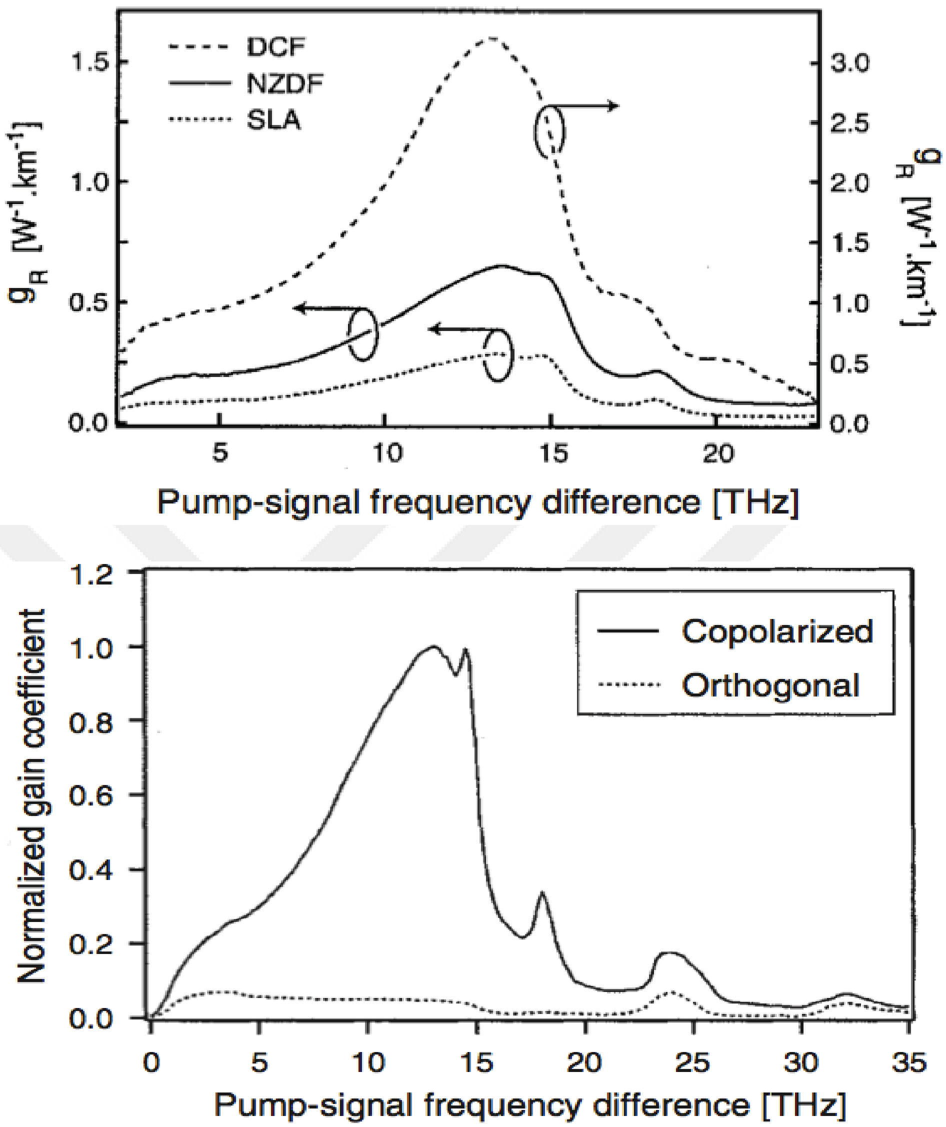

Fig. 1.3 Raman Gain spectrum of silica fiber and the effect of intensity (a), which depends on the type of fibers and the polarization states (b) on Raman gain coefficient [57].

As shown in Fig 1.3, Raman gain spectra show a multi-peak structure due to contribution of many vibrational modes. Although all the fine structures will be absent, Raman gain spectra can simply be modeled by a single peaked function like polynomial, Gaussian or Lorentzian [57].

On the other hand, even without an initial probe beam, new frequency components can be generated and amplified by spontaneous Raman scattering. Although spontaneous Raman scattering generates photons within the entire bandwidth and all are amplified, the frequency component where the Raman gain is maximum is amplified more and dominates in the system. As a result, Stokes wave with the frequency determined by the Raman peak gain (nearly 13.2 THz downshifted for silica) is generated. Raman induced frequency shift enables to generate 26.4-29.4THz (~1000cm^{-1}) frequency separated second order Stokes pulses with ~3THz (~40nm) tunability. This impressive property of SRS enables to design multi wavelength stable soliton Raman lasers to be used in many applications.

For the simplest case in which the CW pump beam is launched inside a fiber, the evolution of pump and the probe beams is governed by the following equations including both the fiber losses and the interaction between them through SRS process [5].

$$\begin{aligned} \frac{\partial I_s}{\partial z} &= g_R I_p I_s - \alpha_s I_s \\ \frac{\partial I_p}{\partial z} &= -\frac{\omega_p}{\omega_s} g_R I_p I_s - \alpha_p I_p \end{aligned} \tag{1.36}$$

where α_p and α_s are the fiber loss coefficients for pump and Stokes frequencies. As seen in the SRS equation, the term $\frac{\omega_p}{\omega_s} > 1$ indicates that the energy emitted from the pump beam is more than the energy gained by the Stokes beam. The remaining energy is lost as phonons in the systems.

There is no analytical solution for these differential equations. However, for the small signal case, i.e. signal is much weaker than the pump, the pump depletion due to the amplification process can be neglected (first term in the second equation) and hence the solution becomes:

$$I_s(z = L) = I_s(0)\exp\left(g_R I_0 L_{eff} - \alpha_s L\right) \tag{1.37}$$

where I_0 is the incident pump intensity and L is the propagation length. In order for the Stokes wave to build up in the fiber, the gain should be greater than the loss as verified in the solution. This solution can only be applied for the initial stages of Raman Soliton generation. Stokes wave circulates in a cavity and is amplified rapidly to reach a steady state by depleting the pump. Thus, for the lasing of the Stokes wave, pump depletion cannot be ignored.

1.5 Optical solitons

Soliton as its name implies, is a particle like wave propagating in a nonlinear medium preserving its shape and surviving after collisions. Propagating undistorted is the most impressive feature of Soliton that enables them to be used in long-haul optical communication systems [46].

Soliton wave is basically the result of interplay between GVD and SPM which independently affect the propagating pulse in a fiber. GVD as discussed in detail is a linear dispersive effect which broadens the optical pulse unless it is initially chirped. In other words, if the pulse is not transform-limited and chirped in a way that the chirp parameter (C) and the GVD parameter β_2 have opposite signs, the pulse compresses during the early stages of propagation and starts to broaden again. On the other hand, SPM as a dominant nonlinear effect introduces a positive chirp ($C > 0$) on the propagating pulse. As a result, when the GVD parameter $\beta_2 < 0$ is negative, namely the pulse propagates in anomalous regime; the broadening effect of GVD can be totally balanced by SPM induced chirp mainly in the central part of the pulse. More specifically, since the SPM induced chirp can be adjusted by tuning the power properly, it cancels the negative chirp induced by GVD [46]. The basic physics under the Soliton wave is explained as in anomalous regime the lower frequency components travel faster than the high frequency components as a result of GVD. SPM, however, affects the pulse in a way that the high frequencies are moved to the leading edge and low ones to the tailing edge, namely induces a positive chirp. As a result of such corporation, total chirp on the pulse is cancelled and enables an undistorted propagation. Briefly, Soliton is a solution of nonlinear Schrödinger equation including both SPM and GVD effects as:

$$\frac{\partial A}{\partial z} + i\frac{\beta_2}{2}\frac{\partial^2 A}{\partial t^2} = i\gamma|A|^2 A \tag{1.38}$$

By introducing $\tau = \frac{t}{T_0}, \xi = \frac{Z}{L_D}$ and $u = N\frac{A}{\sqrt{P_0}}$ where $T_0$is the measure of pulse width, P_0 is the peak power of the pulse and $L_D = \frac{T_0^2}{|\beta_2|}$ is the dispersion length [48]. The equation, considering propagation in an anomalous dispersion regime, (1.25) normalizes to:

$$i\frac{\partial u}{\partial \xi} + \frac{1}{2}\frac{\partial^2 u}{\partial \tau^2} + |u|^2 u = 0 \tag{1.39}$$

which is a special class of nonlinear differential equations that can be solved by inverse scattering method. This equation supports the Soliton wave solution. According to this normalized NLS equation, when the input pulse having an initial envelope of $u(0,\tau) = N\, sech(N\tau)$ is launched into the fiber, it either preserves its shape and remains undistorted or repeats its shape periodically at every $\xi = m\frac{\pi}{2}$ and $z_0 = \frac{\pi}{2}L_D$,distance 4]. As a result, the parameter N determines the propagation pattern of the pulse. If N=1 which means the fundamental soliton case, pulse propagate without changing its shape. However, if N>1 which means high-order soliton case, pulse follows a periodic pattern. The physical meaning behind the parameter N is hided in its definition of $N^2 = \frac{L_D}{L_{NL}}$. N can be thought as the comparison between the dispersion and the nonlinear lengths where only GVD and SPM dominate, respectively.

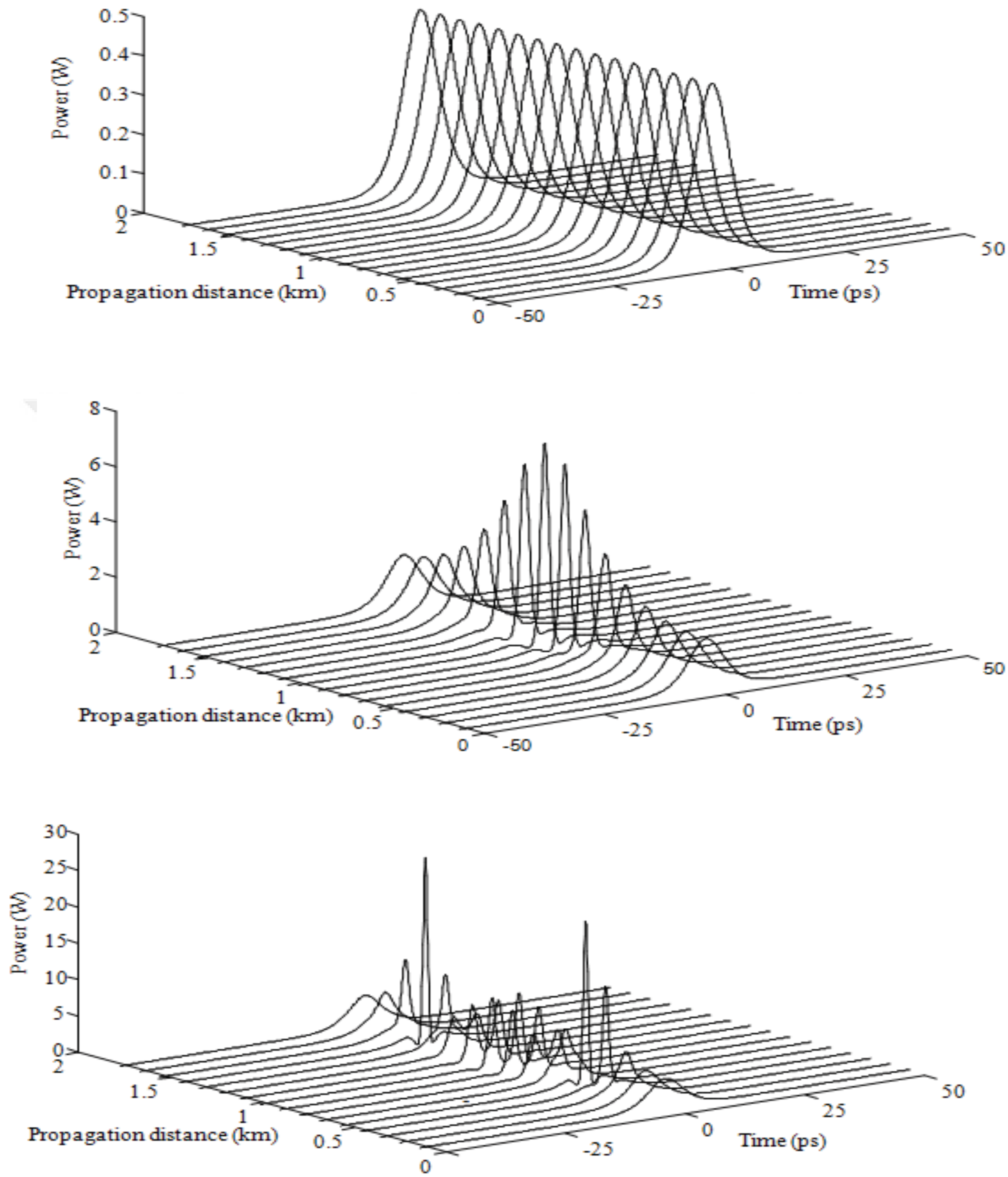

Fig.1.4 Simulation results using our self-developed SSFM for the propagation of fundamental (a), second order (b) and third order (c) Soliton pulses inside the fiber.

CHAPTER 2

Pulsed cascaded lasers up to second order in dispersion managed systems

2.1. Introduction

Wavelength tunable synchronous pulse sources are highly desirable for spectroscopy and optical diagnostics due to their diverse advantages such as broadband operation, low cost, compactness and adaptability with fibers [58-60]. The common method to generate short pulses in the fiber is the use of optical nonlinearities and soliton pulse shaping in the anomalous dispersion regime that results in spectral broadening and pulse compression [61]. However, to generate ultra-short pulses, broadband gain mechanism is also required. Stimulated Raman scattering with a wide gain bandwidth of ~6THz has an ability to generate femtosecond pulses [62-63]. Additionally, Raman gain can be generated at any wavelength in a nonlinear medium, which facilitates generation of pulses at wavelengths which are not attainable by a conventional laser gain medium. Self soliton frequency shift (SSFS) of optical pulses in a highly nonlinear fiber (HNLF) such as photonic crystal fiber due to self Raman scattering effect enables tunable femtosecond pulse generation over a range of >100nm [64]. Fixed-wavelength Raman lasers have been widely studied for the past two decades. Recently, much focus has been shifted toward the multi wavelength tunable Raman fiber lasers which can generate output Stokes pulses in a broad wavelength range by the so called cascaded stimulated Raman scattering [65-68]. For spectroscopy and optical diagnostics, phase coherent and wavelength tunable synchronous pulse sources are of great demand. In particular, in chemistry and biological applications, higher-order cascaded pulsed Raman lasers with up to 1000cm^{-1} frequency spacing is highly desirable for CARS microscopy. Previous experimental works have been dedicated to address that requirement [69-71].

In this chapter, a new configuration for 1st and the 2nd order pulsed Raman lasers with a frequency tuning range up to 1000cm^{-1} is proposed. In particular, a detailed numerical analysis is carried out in order to investigate the stability regime of the generation of Stokes pulses up to the second order in a dispersion managed fiber ring cavity pumped by a 1530nm fiber laser. The stable Stokes pulses can be generated with different pump power levels and lengths of the single mode fiber (SMF) that is included in the dispersion managed (DM) map that forms the cavity. A variational analysis, more powerful and elaborate than the one used in references [72-73] is also employed in order to analytically investigate the steady-state dynamics of Stokes pulses inside the cavity, and to predict the output pulse parameters by solving ordinary differential equations with a periodic boundary conditions which is a computationally efficient alternative to time consuming full numerical simulations. The analytical results are compared with simulation results to show good agreement with the derived equations. The results illustrate that the stable 2nd order Raman Stokes pulses with 0.02mW to 0.1W peak power and 1ps to 2.1ps pulse width can be achieved in our DM Raman laser system.

2.2. Proposed Dispersion Managed (DM) setup and variational equations

In order to generate stable pulsed lasers by the Raman process, inventing a proper dispersion management of the pump, first order and second order pulses is the utmost important issue. Most of the commercial DSFs and SMFs have high dispersion values and slopes; hence it is not possible to maintain a reasonably limited walk-off (which reduces the time overlapping of pulses) through a significant nonlinear interaction length. In order to effectively eliminate such walk-off, we propose the use of the special dispersion-managed map inside the ring laser configuration, which is illustrated in Figs 2.1-2.2. The setup illustrated in Fig 2.1 can be readily experimentally implemented: in this work a detailed numerical stability analysis is performed in order to optimize its parameters. The system is synchronously pumped by a 1530nm mode locked laser with 10ps pulse width. The laser cavity is designed as proposed in [74] that mainly consists of two cascaded sections, the dispersion managed (DM) system as the gain mechanism and the single mode fiber (SMF) for pulse shaping. The overlapping of Stokes pulses at the beginning is satisfied by inserting a stretcher (delay line) in one of the ring cavities to match the pump repetition rate.

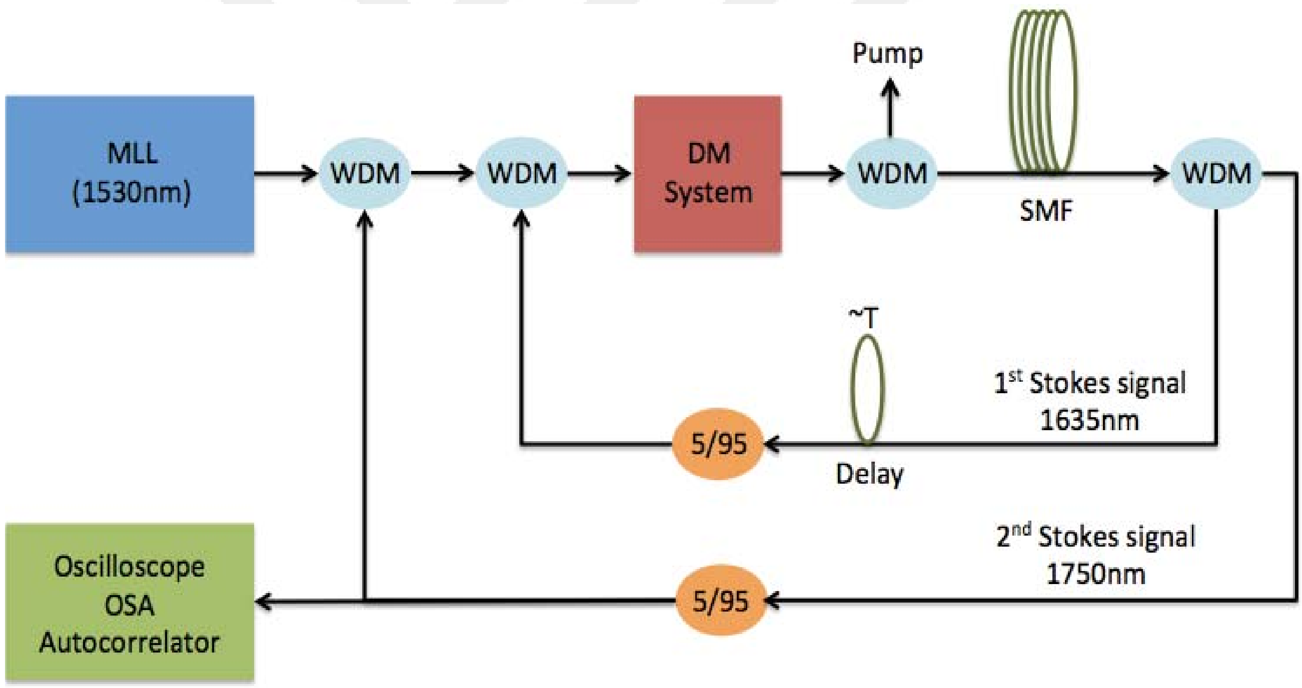

Fig. 2.1 The designed setup with proper dispersion management for the generation of 1^{st} and 2^{nd} order Stokes signals.

Dispersion management is formed by cascading highly nonlinear fiber (HNLF) pieces which has a nearly zero dispersion and dispersion slope in a periodic configuration. In particular, we restrict our analysis to commercially available fibers from different vendors. The characteristics of the HNLF's and the single mode fiber (SMF) used in the simulations are summarized in Table 2.1.

Table 2.1 The characteristics of the fibers used in the simulations [75].

	HNLF (+) slope	**HNLF (-) slope**	**SMF**
α: Fiber loss (dB/km)	0.9	0.9	0.2
γ: Nonlinearity coefficient (1/W-km)	11.5	11.5	2
A_{eff} (μm^2)	11.7	11.7	50
g_R: Raman coefficient (1/W-km)	3.4	3.4	0.8
λ_0: Zero dispersion (nm) / slope(ps/nm^{2}km)	1530 / 0.01	1530 / -0.01	1310 / .076
Length (m)	8	8	20-100

In order to raise the net dispersion to anomalous regime, SMF is cascaded with the dispersion managed system to generate stable soliton like pulses. The Stokes pulse evolution in our ring laser configuration of Fig 2.1 is modeled by supposing that a single (pump and Stokes) pulse re-circulates in the cavity. Therefore, each round trip in the laser involves propagation through a single period of the DM map as in Fig 2.2, which illustrates the dispersion profile for each Stokes order. Stokes pulses are generated through the propagation in the ring laser from the noise level which is taken as the initial condition. When the system reaches a steady state, the Stokes pulses exactly repeat themselves at each period of the map. Thus, the spatial periodic boundary conditions imply that the initial pulse parameters should be the same as the ones at the end of the cavity.

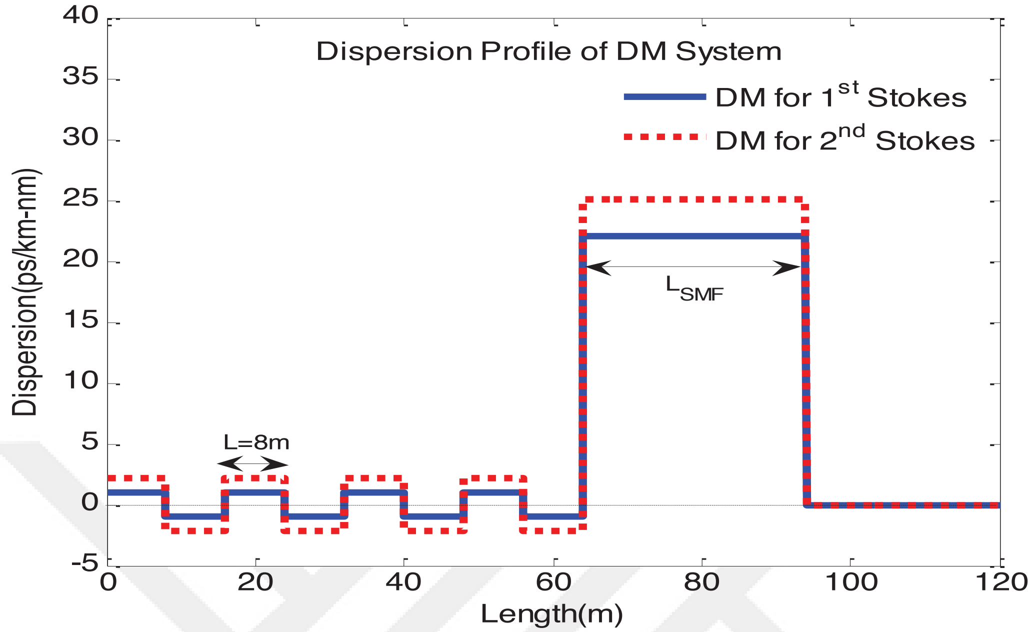

Fig. 2.2 The dispersion managed system for each Stokes pulses.

The mutual interaction between the pump pulse, first and the second order Stokes pulses is governed by a set of three nonlinear Schrodinger equations including all processes of group velocity dispersion (GVD), self phase modulation (SPM), cross phase modulation (XPM), walk off between the pulses, Raman gain and pump depletion 4].

$$\frac{\partial u_p}{\partial z}+\frac{1}{v_{gp}}\frac{\partial u_p}{\partial t}-i\frac{\beta_{2p}}{2}\frac{\partial^2 u_p}{\partial t^2}+i\gamma\left|u_p\right|^2 u_p$$
$$=-\frac{\alpha}{2}u_p-\frac{g_R}{2}\frac{\lambda_1}{\lambda_p}|u_1|^2 u_p-i\gamma(2|u_1|^2+2|u_2|^2)u_p \tag{2.1}$$

$$\frac{\partial u_1}{\partial z}+\frac{1}{v_{g1}}\frac{\partial u_1}{\partial t}-i\frac{\beta_{21}}{2}\frac{\partial^2 u_1}{\partial t^2}+i\gamma|u_1|^2 u_1$$
$$=-\frac{\alpha}{2}u_1+\frac{g_R}{2}\left(\left|u_p\right|^2-\frac{\lambda_2}{\lambda_1}|u_2|^2\right)u_1-i\gamma(2\left|u_p\right|^2+2|u_2|^2)u_1 \tag{2.2}$$

$$\frac{\partial u_2}{\partial z}+\frac{1}{v_{g2}}\frac{\partial u_2}{\partial t}-i\frac{\beta_{22}}{2}\frac{\partial^2 u_2}{\partial t^2}+i\gamma|u_2|^2u_2 = -\frac{\alpha}{2}u_2+\frac{g_R}{2}|u_1|^2u_2-i\gamma(2|u_p|^2+2|u_1|^2)u_2 \tag{2.3}$$

where $\nu_{gp,g1,g2}$ is the group velocity, $\beta_{2p,21,22}$ is the group velocity dispersion parameter (ps^2/km), α is the fiber loss(km^{-1}), g_R is the Raman gain coefficient ($W^{-1}km^{-1}$), γ is the nonlinearity coefficient ($W^{-1}km^{-1}$), and $A_{p,1,2}$ is the amplitude of the pump, first order Stokes and the second order Stokes signals, respectively. These governing equations include all the possible interactions between three optical waves. Four-wave mixing, which cannot build up coherently due to the short length of the HNLFs and the high net dispersion of the cavity, as well as the self Raman induced frequency shift which is negligible for pulses with >1ps pulse width are ignored in this analysis. However, time-consuming numerical analysis is required to determine the pulse evolution in the laser cavity and in optical fibers by using these equations.

Analytical modeling may substantially alleviate computational requirements. Here, an elaborate analytical model is developed for the propagation of pump and the Stokes pulses. The pump pulse which is repetitive at each round trip, is used up in the system and cannot preserve its input Gaussian envelope $\left(|u_p(0,t)|^2=P_{p0}exp\left[-\frac{(t-t_p)^2}{T_p^2}\right]\right)$ where P_{p0} is the peak power, T_p is the pulse width, t_p is the temporal position) [74]. The NLS equation for the pump pulse, Eq.(2.1), can be simplified by neglecting dispersive effects (the GVD parameter at the pump wavelength is zero and the dispersion length is much longer than the cavity length) and by separating spectral (for phase accumulation) and temporal terms (for the pulse shape) so as to solve pump propagation analytically. Fiber loss and pump depletion as seen in Eq. 4 which provides the pump temporal evolution are the dominant terms which affect the pulse shape as follows:

$$\frac{\partial u_p}{\partial z} \approx -\frac{\alpha}{2}u_p - \frac{g_R}{2}\frac{\lambda_1}{\lambda_p}|u_1|^2 u_p \tag{2.4}$$

The pump signal is depleted by the 1st Stokes signal through Raman interaction. Since the walk-off between the pump and the 1st Stokes signal is very small, saturation in the gain line shows up locally by causing hole burning at the center of the pulse, Fig 2.3.

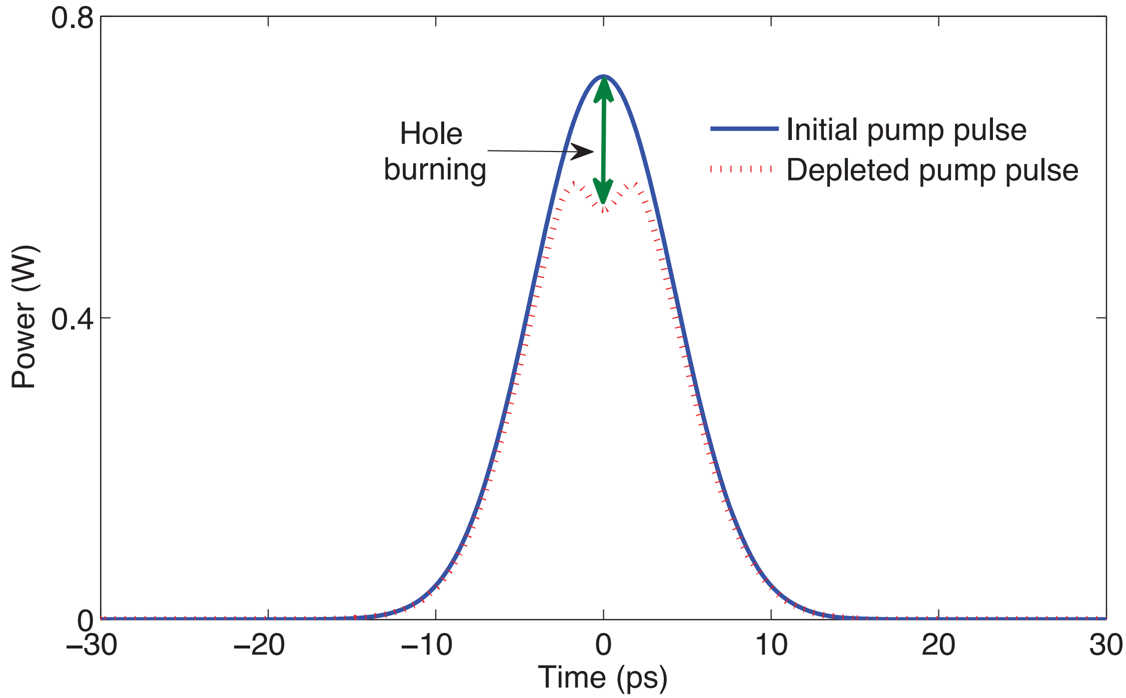

Fig. 2.3 The initial pump pulse at 1530nm with 0.72W peak power and 10ps pulse width is depleted due to 1st Stokes pulse through the DM fiber section creating a hole burning.

The evolution of the pump pulse is approximated by solving Eq.4 as:

$$\left|u_p(z,t)\right|^2 = P_{p0}exp\left[-\frac{(t-t_p)^2}{T_p^2}\right]exp\left[-\int_0^z\left(\alpha + g_R\frac{\lambda_1}{\lambda_p}|u_1|^2\right)d\hat{z}\right] \tag{2.5}$$

$$\begin{aligned}\left|u_p(z,t)\right|^2 &\approx P_{p0}exp\left[-\frac{\left(t-t_p\right)^2}{T_p^2}\right]\left[1-\int_0^z\left(\alpha + g_R\frac{\lambda_1}{\lambda_p}|u_1|^2\right)d\hat{z}\right] \\ &= \left|u_p(0,t)\right|^2 - |u_h(z,t)|^2\end{aligned} \tag{2.6}$$

The second term $u_h(z, t)$ in Eq.(2.6) represents hole burning at the center of the pulse. The hole is modeled by a Gaussian envelope with the peak power (P_h), the pulse width (T_h) and the temporal position (t_h). All loss mechanisms such as fiber loss and gain depletion lead to the growth of the hole (peak power). Since the walk-off between the pump and the 1st Stokes pulses (0.42ps) is much smaller than the pulse width, the pump and the hole are assumed to be temporally co-centered ($t_h \cong t_p$). In addition, due to relatively small change in the pulse width of the pump and the 1st Stokes pulses in the DM section at steady state, the pulse width of the hole is approximated as a combination of pump and 1st Stokes pulse widths [74]. The hole burning is approximated as:

$$\left|u_p(z,t)\right|^2 \approx \alpha P_{p0} + g_R \frac{\lambda_1}{\lambda_p} P_1 P_0 \quad and \quad T_h(z) \approx \left(\frac{1}{T_p^2} + \frac{1}{T_1^2}\right)^{-\frac{1}{2}} \quad and \quad t_h \approx t_p \tag{2.7}$$

The propagation of Stokes pulses is modeled by means of the variational analysis method which assumes the signal maintains its shape even though its power, pulse width and chirp changes in a continuous manner and remains same periodically after each round trip. The evolution of single pulse parameters in the variational method [76] for the unperturbed NLS equations is evaluated by using the Lagrangian density.

$$\mathcal{L} = \frac{i}{2}\left(u\frac{\partial u^*}{\partial z} - u^*\frac{\partial u}{\partial z}\right) + \frac{\beta_2}{2}\left|\frac{\partial u}{\partial t}\right|^2 + \frac{\gamma}{2}|u^4| \tag{2.8}$$

The unperturbed NLS equation is derived from a Lagrangian which is defined as the integration of Lagrangian density with respect to time as:

$$L = \int_{-\infty}^{\infty} \mathcal{L}(u, u_z, u_t; u^*, u_z^*, u_t^*) dt \tag{2.9}$$

where the subscripts z and t correspond to differentiation with respect to distance and time, respectively. The evolution of the pulse parameters is derived by employing modified Euler-Lagrange equations taking into account signal to signal interactions such as Raman amplification, XPM and walk-off as a perturbation to the system. In particular, the physical effects of XPM and temporal walk-off are dominant for determining the chirp evolution, the pump depletion, and the gain reduction [77]. The Euler-Lagrange equation reads as:

$$\frac{\partial L}{\partial z}-\frac{d}{dz}\left(\frac{\partial L}{\partial x_z}\right)=i\mathrm{Im}\left\{\int_{-\infty}^{\infty}\left[R\frac{\partial u^*}{\partial z}-R^*\frac{\partial u}{\partial z}\right]dt\right\} \tag{2.10}$$

where x corresponds to any one of the 6 pulse parameters as the energy, the pulse width, the temporal position, the chirp, the central frequency and the phase, Im denotes the imaginary part and R includes all the perturbation terms analyzed in the right side of the coupled NLS equations. The Gaussian ansatz is assumed for both 1st and 2nd order Stokes pulses as the pulse envelope [76].

$$u=\sqrt{\frac{E}{T}\frac{1}{\sqrt[4]{\pi}}}exp\left[-\left(\frac{(t-t_0)^2}{2T^2}\right)(1+iC)+i\Omega(t-t_0)+i\varphi\right] \tag{2.11}$$

where E is the energy, T is the pulse width, t_0 is the temporal position, C is the chirp parameter, Ω is the center frequency and φ is the phase of the pulse. According the proposed ansatz, the Lagrangian is defined as:

$$L=E\left[-\frac{1}{4}\frac{dC}{dz}+\frac{C}{2T}\frac{dT}{dz}+\frac{\gamma E}{2\sqrt{2\pi}T}+\frac{\beta_2(1+C^2)}{4T_2}+\frac{d\phi}{dz}+t_0\frac{d\Omega}{dz}+\frac{\beta_2\Omega^2}{2}\right] \tag{2.12}$$

By substituting the pulse envelope (Eq.7) and the Lagrangian (Eq.8) with a Gaussian ansatz into the perturbed Euler-Lagrange equation (Eq.6), we derived the modified variational equations for the Stokes pulse parameters, pulse energy (E), pulse width (T), chirp (C), the temporal position (t_0) and the center frequency (Ω) as:

$$\frac{dE_1}{dz} = -\frac{\alpha E_1}{T_1\sqrt{\pi}} I_{0,1,0}(0,t_1,0) + \frac{g_R E_1}{T_1\sqrt{\pi}}\left(J_{0,1,1}(0,t_1,t_p) - \frac{\lambda_2}{\lambda_1}\frac{E_2}{T_2\sqrt{\pi}} I_{0,1,1}(0,t_1,t_2)\right) \qquad (2.13)$$

$$\frac{dT_1}{dz} = \frac{2T_1}{E_1}\left[\begin{array}{c} -\frac{1}{4}\frac{dE_1}{dz} - \frac{E_1\beta_{21}C_1}{2T_1^2} - \frac{\alpha E_1}{2T_1^3\sqrt{\pi}} I_{0,1,1}(0,t_1,0) + \\ \frac{g_R}{2T_1^3}\frac{E_1}{\sqrt{\pi}}\left(J_{1,1,1}(t_1,t_1,t_p) - \frac{\lambda_2}{\lambda_1}\frac{E_2}{T_2\sqrt{\pi}} I_{1,1,1}(t_1,t_1,t_2)\right)\end{array}\right] \qquad (2.14)$$

$$\frac{dC_1}{dz} = -\frac{2T_1}{E_1}\left[\begin{array}{c} \frac{C_1}{2T_1}\frac{dE_1}{dz} + \frac{E_1\beta_{21}(1+C_1^2)}{2T_1^3} + \frac{\gamma E_1^2}{T_1^2 2\sqrt{2\pi}} + \frac{\alpha E_1 C_1}{T_1^4\sqrt{\pi}} I_{1,1,0}(t_1,t_1,0) - \\ \frac{g_R E_1 C_1}{T_1^4\sqrt{\pi}}\frac{1}{T_1\sqrt{\pi}} I_{1,1,1}(t_1,t_1,t_2) + \\ \frac{2\gamma E_1}{T_1^2\sqrt{\pi}}\left(J_{2,1,1}(t_1,t_1,t_p) + \frac{\lambda_2}{\lambda_1}\frac{E_2}{T_1\sqrt{\pi}} I_{2,1,1}(t_1,t_1,t_2)\right) + \\ \frac{4\gamma E_1}{T_1^4\sqrt{\pi}}\left(J_{2,1,1}(t_1,t_1,t_p) + \frac{\lambda_2}{\lambda_1}\frac{E_2}{T_2\sqrt{\pi}} I_{2,1,1}(t_1,t_1,t_2)\right)\end{array}\right] \qquad (2.15)$$

$$\frac{dt_1}{dz} = w_{12} - \frac{1}{E_1}\left[\begin{array}{c} \frac{dE_1}{dz}t_1 - E_1\beta_{21}\Omega_1 + \frac{\alpha E_1}{T_1\sqrt{\pi}} I_{1,1,0}(t_1,t_1,0) + \\ \frac{g_R E_1}{T_1\sqrt{\pi}}\left(J_{1,1,1}(t_1,t_1,t_p) - \frac{\lambda_2}{\lambda_1}\frac{E_2}{T_2\sqrt{\pi}} I_{1,1,1}(t_1,t_1,t_2)\right)\end{array}\right] \qquad (2.16)$$

$$\frac{d\Omega_1}{dz} = \frac{1}{E_1}\left[\begin{array}{c} -\frac{\alpha E_1 C_1}{T_1^3\sqrt{\pi}} I_{1,1,0}(t_1,t_1,0) + \frac{g_R E_1 C_1}{T_1^3\sqrt{\pi}}\left(J_{1,1,1}(t_1,t_1,t_p) - \frac{\lambda_2}{\lambda_1}\frac{E_2}{T_2\sqrt{\pi}} I_{1,1,1}(t_1,t_1,t_2)\right) \\ -\frac{\alpha E_1 \Omega_1}{T_1\sqrt{\pi}} I_{0,1,0}(0,t_1,0) + \frac{g_R E_1 \Omega_1}{T_1^3\sqrt{\pi}}\left(J_{0,1,1}(t_1,t_1,t_p) - \frac{\lambda_2}{\lambda_1}\frac{E_2}{T_2\sqrt{\pi}} I_{0,1,1}(t_1,t_1,t_2)\right) \\ + \frac{4\gamma E_1}{T_1^3\sqrt{\pi}}\left(J_{1,1,1}(t_1,t_1,t_p) - \frac{E_2}{T_2\sqrt{\pi}} I_{1,1,1}(t_1,t_1,t_2)\right)\end{array}\right] \qquad (2.17)$$

$$\frac{dE_2}{dz} = -\frac{\alpha E_2}{T_2\sqrt{\pi}} I_{0,1,0}(0, t_2, 0) + \frac{g_R E_2}{T_2\sqrt{\pi}} \frac{\lambda_2}{\lambda_1} \frac{E_1}{T_1\sqrt{\pi}} I_{0,1,1}(0, t_2, t_1) \tag{2.18}$$

$$\frac{dT_2}{dz} = \frac{2T_2}{E_2} \begin{bmatrix} -\frac{1}{4}\frac{dE_2}{dz} - \frac{E_2\beta_{22}C_2}{2T_2^2} - \frac{\alpha E_2}{2T_2^3\sqrt{\pi}} I_{0,1,0}(0, t_2, 0) \\ + \frac{g_R}{2T_2^3}\frac{E_2}{\sqrt{\pi}}\frac{E_1}{T_1\sqrt{\pi}} I_{1,1,1}(t_2, t_2, t_1) \end{bmatrix} \tag{2.19}$$

$$\frac{dC_2}{dz} = -\frac{2T_2}{E_2} \begin{bmatrix} \frac{C_2}{2T_2}\frac{dE_2}{dz} + \frac{E_2\beta_{22}(1 + C_2^2)}{2T_2^3} + \frac{\gamma E_2^2}{T_2^2 2\sqrt{2\pi}} + \frac{\alpha E_2 C_2}{T_2^4\sqrt{\pi}} I_{1,1,0}(t_2, t_2, 0) - \\ \frac{g_R E_2 C_2}{T_2^4\sqrt{\pi}}\frac{1}{T_1\sqrt{\pi}} I_{1,1,1}(t_2, t_2, t_1) + \\ \frac{2\gamma E_2}{T_2^2\sqrt{\pi}}\left(J_{2,1,1}\left(t_2, t_2, t_p\right) + \frac{E_1}{T_1\sqrt{\pi}} I_{2,1,1}(t_2, t_2, t_1)\right) + \\ - \\ \frac{4\gamma E_2}{T_2^4\sqrt{\pi}}\left(J_{2,1,1}\left(t_2, t_2, t_p\right) + \frac{E_1}{T_1\sqrt{\pi}} I_{2,1,1}(t_2, t_2, t_1)\right) \end{bmatrix} \tag{2.20}$$

$$\frac{dt_2}{dz} = -\frac{1}{E_2} \begin{bmatrix} \frac{dE_2}{dz} t_2 - E_2\beta_{22}\Omega_2 + \frac{\alpha E_2}{T_2\sqrt{\pi}} I_{1,1,0}(t_2, t_2, 0) + \\ \frac{g_R E_2}{T_2\sqrt{\pi}}\frac{\lambda_2}{\lambda_1}\frac{E_1}{T_1\sqrt{\pi}} I_{1,1,1}(t_1, t_2, t_1) \end{bmatrix} \tag{2.21}$$

$$\frac{d\Omega_2}{dz} = \frac{1}{E_2} \begin{bmatrix} -\frac{\alpha E_2 C_2}{T_2^3\sqrt{\pi}} I_{1,1,0}(t_2, t_2, 0) + \frac{g_R E_2 C_2}{T_2^3\sqrt{\pi}}\frac{\lambda_2}{\lambda_1}\frac{E_1}{T_1\sqrt{\pi}} I_{1,1,1}(t_2, t_1, t_2) \\ -\frac{\alpha E_2\Omega_2}{T_2\sqrt{\pi}} I_{0,1,0}(0, t_2, 0) + \frac{g_R E_2\Omega_2}{T_2^3\sqrt{\pi}}\frac{E_1}{T_1\sqrt{\pi}} I_{0,1,1}(t_2, t_1, t_2) \\ + \frac{4\gamma E_2}{T_2^3\sqrt{\pi}}\left(J_{1,1,1}(t_2, t_2, t_p) - \frac{E_1}{T_1\sqrt{\pi}} I_{1,1,1}(t_2, t_1, t_2)\right) \end{bmatrix} \tag{2.22}$$

where we define the integrals as:

$$I_{a,b,c}(t_0,t_1,t_2) = \int_{-\infty}^{\infty} (t-t_0)^a\, f(t-t_1)^b f(t-t_2)^c$$

$$f(t-t_i) = exp\left[\frac{(t-t_i)^2}{T_i^2}\right] \quad where \quad i = p,1,2 \tag{2.23}$$

$$J_{a,b,c}\big(t_0,t_1,t_p\big) = P_{p0} I_{a,b,c}\big(t_0,t_1,t_p\big) - P_h I_{a,b,c}(t_0,t_1,t_h)$$

Here the subscripts i= p, 1, 2 correspond to pump, 1st Stokes and 2nd Stokes signals, respectively [74]. The relative temporal positions of the pulse centers of the pump and the Stokes signals (the second order Stokes signal is assumed to be the time reference) change mainly due to pulse interactions. Since the frequency shift has a negligible effect we can ignore the variation in center frequency. However, the temporal shift due to the walk off effect becomes highly dominant. Thus, we can formulate the change of the pulse temporal positions due to walk off in a reduced form as:

$$\frac{dt_p}{dz} \approx w_{p1} + w_{12}, \quad \frac{dt_1}{dz} \approx w_{12} \quad and \quad \frac{dt_2}{dz} \approx 0 \tag{2.24}$$

where $w_{p1} = \int_{\lambda_p}^{\lambda_1} D(\lambda) d\lambda \approx \frac{D_p+D_1}{2}(\lambda_1 - \lambda_p)$ and $w_{12} = \int_{\lambda_1}^{\lambda_2} D(\lambda) d\lambda \approx \frac{D_1+D_2}{2}(\lambda_2 - \lambda_1)$ stand for the walk-off time between pump-1st Stokes (~0.052ps/m) and 1st-2nd Stokes pulses (~0.19ps/m) per unit length and D is the dispersion value (ps/nm-km) [74].

2.3. Analytical and simulation results

The main objective of our analysis is to determine if the Stokes pulses converge to dispersion managed solitons at the steady state. The Split Step Fourier Method (SSFM) was used to solve the coupled NLS equations (Eq.1-3). Raman amplification is added as a support interaction. The 1st and 2nd order Stokes signals are obtained at the output for different pump power and SMF length (determines the net anomalous dispersion) combinations. Figure 2.4 illustrates the steady state Stokes pulses inside the cavity (i.e. before the couplers) and their peak power evolution in the laser system as an example of transient behavior towards the steady state. The 1st Stokes pulse builds up in the system due to proper pumping. If the 1st Stokes pulse has enough energy (i.e., it reaches threshold for the 2nd Stokes pulse to grow), it starts to generate the 2nd Stokes pulse. While the 2nd Stokes pulse builds up in the system, it depletes the 1st Stokes. Since the system is highly dissipative, the Stokes pulses reach their steady state level in a damped oscillatory manner. The magnitude of the overshoot, oscillations and the settling time in the transient response depend on the pump power level. The temporal deviation of the pulse center of the 1st Stokes signal results from the temporal walk-off effect.

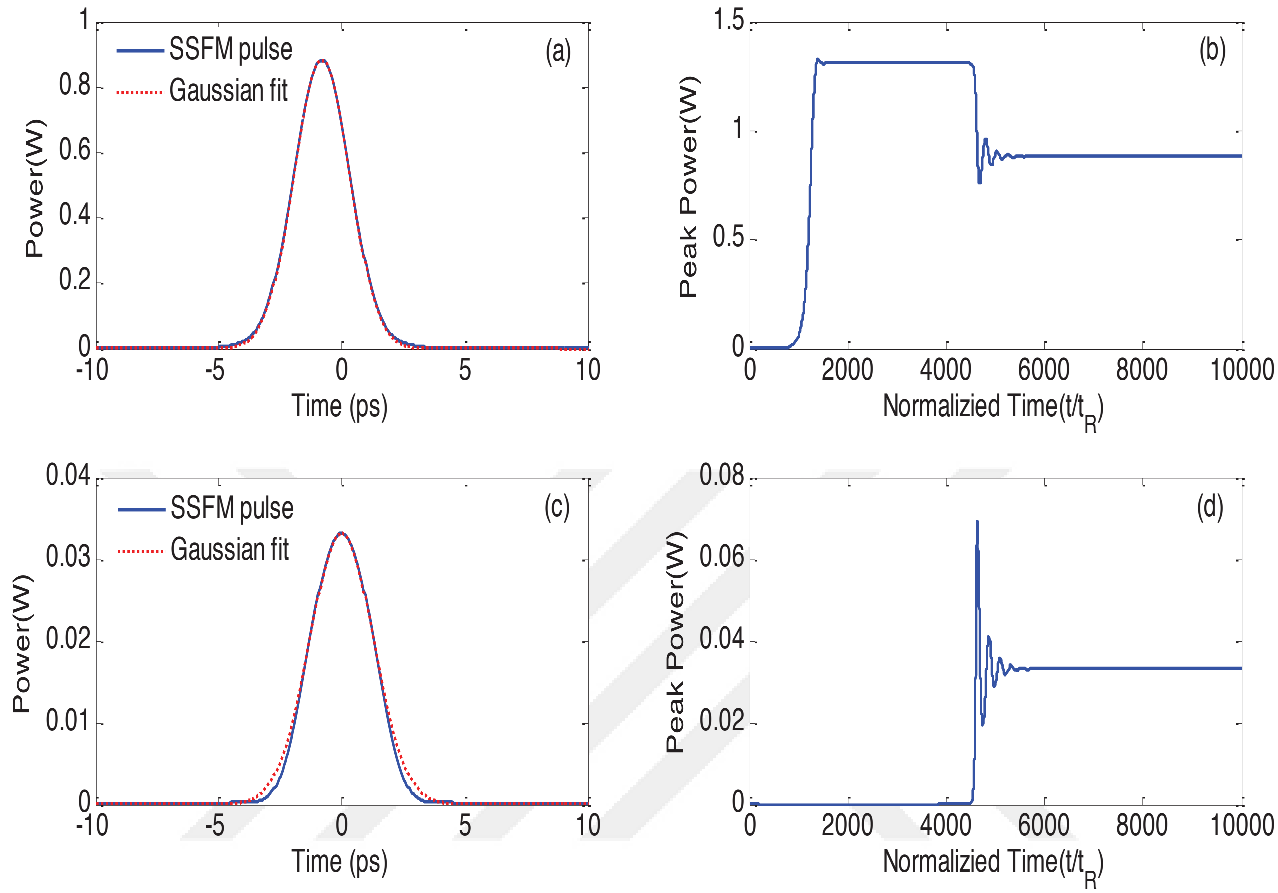

Fig. 2.4 The 1st Stokes pulse (a) with Gaussian fitting and the evolution of its peak power (b), and the 2nd Stokes pulse (c) with Gaussian fitting and the evolution of its peak power (d) at L_{SMF}=50m and P_{pump}=0.72W. The "t_R" is the round trip time of the cavity.

The envelope of the Stokes pulse is also characterized by comparing it with a Gaussian pulse with the same parameters. The 1st Stokes pulse is very well represented by a Gaussian profile; however the tails of the 2nd Stokes pulse are slightly compressed in time so that the Gaussian fitting is less appropriate in this region.

The Stokes pulses repeat themselves after each pass (round trip) at steady state. Thus, the SSFM is employed to propagate the steady-state Stokes pulses for a single pass, so that the intra-cavity pulse dynamics can be analyzed by extracting the evolution of the pulse parameters. Figure 2.5 illustrates the evolution of the peak power and the time width, which is defined as the root mean square (RMS) width, of the Stokes pulses throughout the cavity at the steady state. The dynamics of the parameters of each Stokes pulse has a similar behavior. Throughout the DM section of the cavity where all the Raman interactions occur, distributed gain and other nonlinear effects such as SPM and XPM are the dominant terms. Thus, the Stokes pulses are amplified and positively chirped through the dispersion managed (DM) fibers. Because the dispersion length ($L_D=T_0^2/|\beta_2|$) in the DM-HNLF is much larger than the amplification ($L_A= (g_R|A|^2)^{-1}$) and nonlinear lengths ($L_{NL}= (\gamma|A|^2)^{-1}$), and owing to the net zero dispersion of the entire DM map, linear dispersive effects become negligible as seen by the dynamics of the pulse width. However, in the second section of the cavity (standard SMF), since the pulses become separate due the walk-off, there is virtually no pulse-to-pulse interaction. Here GVD is the dominant effect throughout the SMF. Since the pulses becomes highly positively chirped in the DM section of the cavity due to the acquired nonlinear phase, the Stokes pulses first compress and then broaden as seen by the evolutions in Fig 2.5 of its peak power and time width.

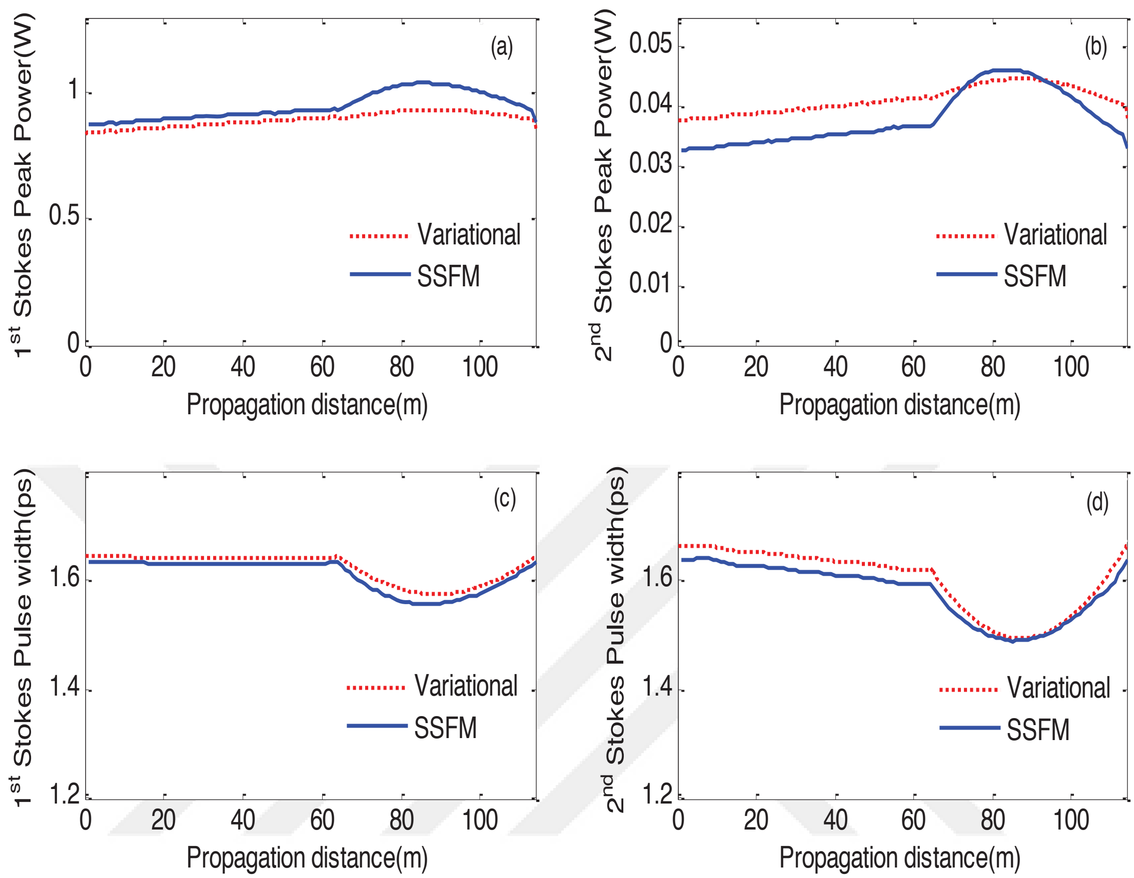

Fig. 2.5 The intra-cavity dynamics of the steady state pulse parameters, peak power and pulse width of 1st order Stokes (a-c) and 2nd order Stokes (b-d) at L_{SMF}=50m and P_{pump}=0.72W are shown. The variational and numerical results are compared.

In order to develop an analytical model to provide a rapid understanding and to explain the pulse dynamics inside the cavity a detailed variational analysis was employed. The intra cavity dynamics of pulse parameters is analyzed in terms of the variational model of Eqs. (13-22) as follows. Firstly, the shooting method is used in order to satisfy the constraint that the same initial and final values for each pulse parameter are obtained upon a single cavity round-trip. Next the intra-cavity variation of these parameters is extracted by solving the same equations for a given steady-state input condition over the entire round trip. To compare the results of the variational analysis with the numerical modeling, I investigated the pulse dynamics for a specific SMF length and pump power (L_{SMF}=50m and P_{pump}=0.72W) as shown again in Figure 2.5. The variational equations are quite successful to explain the general trend of the pulse parameters at the steady-state. Since the variational analysis assumes that the pulse shape does not change throughout the propagation, all perturbations such as Raman gain, pump depletion and the nonlinear chirp (induced by XPM) affect the entire pulse by changing its total energy and phase. However, due to temporal walk-off and the mismatches between the various pulse widths, these perturbations force the pulses to have local changes at different positions. Thus the variational analysis is accompanied by an intrinsic averaging mechanism which reduces the effect of the gain and the chirp (arising mainly from XPM) over the central region of each pulse, which explains the small deviation between variational and numerical results.

In addition to the intra-cavity pulse dynamics, steady-state pulse parameters such as the peak power and the time width (RMS width) of the 1st and the 2nd order Stokes inside the cavity (i.e. before the couplers) that are obtained for different peak pump power levels are extracted by the variational analysis and illustrated in Fig 2.6, along with the corresponding numerical results. The overall agreement with the numerical results obtained by the SSFM confirms the validity of developed variational analysis.

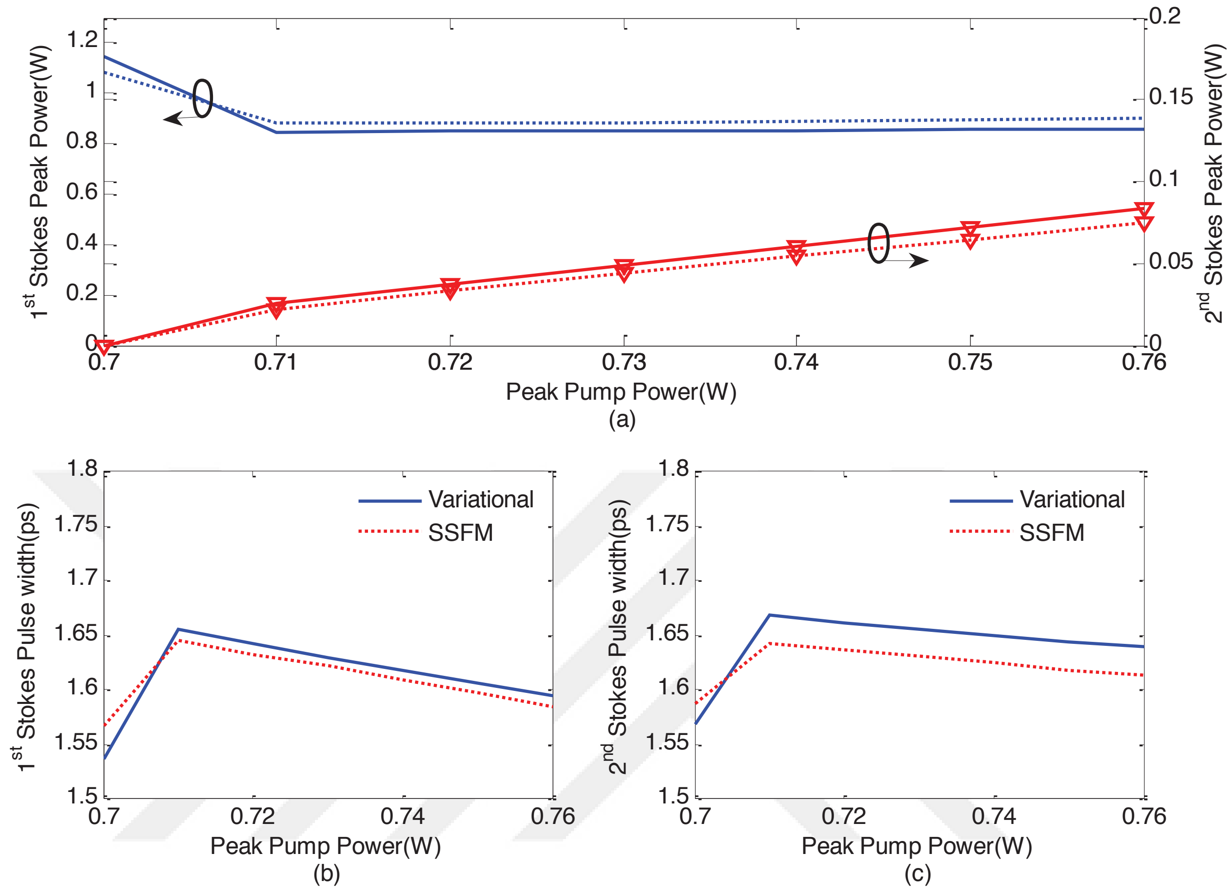

Fig. 2.6 Steady state peak power (a) and pulse width (b-c) of the Stokes pulses with respect to peak pump power at L_{SMF}=50m are shown. The analytical (solid) and the numerical results (dotted) are also illustrated as a comparison.

I also investigate the stable pulse generation regime which is defined by the boundaries of either the Stokes threshold on the one hand and the nonlinear induced pulse break-up on the other hand, for various SMF lengths (net dispersion) ranging from 20m to 100m and for peak pump powers from 0.7W to 0.76W. Clearly the stability of pulse solutions in this regime is due to the attractive nature of the strongly dissipative laser map under consideration. The results are reported in the contour plots of Fig 2.7 which show the peak power and time width (RMS width) of 1st and 2nd order Stokes pulses inside the cavity (i.e. before the couplers) that converge at steady state. Figure

2.7 shows that stable 1st order Stokes pulses with up to 1W peak power and 1ps to 2.1ps pulse widths are generated. Similarly, 2nd order Stokes pulses with 0.02W to 0.1W peak power and 1ps to 2.1ps pulse widths can be obtained.

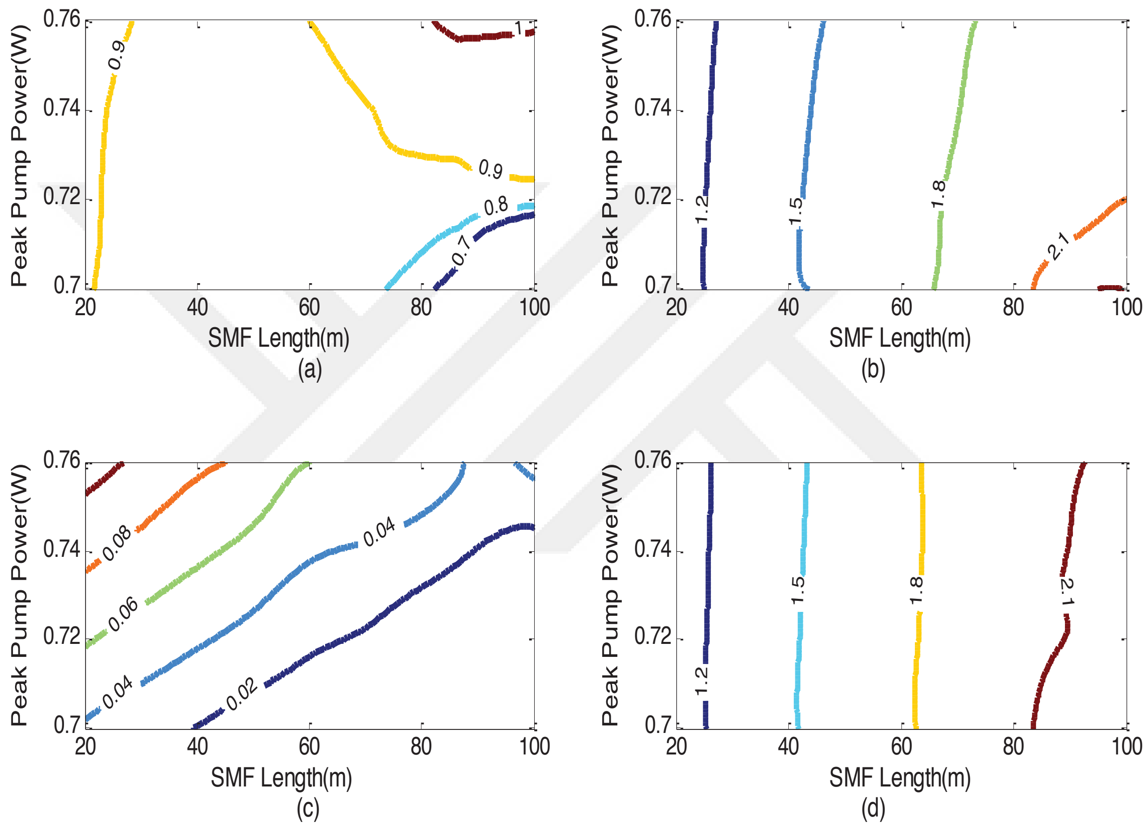

Fig. 2.7 Contour plots for the peak power (W) and pulse width (ps) of the 1st order Stokes pulse (6a-6b) and the contour plots for the peak power (W) and pulse width (ps) of the 2nd order Stokes pulse (6c-6d) with respect to the SMF length and peak pump power.

At low pump powers which are very close to threshold only the 1st order Stokes can be generated. When the pump power is increased, the 1st order Stokes signal starts to build up in the system and converge to a steady state. If the final peak power of the 1st Stokes signal reaches the threshold for 2nd Stokes signal, it generates the 2nd Stokes pulse. At high pump powers, due to imbalance between strong nonlinearity and weak dispersion, the 1st Stokes signal starts to break-up and the laser system becomes unstable. The robustness to nonlinearity increases proportionally to the net dispersion (SMF length), Fig 2.8.

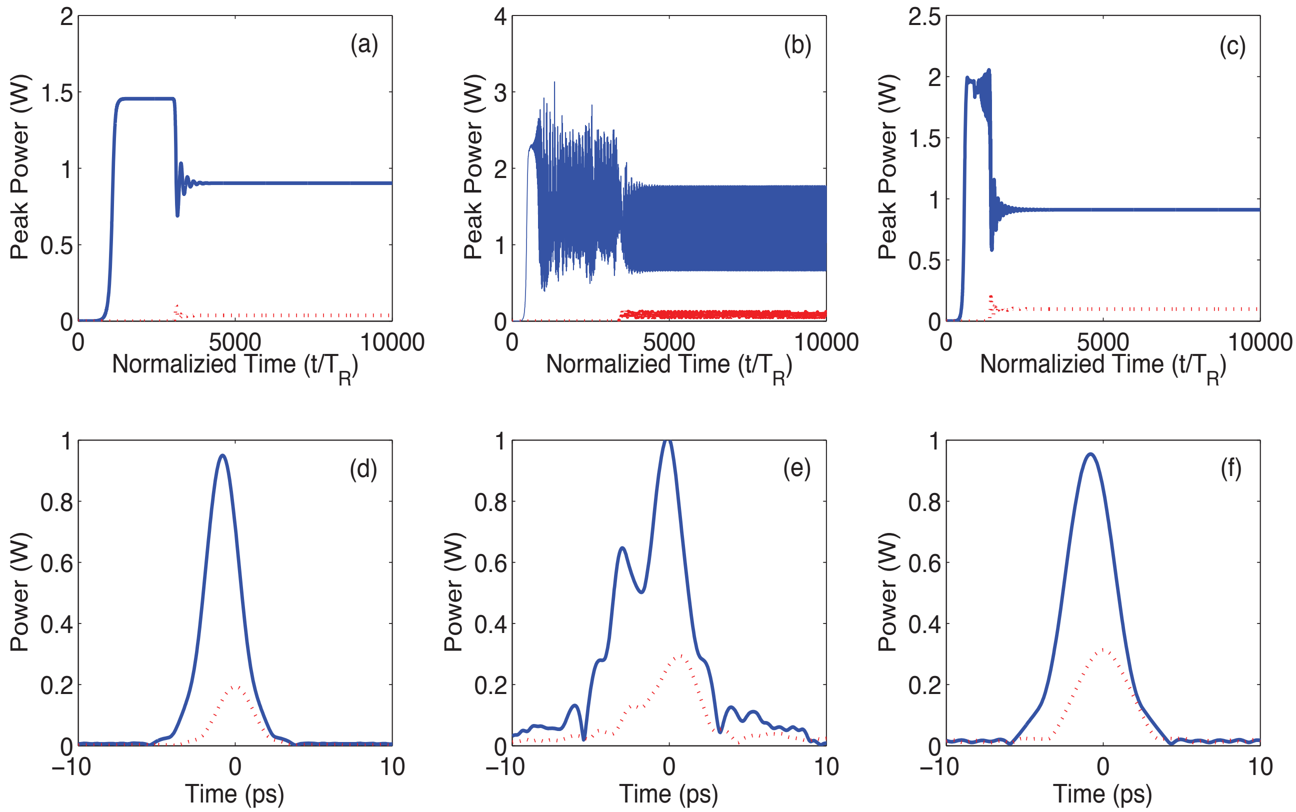

Fig. 2.8 The impact of pump peak power and the amount of dispersion on the stability of the Stokes pulses. Case-1 (a,d): L=20m, P_{peak}=0.70W. Case-2 (b,e): L=20m, P_{peak}=0.78W. Case-3 (c,f): L=50m, P_{peak}=0.78W.

2.4. Conclusion

The novel dispersion managed fiber ring cavity is proposed for phase coherent and wavelength tunable synchronous cascaded pulsed Raman laser with a frequency tuning range up to 1000cm^{-1} which is highly desirable for chemistry and biological applications especially for spectroscopy, optical diagnostics and CARS microscopy. The detailed numerical analysis is carried out in order to investigate the stability regime of the generation of Stokes pulses for different pump power levels and lengths of the single mode fiber (SMF) included in the dispersion managed (DM) map that forms the cavity. A variational analysis is also employed in order to analytically investigate the steady-state dynamics of Stokes pulses inside the cavity, and to predict the output pulse parameters by solving ordinary differential equations with a periodic boundary conditions which is a computationally efficient alternative to time consuming full numerical simulations. The analytical results are compared with simulation results to show good agreement with the derived equations. The results illustrate that the stable 2nd order Raman Stokes pulses with 0.02mW to 0.1W peak power and 1ps to 2.1ps pulse width can be achieved in proposed DM Raman laser system.

CHAPTER 3

Noise performance of time-stretched systems with distributed and discrete amplifiers

3.1. Introduction

The revolution of optical signal processing has enabled many applications ranging from broadband communications to radar systems and imaging applications by introducing high-speed operations. Recent advances in optical signal processing have enabled the design of ultrafast instruments that operate in real time with high temporal resolution and high throughput efficiency [78]. Real-time instruments are highly desired for capturing of ultrafast rare events, wideband analog to digital converter (ADC) [79-80], spectroscopy [81] and imaging [82-84] applications. The amplified photonic time-stretch technique based on group-velocity dispersion (GVD) is capable of slowing down and amplifying of intensity modulated signal so that it can be captured in real-time with an electronic digitizer.

Photonic time stretched systems are mainly designed by combining the broadband illumination, spectral domain processing and time to wavelength mapping modules, Fig 3.1. To provide a broadband spectral window to capture the information of interest, supercontinuum pulses are generated by propagating the Mode Locked Laser (MLL) pulses through the amplifier (EDFA) and the supercontinuum (SC) fibers [85]. In the first step, the broadband spectrum of the pulses is either mapped over the time (by using dispersive elements for ADC applications) or over the space (by diffractive elements for imaging applications). Then, the wavelengths are shaped by the information of interest, which can be a fast non-repetitive RF waveform especially in a communication network, the spectroscopic signature of a materials or the image of an object. Finally, to obtain real time operation, the spectral modulation is converted into temporal modulation via time to wavelength mapping (i.e. time stretching). In other words, spectrally modulated SC pulses are passed through the highly dispersive fibers to perform so-called optical Fourier transformation, which converts the frequency (spectral) domain into temporal domain.

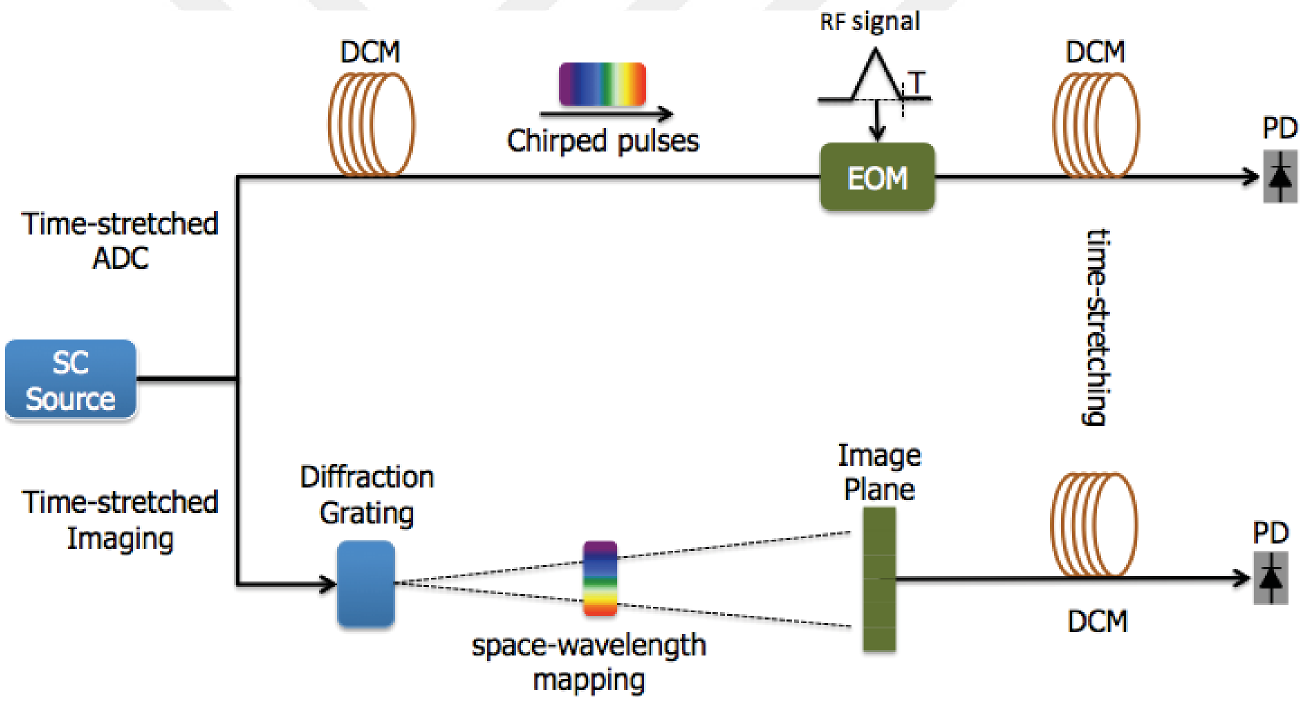

Fig. 3.1 The schematic of the photonic time-stretched analog-to-digital converter and imaging systems [79-81].

In order to effectively enable time-wavelength mapping, the temporal resolution of the system, which is the temporal width ($\Delta\tau$) of the SC pulses, has to be short enough to catch the high frequency features. In other words, the optical bandwidth has to be much higher than the electrical bandwidth to effectively sample the RF signal without any loss due to well-known Nyquist theorem as $\Delta\tau \ll \Delta T = \frac{1}{2\Delta f_{RF}} \xrightarrow{yields} 2\pi\Delta f_{opt} \gg \Delta f_{RF}$ [79]. Since the optical bandwidth is typically in the THz range whereas the RF bandwidth is in GHz range, the condition for time-to-wavelength mapping is normally satisfied. As discussed in chapter 1, nonlinear dispersion as characterized by the higher order dispersion terms ($\beta_3, \beta_4, \ldots$) causes different spectral segments to stretch in different amounts in a nonlinear manner so that the time stretching becomes time dependent. The group delay ($\Delta\tau$) for a certain bandwidth ($\Delta\lambda$) per unit length of the fiber is calculated as $\Delta\tau = \int_{\Delta\lambda} D\,(\hat{\lambda})\, d\hat{\lambda}$. At the output, the temporal width of the SC pulses becomes $\Delta t_{out} = L\,\Delta\tau$.

In this chapter, discrete and the distributed amplifiers, which are utilized to compensate the system losses, have been analyzed comparably to investigate their effects on the noise performance of time stretch systems. Firstly, an analytical study have been conducted to characterize the individual noise components and hence the ENOB performance of the system. It has been showed that the cumulative noise mainly due to amplifier, double Rayleigh scattering (DRS) and relative intensity noise (RIN) limit the maximum effective number of bits (ENOB) that can be achieved in such a system. Secondly, a time stretched system with >10GHz analog bandwidth is designed especially for ADC applications. It has been showed that the system exhibit 16dB higher SNR corresponding to ~2.5-bit higher resolution using distributed amplification. Finally, ~60nm broadband Raman amplifier with nearly flat gain profile (<0.5dB gain ripple), which will be used in ADC, RF arbitrary waveform generation (AWG) and dispersive imaging experiments, is experimentally demonstrated and the noise performance is characterized.

3.2. Discrete and distributed amplification

In order to compensate the system loss and to achieve extremely large stretching factors, which scale the amplitude as being stretched in time to preserve the pulse energy, optical amplification should be employed in the system, especially over the second highly dispersive (longer and higher insertion loss) stage. Optical amplification can be utilized either by embedding discrete (lumped) amplifiers at discrete positions or by distributing the gain over the system. For the distributed amplification, a flat gain broadband Raman amplifier is designed.

3.2.1. Discrete amplification

Discrete amplification as the name implies, is performed by utilizing optical amplifiers placed at discrete positions. These amplifiers are typically bulky optical devices which requires special doped fibers to provide desired gain profile. Erbium Doped Fiber Amplifier (EDFA) is most commonly used one where the core of a silica fiber is doped with Erbium ions and can be efficiently pumped with a laser at a wavelength of 980 nm or 1450 nm, and exhibits gain in the 1550 nm (communication wavelength) region [86].

As illustrated in Fig 3.2, the EDFA has a narrowband gain curve and the wavelengths are determined by the resonant levels of the Er atom. In addition, since the energy is stored in the upper level of the Er the gain process is slow.

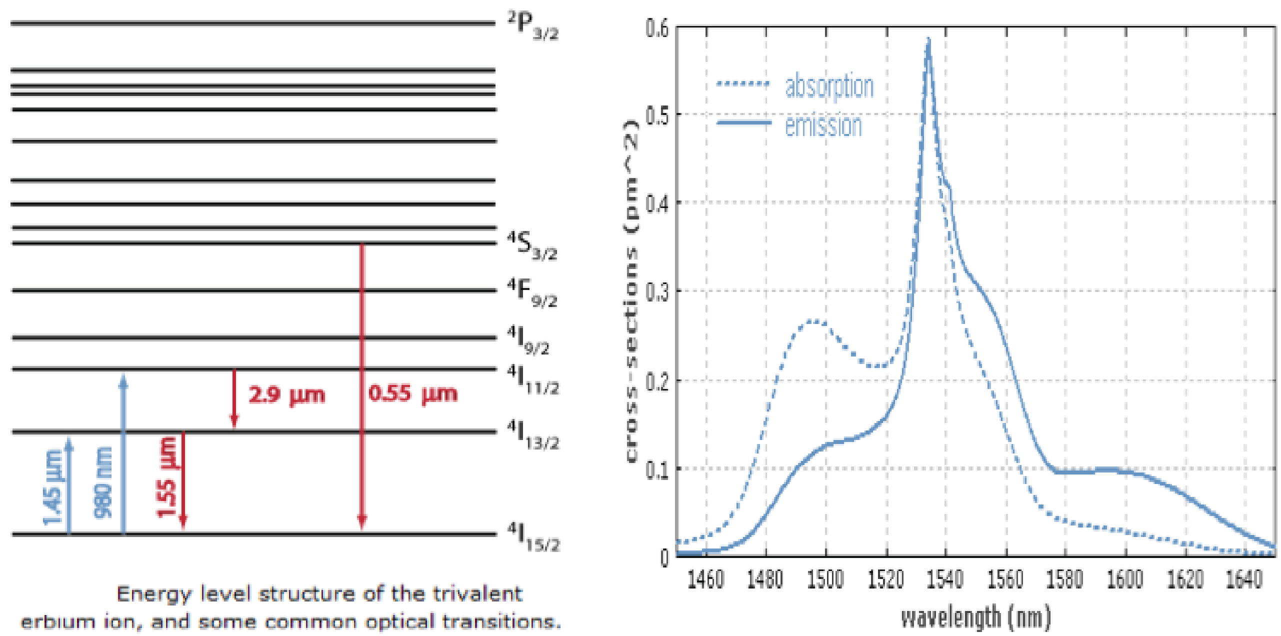

Fig. 3.2 Energy level structure of Erbium ion [9] and some optical transitions (a). Absorption and emission cross-sections for Erbium ions [87] in Er: Yb-doped phosphate glass (b) [86].

3.2.2 Distributed amplification

For the distributed amplification, a flat gain Raman amplifier, which is based on stimulated Raman scattering, is utilized to provide a uniform amplification for the broadband signal. Rather than a discrete amplification at certain positions, signals are amplified through the fiber link in a distributed manner. The fiber becomes the gain medium for the Raman amplification when properly pumped [88]. The pumping can be in the same direction as the signal (co-pumping), in the opposite direction of the signal (counter-pumping) or in a mixed configuration (hybrid pumping), Fig 3.3.

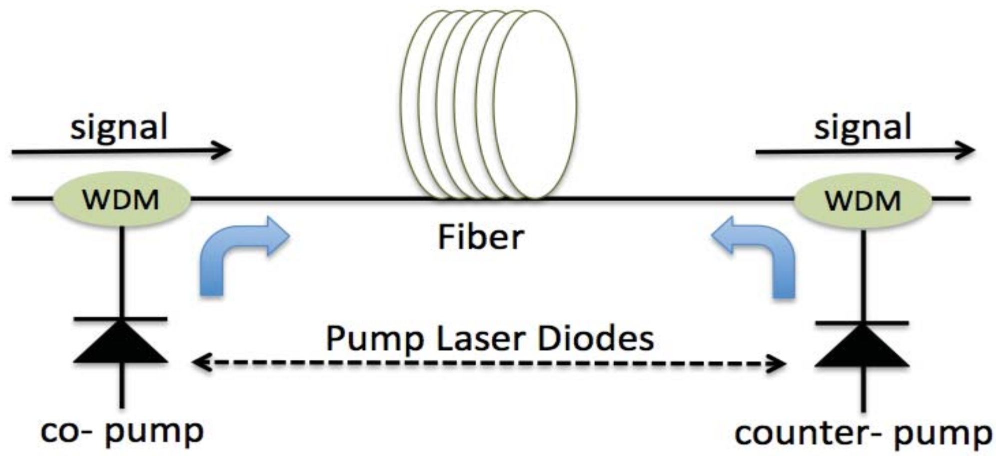

Fig. 3.3 The schematics of the Raman amplifier including co/counter pump laser diodes.

The distributed Raman amplification provides a better alternative to discrete amplification in terms of the feasibility, achievable gain bandwidth, uniformity and the SNR. The main advantages of Raman amplifier over lumped EDFA are:

1. Since the Raman amplification is based on stimulated Raman scattering (SRS), which is a simultaneous process, it enables fast gain mechanism [88].
2. Raman amplification via distributing the gain over the entire fiber ensures the signal levels to stay inside the safe region, namely prevents the signals to be affected by nonlinear effects (high power) and interfered with high noise (low power) [80].

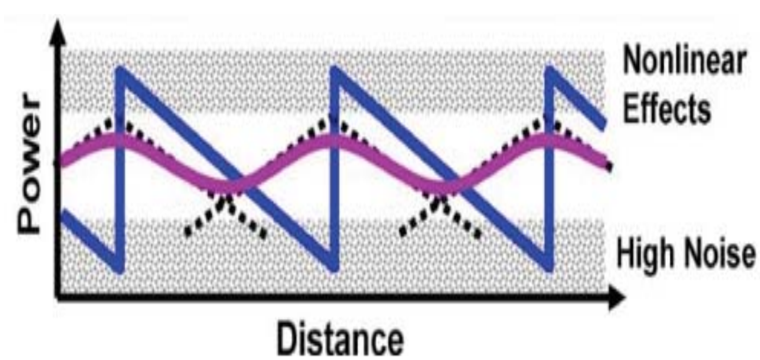

Fig. 3.4 The signal level dynamics inside the fiber with discrete (blue) and distributed amplification (red) [80].

3. Raman amplification provides broadband gain profile, which is independent of pump wavelength and only a function of frequency shift. Using multi pumping scheme with co-pumping, counter-pumping or hybrid pumping configurations and by selecting appropriate pump wavelengths and the powers, broadband and uniform spectral gain profile can be obtained.

The multi-pumped Raman amplifier is modeled by including all the signal to signal (pump-pump, pump-signal and signal-signal) interactions and the wavelength dependent attenuation (α_k). The evolution of all the signal and pump powers along the longitudinal axis of the fiber (z) in a Raman amplified system is governed by solving the following set of equations as:

$$\pm\frac{dP_k}{dz} = -\alpha_k P_k + \sum_{j=1}^{k-1} g_{\lambda_j}\left(\lambda_k - \lambda_j\right) P_j P_k - \sum_{j=k+1}^{N} \frac{\lambda_j}{\lambda_k} g_{\lambda_k}\left(\lambda_j - \lambda_k\right) P_j P_k, \quad k = 1,2,\ldots,N \tag{3.1}$$

where $+/-$ corresponds to $\text{co}/\mathit{counter\ propagating}$ signals, P_k is the pump/signal power, α_k is the wavelength dependent attenuation coefficient and g_{λ_j} is the Raman gain coefficient for the signal at wavelength λ_j which is proportional to reference gain coefficient at λ_0 as $g_{\lambda_j}(\Delta\lambda) = \frac{\lambda_j}{\lambda_0} g_{\lambda_0}(\Delta\lambda)$ [89]. The first term on the right side of the equation represents the wavelength dependent fiber attenuation. The second term is the gain introduced on the signal at wavelength λ_k by the other signals with higher frequencies, λ_j, $\mathrm{j} = 1, \ldots, \mathrm{k} - 1$. The last term, on the other hand, represents the pump depletion on the signal at wavelength λ_k due to power transfer to the other signals with lower frequencies, λ_j, $\mathrm{j} = \mathrm{k} + 1, \ldots, \mathrm{N}$. In order to achieve uniform wideband gain profile, a multi pumped Raman amplifier has to be designed and optimized by properly selecting the pump wavelengths and the powers. The genetic and the shooting algorithms are developed and used together to design a Raman amplifier for the desired gain profile, Fig 3.5.

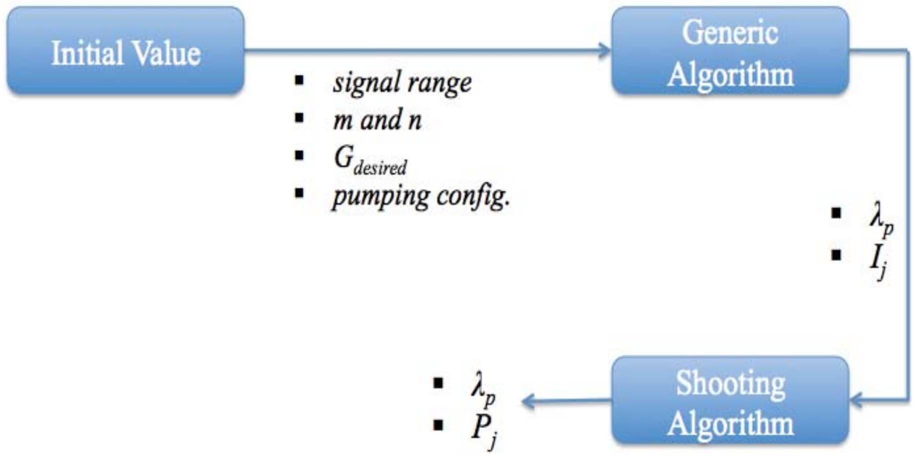

Fig. 3.5 The algorithm of the Raman amplifier model. The *m* and *n* are the number of pump and signal channels and (λ_p , I_j , P_j) is the output pump spectra (wavelength, pump integral, pump power).

The 2D genetic algorithm [89] is employed initially to find the optimum wavelength and the power integral ($I_j = \int_0^L P_j(z)\, dz$ *where j=1-m*) combinations for *m* number of pump lasers, which ensure the maximum gain ripple (defined by F: fitness parameter) is less than a pre-defined tolerance (<10%).

$$G_k = \frac{P_k(L)}{P_k(0)} \approx exp\left(-\alpha_k L + \sum_{j=1}^{m} g_{\lambda_j}(\lambda_j - \lambda_k) I_k\right) \tag{3.2}$$

$$F = 10log_{10}\left[\frac{\left(10log_{10}(G_k^{max}) - 10log_{10}\left(G_k^{min}\right)\right)}{10log_{10}(G_{desired})}\right] \times 100\% \tag{3.3}$$

After optimizing the pump spectra (the wavelengths and the pump integrals), the shooting algorithm [90] is employed to obtain the corresponding pump powers due to the pumping configuration. The developed Raman amplifier model is tested to achieve nearly flat gain profile with maximum gain ripple to be less than 5% over 20nm bandwidth (1580nm-1600nm):

i. By using four laser diodes with fixed wavelengths (the available laser diodes to be used in the experiment) at 1450nm, 1470nm, 1490nm and 1505nm.

ii. Four different pumping configuration as illustrated in Table 3.1.

Table 3.1 Four different pumping configuration by using four fixed wavelength laser diodes.

	LD-1 (1450nm)	**LD-2 (1470nm)**	**LD-3 (1490nm)**	**LD-4 (1505nm)**
SET-1	Backward	Backward	Forward	Forward
SET-2	Forward	Forward	Forward	Forward
SET-3	Backward	Backward	Backward	Backward
SET-4	Forward	Forward	Backward	Backward

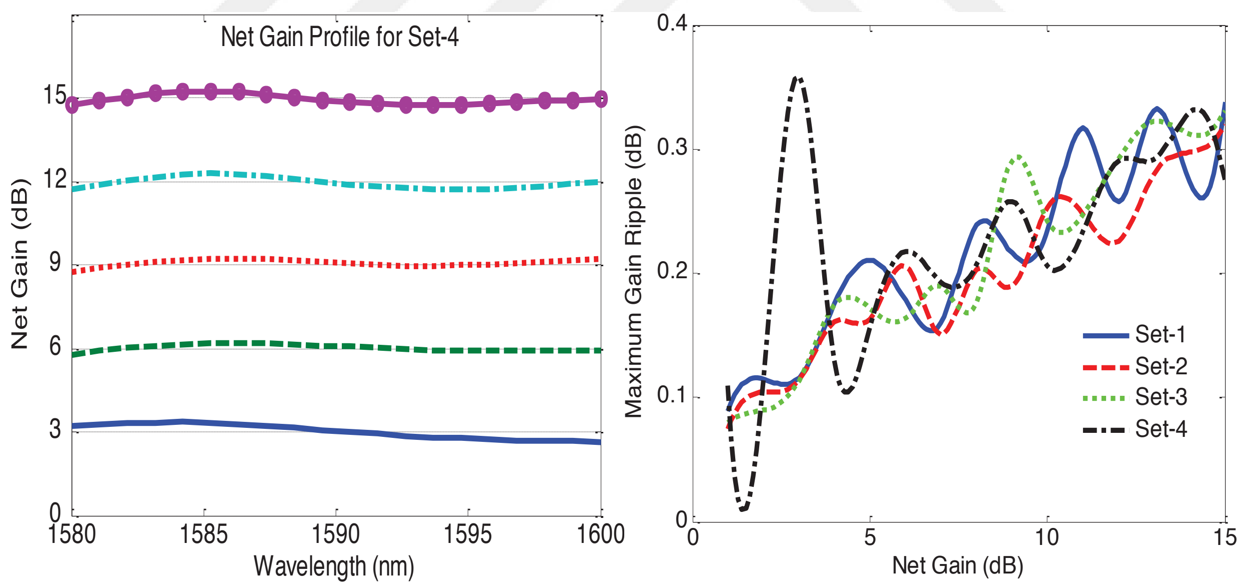

Fig. 3.6 The optimized net gain profile for Set-4 configuration over 1580nm to 1600nm (a). The maximum gain ripple with respect to net gain and different pumping configuration (b).

3.2.3. Individual noise components

The performance of the dispersive systems in terms of noise figure (NF) and the signal to noise ratio (SINAD) is limited by the noise cumulated in the system from both optical and electrical sources. Under SINAD analysis, all the noise components such as amplified spontaneous emission (ASE), relative intensity noise (RIN), double Rayleigh backscattering (DRS), quantization noise and the detector noises as thermal and shot noises are investigated individually.

a. Quantization noise

The quantization noise due to electronic analog to digital converter is modeled as white noise with a uniform spectral density of $S_Q(f)$ up to half sampling frequency (f_s/2). The noise variance $\sigma_Q^2 = \int_{\Delta f} S_Q(f)df$ is obtained as:

$$\sigma_Q^2 = \frac{2(2mP_{in}RG)^2}{12f_s 2^{2N}}\Delta f \tag{3.4}$$

where m is modulation index, f_s is the sampling frequency, G is the gain, P_{in} is the input power, R is the responsivity of the detector, N is the number of bits and Δf is the effective noise bandwidth [91].

b. Shot noise

Electrons generated at random times results in a fluctuation in the photo detector current, which is called shot noise. Shot noise is a stationary random process modeled as a white noise with a constant spectral density of $S_s(f)$. The noise variance $\sigma_s^2 = \int_{\Delta f} S_s(f)df$ is obtained as:

$$\sigma_s^2 = \int_{\Delta f} S_s(f)df = 2q(P_{in}GR)^2\Delta f \tag{3.5}$$

where q is the electrical charge [45].

c. Thermal noise

Electrons in any conductor move randomly due to the temperature. This temperature induced random motion of electrons causes fluctuations in the current called thermal noise. Thermal noise is modeled as a stationary Gaussian random process with a spectral density of $S_{th}(f), which$ is frequency independent up to 1THz. The noise variance $\sigma_{th}^2 = \int_{\Delta f} S_{th}(f)df$ is obtained as:

$$\sigma_{th}^2 = \int_{\Delta f} S_{th}(f)df = \frac{4k_B T}{R_L} F_n \Delta f \tag{3.6}$$

where k_B is the Boltzman constant, T is the temperature, R_L is the load resistance and $F_n$is the noise figure [45].

d. Amplified Spontaneous Emission (ASE)

In both discrete and distributed amplification processes, the excited electrons emit photons either via stimulated or spontaneous manner. Spontaneous emission generates randomly phased photons which appears as a noise added on to the amplified signal. The ASE noise in discrete amplifier is modeled as a white noise with spectral density of $S_{ASE}(f)$. The noise variance $\sigma_{ASE}^2 = \int_{\Delta f} S_{ASE}(f)df$ is obtained as:

$$\sigma_{ASE}^2 = 4R^2 P_L (G-1) n_{sp} h\nu_0 \Delta f \tag{3.7}$$

where G is the gain, $P_L = GP_{in}$, n_{sp} is the spontaneous emission coefficient and $h\nu_0$ is the average photon energy [88]. Contrary to EDFA, in Raman amplification spontaneous Raman scattering is amplified by the distributed Raman gain. The current fluctuations result from the signal-ASE and ASE-ASE (so small and can be neglected) beating. The noise variance σ_{ASE}^2 becomes:

$$\sigma_{ASE}^2 = 4R^2 P_L n_{sp} \Delta f h\nu_0 G_L \int_0^L \frac{g_R P_p(z)}{G(z)} dz \tag{3.8}$$

where $G_L = G(z = L)$ and P_p is the pump power [88]. For a Raman amplifier with multi-pump configuration, the effects of all the pumps on the ASE noise are included as $\int_0^L \frac{\sum_{j=1}^{n} g_{Rj} P_{pj}(z)}{G(z)} dz$ where n is the number of pumps.

e. Relative Intensity Noise (RIN)

All lasers especially the semiconductor laser diodes used as a pump for Raman amplifiers exhibit instability in the power levels due to such mechanical and optical effects as the cavity vibration, spontaneous emission and fluctuations in the gain medium. In discrete amplification, since there is no pumping mechanism the RIN noise results only from the signal laser diodes, which has much lower intensity noise (<160dB/Hz). On the other hand, since the Raman amplification employ many high power laser diodes which have comparably higher intensity noise (>-140dB/Hz) and the Raman gain is exponentially dependent to pump power, any fluctuations in the pump power is intensified and transferred to the amplified signal causing larger fluctuations [92]. The pump induced RIN transfer $\left(\frac{RIN_s(f)}{RIN_p(f)}\right)$ is calculated by analytically solving the coupled equations.

$$\frac{\partial P_i}{\partial z} + \left(\frac{1}{v_i} - \frac{1}{v_r}\right)\frac{\partial P_i}{\partial t} = -\alpha_i P_i + \sum_{j=1}^{N} g_R(j,i) P_i P_j$$

$$P_i = \bar{P}_i + \Delta P_i(z,t) \;\; and \quad \Delta P_i(z,t) = m_i(z) e^{i\Omega t} \bar{P}_i \tag{3.9}$$

where $\bar{P}_i$ is the average signal power, $g_R(j,i)$ is the Raman gain/depletion coefficient between i^{th} and j^{th} signals (if $\lambda_j < \lambda_i$ then the $g_R(j,i)$>0 and $\lambda_j > \lambda_i$ then the $g_R(j,i)$<0), for $m_i(z)$ *and* Ω are the modulation index and modulation frequency, respectively. The term $\left(\frac{1}{v_i} - \frac{1}{v_r}\right)$ represents the effect of the relative group velocity of the propagating signal with respect to reference signal and the RIN transfer characteristics is highly dependent to the relative velocity between the pumps and the signals. If the relative group velocity between the signals increases, the RIN transfer is reduced especially at high frequencies via averaging effect. Thus, for the counter propagating signals, where the relative velocity $\left(\sim \frac{2}{v_s}\right)$ is much higher, the 3dB cut-off frequency of RIN transfer is readily reduced down to 1kHz compared to 1MHz for co-propagating signals. By substituting the power fluctuations $\Delta P_i(z,t)$ into the Eq. 3.11 as small perturbations, the Eq. 3.11 can be split into such two equations for average signal power and the small signal evolution [93].

$$\begin{aligned} \frac{\partial \bar{P}_i}{\partial z} + \frac{1}{v_i}\frac{\partial \bar{P}_i}{\partial t} &= -\alpha_i \bar{P}_i + \sum_{j=1}^{N} g_R(i,j)\bar{P}_i\bar{P}_j \\ \frac{\partial m_i}{\partial z} + i\Omega\frac{1}{v_i} m_i &= \sum_{j=1}^{N} g_R(i,j)P_j m_j \end{aligned} \tag{3.10}$$

As a result the RIN transfer becomes $\left|\frac{m_s(\Omega)}{m_p(\Omega)}\right|^2$ and the RIN noise power of the amplified signal accumulated over the noise bandwidth is calculated as:

$$\sigma_{RIN}^2 = (P_{in}RG)^2 \int_{\Delta f} RIN(f)df \tag{3.11}$$

The RIN performance of Raman amplifier is tested for such four different pumping configurations mentioned in Table 3.1. As illustrated in Fig 3.7, RIN transfer shows low pass characteristics. Unidirectional pumping has a single cut-off, which is much lower for all-backward pumping (~10kHz) configuration than all-forward pumping (~10MHz) configuration. On the other hand, hybrid pumping shows a step-wise low pass characteristics with two cut-off frequencies.

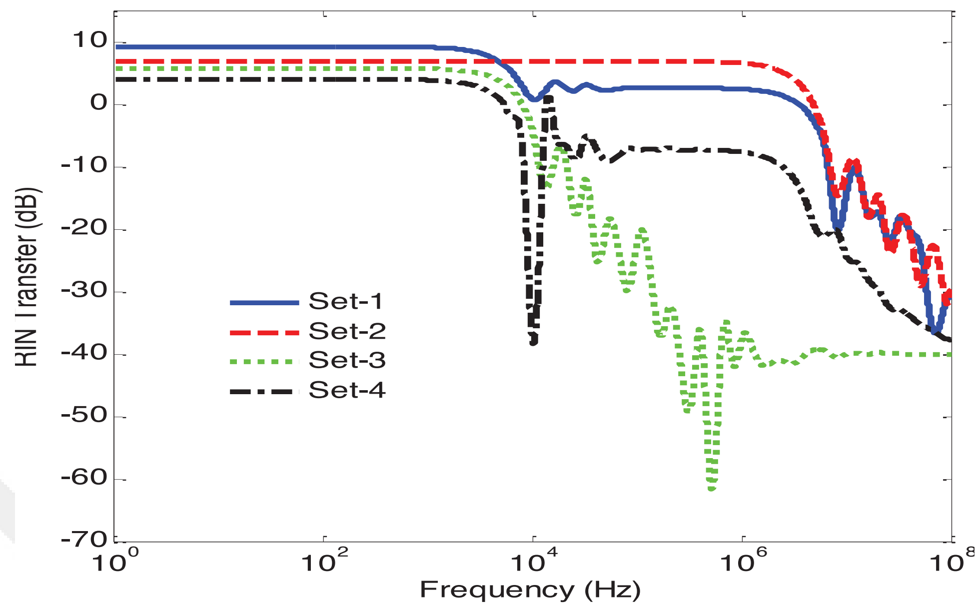

Fig. 3.7 The RIN Transfer function for the four different pumping configuration sets.

f. Double Rayleigh Backscattering (DRB)

Double Rayleigh backscattering (DRB) is one of the detrimental noise component in distributed amplifiers which is the multi-scattering process occurs in any fiber. Backscattered noise which has nearly the same spectral range experiences double scattering and interfere with the forward propagating signal. The variance of the DRB noise is calculated by

$$\sigma_{DRS}^2 = \frac{10}{9} f_{DRS}(2\alpha L + e^{-2\alpha L} - 1)\Im\{\langle|R_\epsilon(\tau)|^2\rangle\} \tag{3.12}$$

where f_{DRS} is the DRB scattering coefficient, α is the fiber loss (1/km), L is the fiber length. The $\Im\{\langle|R_\epsilon(\tau)|\rangle\}$ is the Fourier transform of the auto correlation function of electric field [94]. Using signal RIN noise components as the temporal fluctuations and substituted into Eq. 3.14, the DRB noise spectra simplifies to:

$$\sigma_{DRS}^2 = \frac{10}{9} f_{DRS}(2\alpha L + e^{-2\alpha L} - 1)\left[\Im\left\{\left(1 + \frac{1}{8}\sum_{i}^{N} m_i^2 \cos(2\pi f_i \tau)\right)^2\right\}\right]$$

$$\sigma_{DRS}^2 \approx \frac{10}{9} f_{DRS}(2\alpha L + e^{-2\alpha L} - 1)\left(\frac{\int_{\Delta f} RIN(f)df}{4}\right) \tag{3.13}$$

This DRB induced noise amplified by the distributed Raman gain causes cross-talk and constitutes one of the major source of SNR degradation in Raman-amplified lightwave systems.

3.3. System description and noise analysis

Time stretched ADC with stretch factor of 40 is designed to capture 10GHz analog signals by 12bit 250MHz high fidelity electronic digitizers. Time stretching is achieved by propagating a broadband continuum signal with 60 nm bandwidth centered at 1590nm through the two-stage dispersion compensation modules (DCMs) having the dispersion value of -32ps/nm and the -1258ps/nm, respectively [95]. In particular, the second module consists of three cascaded dispersion compensation fibers (DCFs), Fig 3.8.

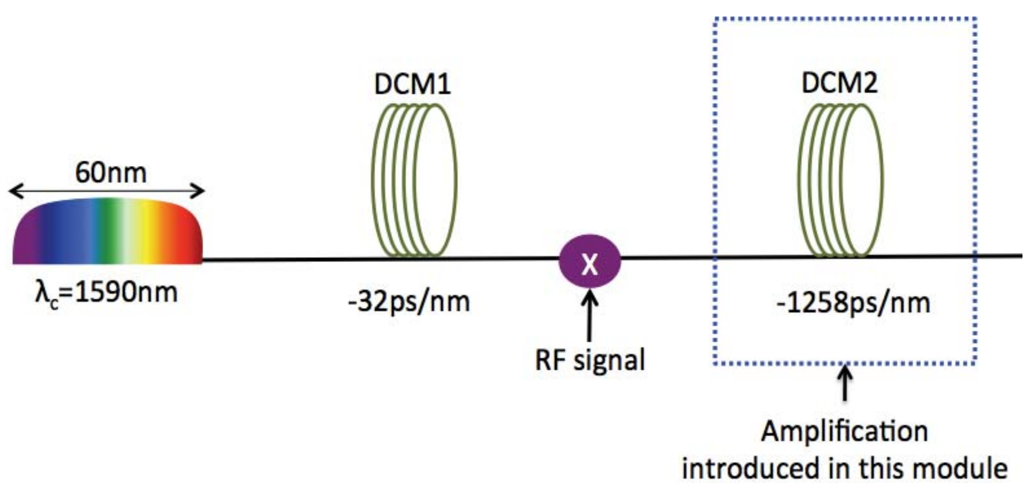

Fig. 3.8 The designed time stretched ADC with stretching factor of ~40.

The distributed Raman amplifier is designed and introduced over the second DCM, which consists of three cascaded dispersive fibers, by using six pump laser diodes in a hybrid configuration, Fig 3.9.

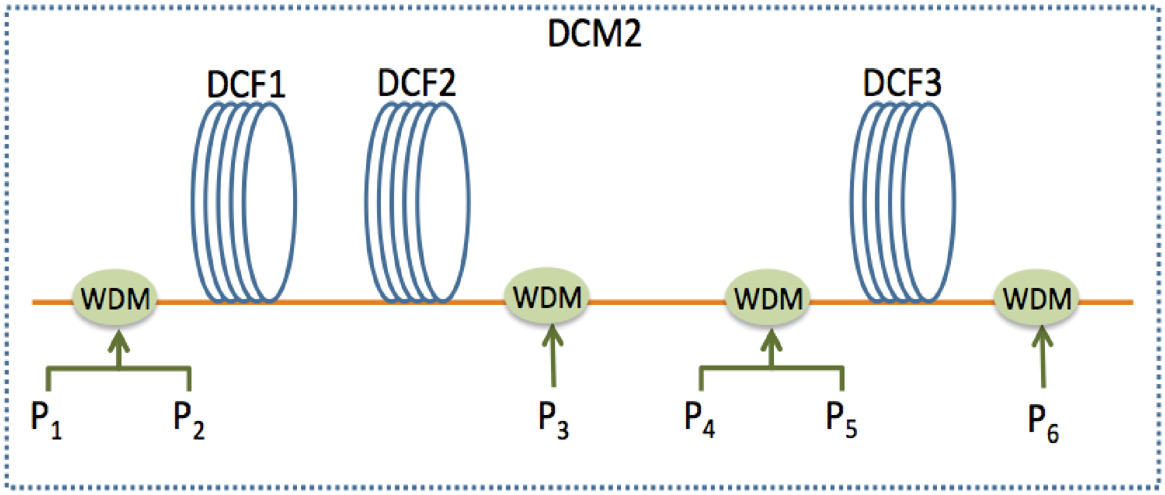

Fig. 3.9 The Raman amplifier designed over DCM2 by using 6 pump laser diodes in a hybrid configuration.

The specifications of the three dispersion-compensating fibers used both in simulation and the experiment and the optimized pump spectra including the wavelength and the power of the laser diodes are summarized in Table 3.1 and Table 3.2, respectively.

Table 3.2 Specification of Dispersion Compensating Fibers used to form DCM2.

	Dispersion	**Length**	**Fiber Loss**	**Splice Loss**
DCF-1	-658(ps/nm)	8(km)	0.34(dB/km)	0.45(dB/splice)
DCF-2	-300(ps/nm)	3.5(km)	0.30(dB/km)	0.35(dB/splice)
DCF-3	-300(ps/nm)	3.5(km)	0.30(dB/km)	0.35(dB/splice)

Table 3.3 The Pump Spectra (wavelength and the power) for 6 pump laser diodes used to in Raman amplifier.

	P1	P2	P3	P4	P5	P6
Wavelength	1505nm	1490nm	1480nm	1450nm	1470nm	1460nm
Power	50mW	150mW	90mW	330mW	160mW	280mW

Broadband gain profile over 60nm (1560nm to 1620nm) bandwidth with ~4.65dB average net gain and maximum gain ripple ~0.44dB is achieved, Fig 3.10(a). The evolution of the pump and the WDM signals (13 signal channels with 10mW spectral power) is illustrated in Fig 3.10(b). The WDM signals are mainly amplified through the first and the third shorter DCFs and stay constant along the second longer DCF, Fig 3.10(b).

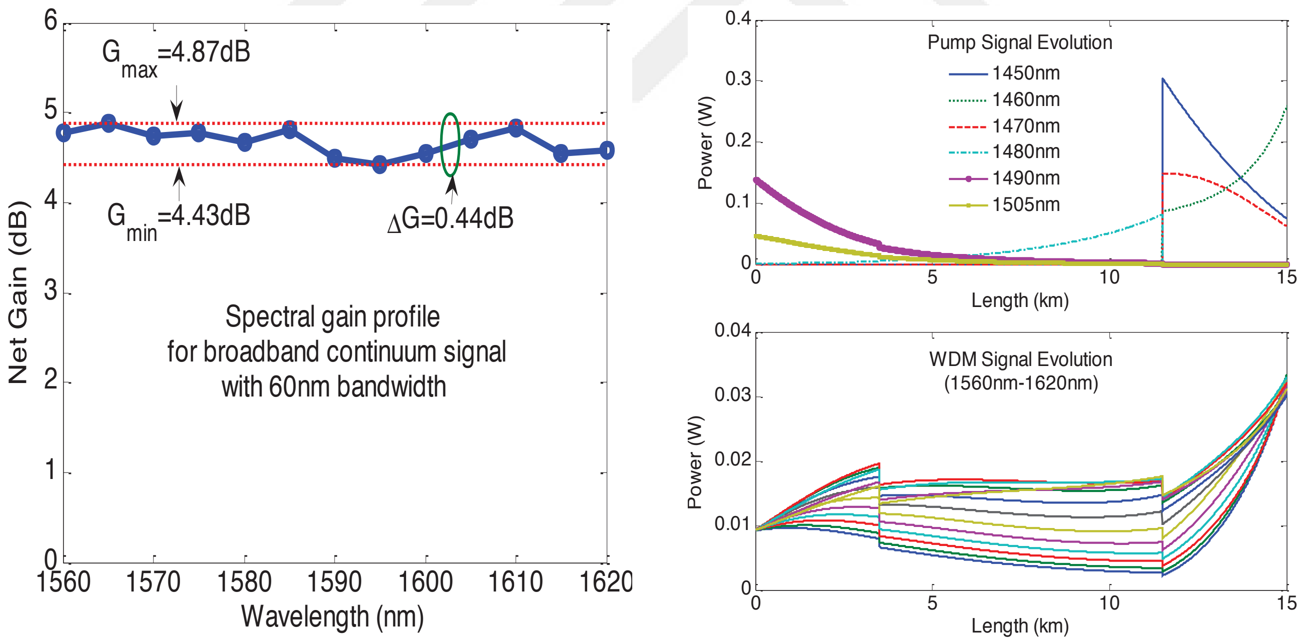

Fig. 3.10 The obtained wideband (~60nm) nearly flat (ΔG<0.5dB) spectral gain profile (a), and the pump and WDM signal evolution inside the cascaded DCFs (b).

Similarly, the same noise analysis is performed for time stretch system with discrete amplifiers. To have fair comparison, I insert discrete amplifiers that produce the same signal power at the detector as the Raman amplifier and assume 5dB noise figure for each amplifier. In the first case I assume a single EDFA with 11.5 dB gain inserted after DCF3. In the second case I insert double amplifiers after DCF2 and DCF3, Fig 3.11 [95].

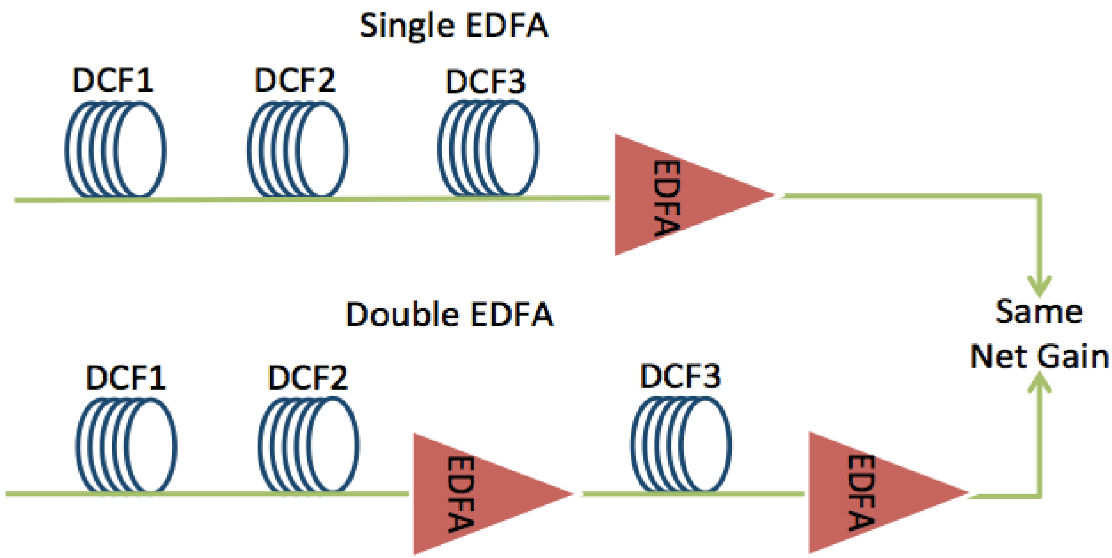

Fig. 3.11 Two alternative discrete amplifier configuration providing same net gain of 11.5dB.

3.3.1. SINAD and Noise Figure

The system performance of the ADC in terms of SNR is limited by the noise cumulated in the system from both optical and electrical sources. A deep analysis is conducted to calculate the signal to noise and distortion ratio (SINAD) and the effective number of bits, which is defined as $ENOB = \frac{SINAD - 1.76}{6.02}$, for both discrete and distributed amplification configurations [95]. Under SINAD analysis, all the noise components such as amplified spontaneous emission (ASE), relative intensity noise (RIN), double Rayleigh backscattering (DRS), quantization noise thermal noise and the shot noise are estimated individually with respect to such optical and electrical parameters shown in Table 3.4 and the system total SINAD is calculated as:

$$SINAD = \frac{(P_{in}GR)^2}{\sigma_Q^2 + \sigma_S^2 + \sigma_{th}^2 + \sigma_{ASE}^2 + \sigma_{RIN}^2 + \sigma_{DRB}^2} \tag{3.14}$$

Table 3.4 The parameters used in the SINAD analysis

Simulation Parameters	**Values**
R : Responsivity (A/W)	0.9
k_B : Boltzman constant (m^2 kg s^{-2} K^{-1})	1.38 x 10^{-23}
h : Plank's constant (m^2 kg / s)	6.626 x 10^{-34}
T : Temperature (K^0)	300
f_{DRS} : DRB coefficient	10^{-4}
R_L : Load resistance (Ω)	50
N : Number of bits	12
f_s : Sampling frequency (GHz)	3
Δf : Noise bandwidth (GHz)	1
n_{sp} : Sponteneous emission factor	1.58
m_{RF} : RF modulation index ⇒ $[1 + m_{RF}\, cos(\omega_m t)]P_{in}$	0.5

RIN transfer in distributed amplifiers has been identified as one of the main contributor for low SINAD time stretch system. Here we analyze the RIN transfer of the designed Raman amplifiers and show that RIN transfer from pump to signal varies between 6dB and 11dB over the entire 60nm bandwidth, Fig 3.12(a). In addition to RIN transfer, we individually include the contributions from double Rayleigh backscattering, shot noise, thermal noise, quantization noise and ASE noise. As indicated in Fig 3.12(b), most noise accumulation occurs at low frequencies that can be eliminated by using high pass filter such as 10MHz and 100MHz used in these simulations that limits the lower edge of the analog bandwidth of the time stretch system to 400MHz and 4GHz, respectively.

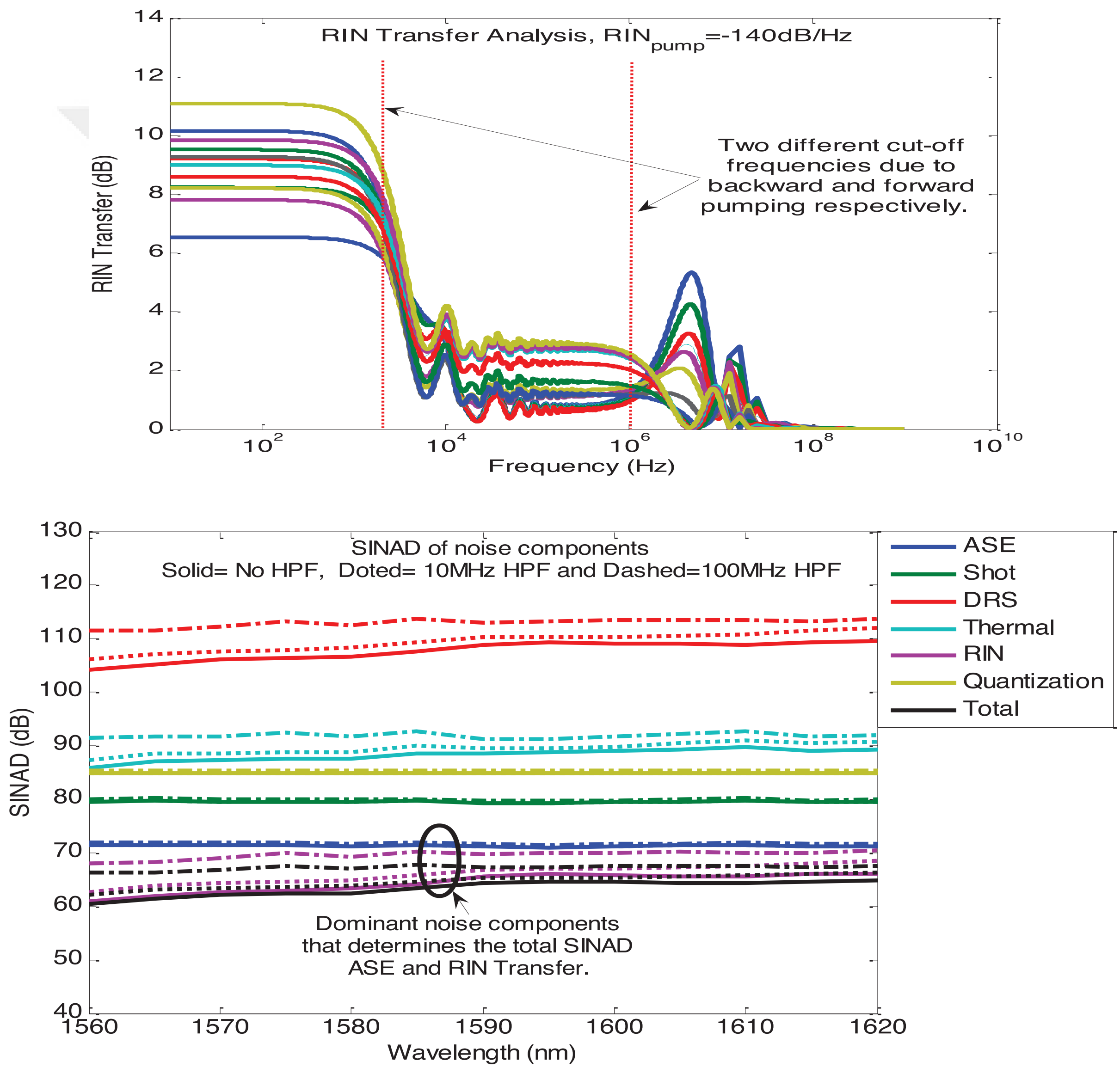

Fig. 3.12 The RIN transfer (a) from the pumps to the WDM signals in 6 pumped Raman amplifier shown in Fig 3.1(a) and the individual noise components effective in the distributed amplification (b).

Effective noise figure (NF), the SINAD and the corresponding ENOB values for distributed and discrete amplifiers are illustrated in Fig. 3.13.

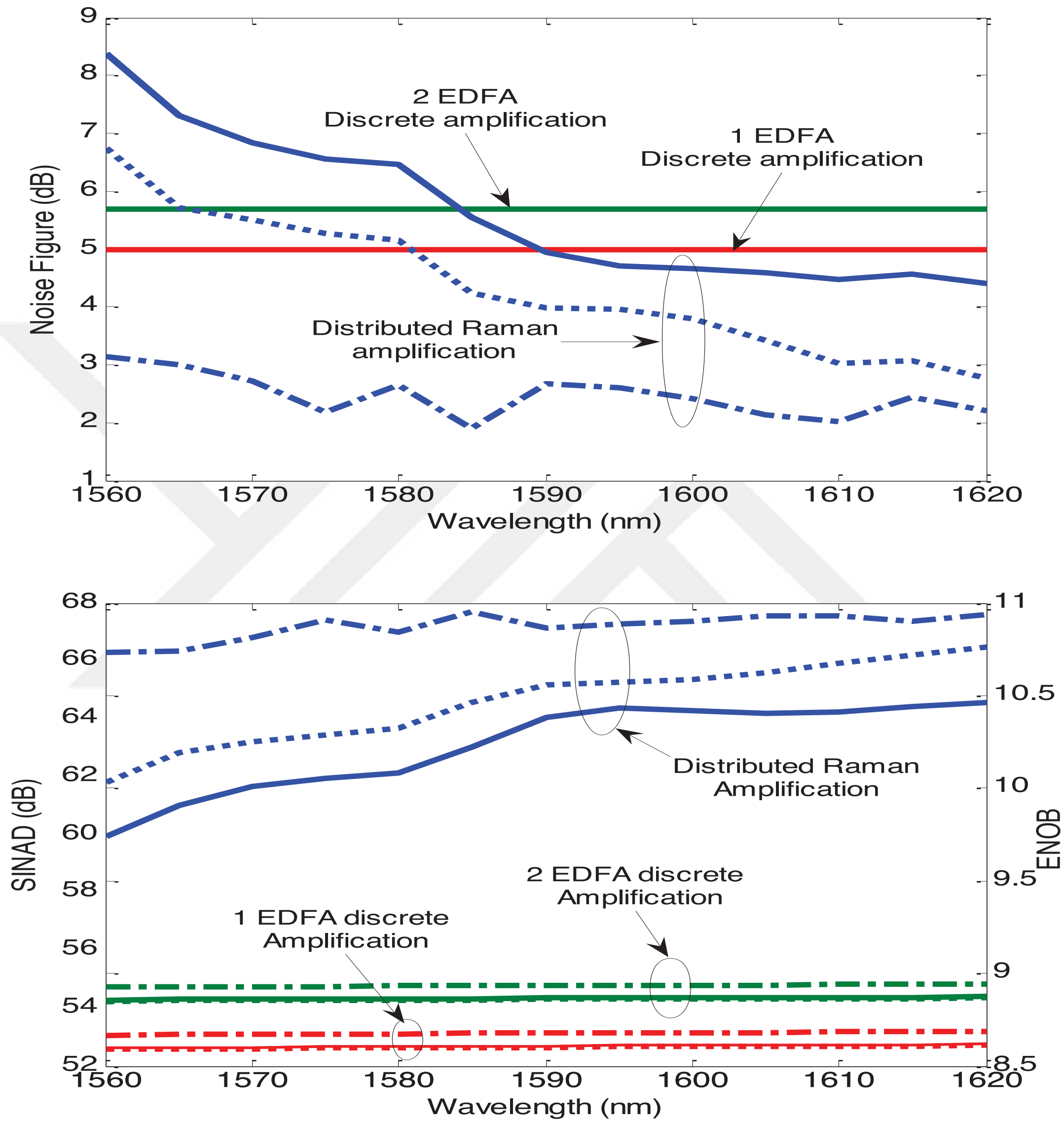

Fig. 3.13 The NF (3a) and the ENOB (3b) calculation of discrete and distributed amplification schemas for ADC with the 3GHz sampling rate, 1GHz bandwidth and 12bit quantization. Solid=No HPF, Doted=10MHz HPF, Dashed=100MHz.

SINAD values for distributed amplification vary from 60 dB to 68 dB. The biggest noise component is generated by RIN transfer from pump lasers in distributed amplification. Additionally, double Rayleigh scattering is determined to be detrimental for high ENOB systems. In discrete amplification case we obtain SINAD values of ~55dB [95]. The biggest noise component in discrete amplification is produced by ASE noise. In particular, we obtain ~16dB higher SINAD for distributed amplification that can result in ~2.5bit higher resolution, Fig 3.13(b).

3.3.2. Experimental setup and results

In addition to analytical modeling, an experimental setup is designed to characterize the distributed Raman amplifier by analyzing the gain profile and the noise performance in terms of signal to noise and distortion ratio (SINAD) and the noise figure (NF).

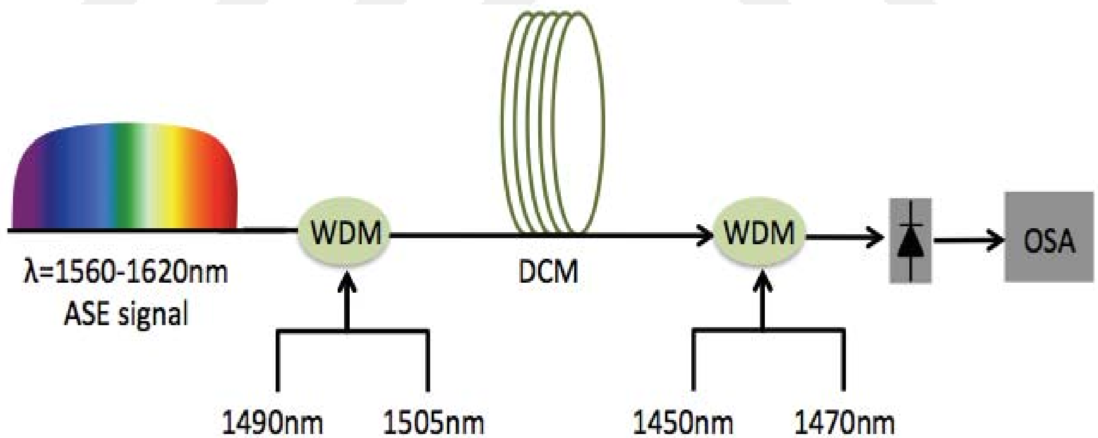

Fig. 3.14 The experimental setup for Raman amplifier characterization.

As an input either broadband or continuous wave (CW) signals are propagated through the dispersion compensating module (DCM with -1270ps/nm dispersion, 7.78km length and 3.5dB insertion loss), which represents the second dispersive unit in time stretched ADC system. Distributed Raman amplifier is designed over the DCM to obtain nearly uniform gain profile over

60nm bandwidth via utilizing four high power pump laser diodes at 1450nm, 1470nm, 1490nm and 1505nm in a hybrid configuration.

Firstly, the gain profile of the Raman amplifier is measured by using the amplified spontaneous emission (ASE) noise (>60nm bandwidth and 2.57mW average power) obtained directly from the output of EDFA as the input signal. The ~8dB on-off and 4.5dB net gain is achieved with <0.5dB ripple (highlighted in the figure inset). The sharp gain reduction around 1610nm results from the pass band characteristics (1528~1610nm) of wavelength-division-multiplexer (WDM) used in the experiment. The measured net and on-off gain profiles are illustrated in the figure.

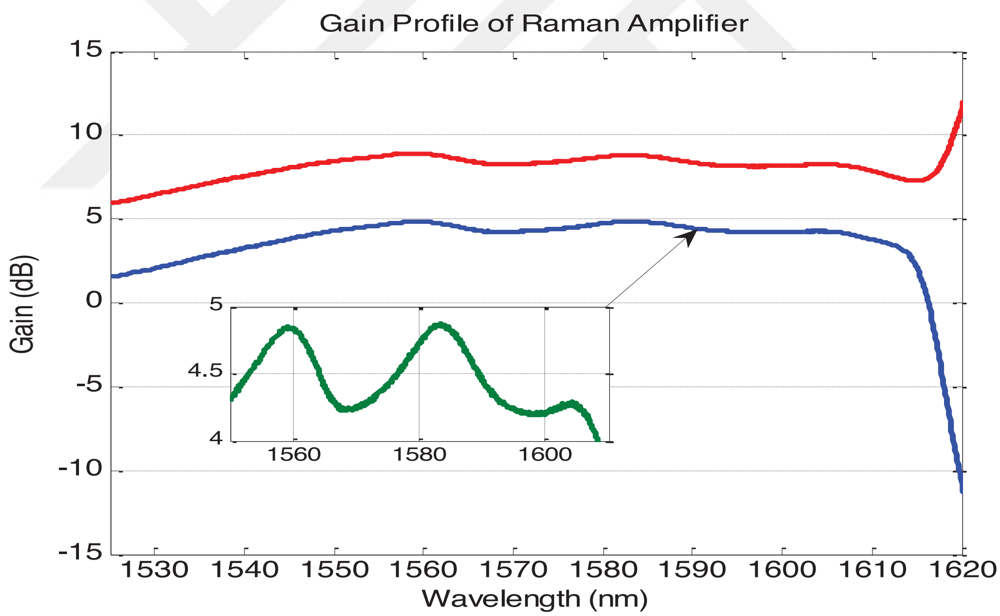

Fig. 3.15 The ~60nm broadband nearly flat gain profile of Raman amplifier with <0.5dB gain ripple.

Secondly, the noise performance of the Raman amplifier is analyzed for two continuous wave (CW) signals (at 1590nm with 3.05mW and 1.63mW peak powers). The total noise in the output signal, which results from the amplifier (RIN and ASE noise from the pumps) and the detector (shot and thermal noise), is measured by spectrum analyzer (9kHz-6.7GHz bandwidth and

1kHz minimum resolution bandwidth). As shown in Fig 3.16, the noise is mainly accumulated at low frequencies. Thus, in order to reduce the total noise in the system, we applied both electrical filtering by RF band-pass filters (low cut-off frequencies at 10MHz, 50MHz,100MHz and high cut-off frequency at 1GHz) and optical filtering especially to suppress the ASE noise by coarse wavelength division multiplexer (CWDM with~20nm bandwidth) are used.

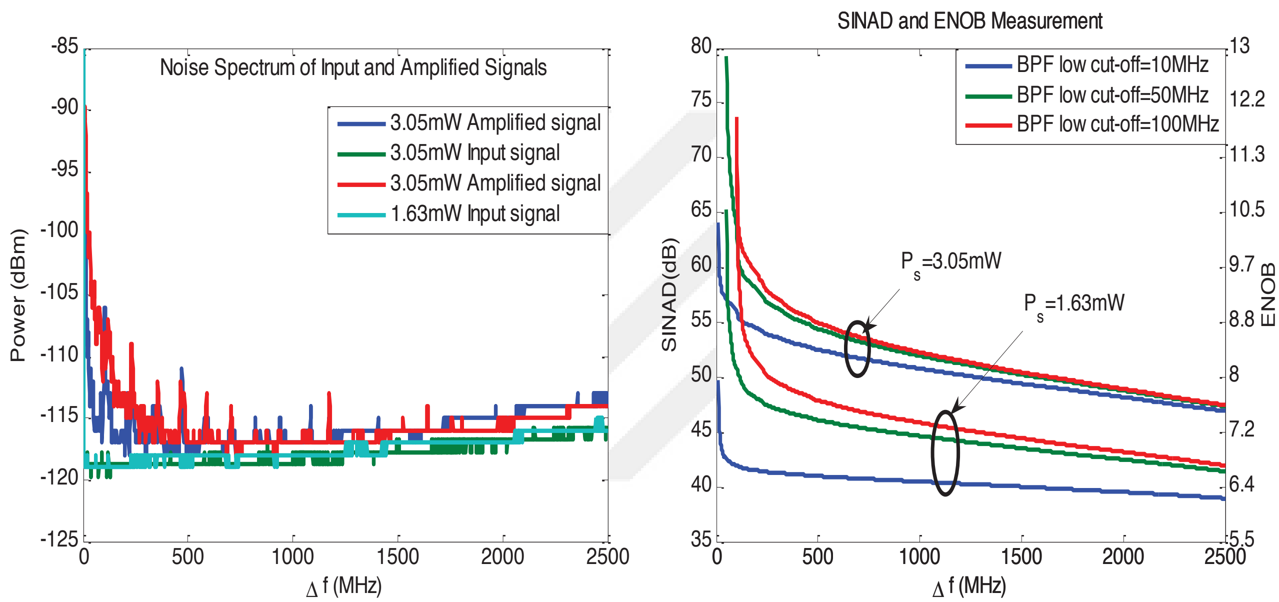

Fig. 3.16 The noise spectrum (a) and the corresponding SINAD performance (b) for amplified signals with input power of 1.63mW and 3.05mW.

As illustrated in Fig 3.17(a), SINAD is calculated for different signal powers ranging from 0.5mW to 2.5mW to illustrate the effect of signal power on SINAD. It is illustrated that ~10dB higher SINAD is achieved. Additionally, the noise figure (NF) is calculated for signals (with 1.35mW average power) at different wavelengths ranging from 1560nm to 1590nm, Fig 3.17(b). It is illustrated that ~0.5dB NF is achieved in Raman amplification as compared to ~3dB in EDFA.

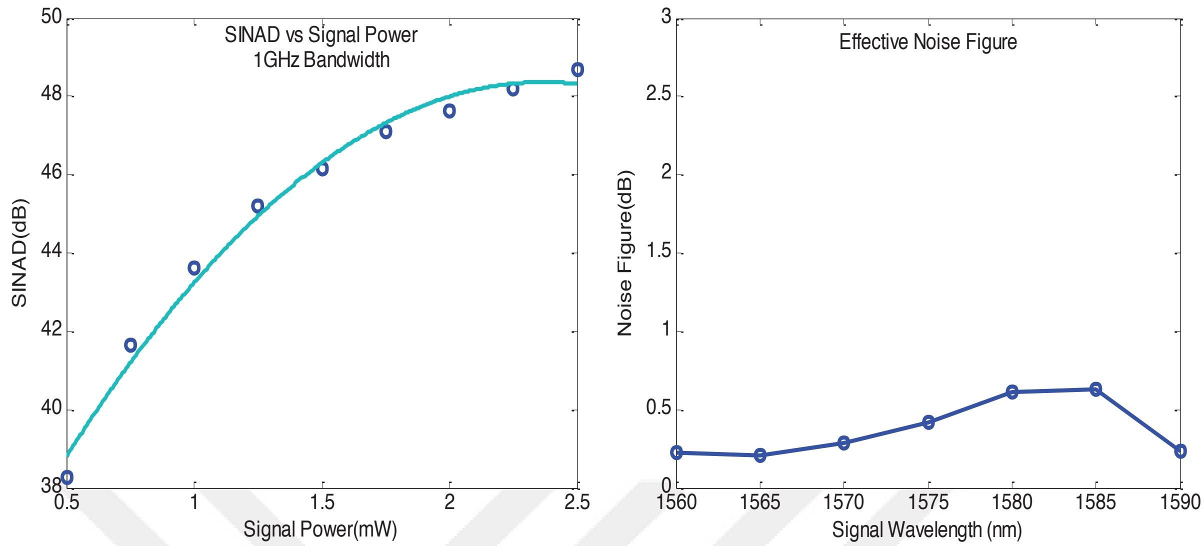

Fig. 3.17 The effect of signal power on SINAD (a) and wavelength dependency of NF (b) over 1GHz noise bandwidth.

3.4. Conclusion

In this chapter, amplified time stretched system for real time applications such as optical analog-to-digital converter, arbitrary waveform generation and dispersive imaging is analyzed in terms of the noise performance. In order to compensate the system losses and to obtain higher signal integrity, the signals such as the WDM channels in communication networks or the broadband supercontinuum pulses have to be optically amplified. Optical amplification can be implemented either by either using lumped bulky amplifiers (EDFAs are commonly used at NIR regime) at discrete positions or by using Raman amplifier which provides the gain over the system in a distributed manner.

Analytically, all the effective noise components such as relative intensity noise (RIN), amplified spontaneous emission noise (ASE), double Rayleigh backscattering noise (DRB), shot noise, thermal noise and the quantization noise accumulated through out the system are investigated individually for both distributed and discrete amplification cases. It s concluded that time stretch system with distributed amplification is mainly limited by RIN transfer and discrete amplification system is limited by ASE noise. The noise performance of time stretched system with distributed and lumped amplifications is analyzed in terms of the SINAD and the NF. Overall, the distributed amplification in time stretch system with >10GHz analog bandwidth exhibit up to 16dB higher SNR corresponding to ~2.5 bit higher resolution and ~3dB less NF.

In addition to analytical modeling, a flat ~60nm broadband Raman amplifier is demonstrated experimentally. To test the noise performance, the variation of SINAD with respect to signal power ranging from 0.5mW to 2.5mW is calculated and ~10dB higher SINAD is achieved. Additionally, the noise figure (NF) is calculated for signals (with 1.35mW average power) at different wavelengths ranging from 1560nm to 1590nm. It is illustrated that ~0.5dB NF is achieved in Raman amplification as compared to ~5dB in EDFA.

CHAPTER 4

Fast arbitrary waveform generation by using digital micro-mirror arrays

4.1. Introduction

Arbitrary waveform generators (AWGs) find many applications in wide range of fields varying from wideband communication and instrument diagnostics to remote sensing and radar systems. Photonic AWGs provide wider bandwidth and higher dynamic range resolution and hence can complement the electronic AWG techniques in many applications [96-97]. Various photonic techniques which significantly improve the current state of art millimeter wave and microwave AWG have been proposed and demonstrated. The narrow band techniques which enable to generate tunable gigahertz waveforms through RF interference by employing a tunable laser diode source, electrooptic modulator, and fiber delay lines [98] and through beating of different longitudinal laser modes, which are independently phase or amplitude modulated to produce arbitrarily shaped beat signals, by utilizing mode-locked laser diode combined with a wavelength-division-demultiplexing [99] have been demonstrated. Using arrayed waveguide grating as a wavelength-division-multiplexing (WDM) scheme with a series of optical attenuators and delay lines as well permits to achieve amplitude and phase modulated gigahertz RF waveforms [97]. This technique, however, requires adapting the wavelength selective delay lines for each specific RF waveform and thus complicates the reconfigurability. In addition, all-fiber based methods such as temporal pulse shaping, spectral shaping and microwave filtering followed by frequency-to-time mapping have been recently proposed to generate desired RF waveforms [100-102]. Moreover, free space AWG techniques using high rate tailored pulse sequences produced through the direct space-to-time pulse shaper which generates amplitude equalized and frequency modulated RF waveforms up to 50 GHz [103] and time stretched reprogrammable system which produces waveforms up to 10GHz [104] by shaping the spectrum of the broadband source spatially after being mapped over the modulator have been previously demonstrated. In these spatial techniques, light modulation relies on the programmable liquid crystal horizontal pixel arrays that can control the amplitude and phase of the incident light which are limited by the slow response on a time scale of milliseconds [104-105].

Recently, new digital micro-mirror device (DMD) based on the DLP™ technology (Texas Instruments, Dallas, TX) has been commercialized and it has the enabling capability of two dimensional mapping and modulation via 2D pixel arrays, high resolution, high reflection, exceptional stability and excellent controllability over thousands of individual micro mirrors [106]. Up to date MEMS micro-mirror arrays have been proposed for such many application as programmable imaging, display technologies, spectroscopy, microscopy, 3D metrology, and maskless lithography [107-109]. However, use of such devices for arbitrary waveform generation has not been utilized.

In this chapter, a novel method for all optical RF arbitrary waveform generation (AWG) that utilizes DMD technology is proposed and experimentally demonstrated. First I will introduce the digital micro-mirror device (DMD), its operation principles, optical properties and superiority over other types of spatial light modulators (SLM) especially the commonly used liquid crystal (LC) technology. Then, I will discuss the detailed procedure that is used in AWG and provide analytical modeling. In particular, I will discuss the limits of the proposed technique based on currently available digital mirror technologies. The achievable temporal resolution, repetition rate, modulation index and the rise/fall times of the final waveform are calculated as figure of merit. It has been showed that reducing the diffraction limit by increasing the ratio of beam size to lens focal length (>0.075) and spatial modulation down to single mirror pitch size (10.8μm), waveforms up to 18GHz repetition rates with high reconfigurability rates beyond 32.5kHz, >90% modulation index and <100ps rise times can be achievable by utilizing -675 ps/nm dispersion [110]. Finally, an experimental setup is designed for proof-concept demonstration of AWG and 120MHz to 280MHz sawtooth and 120MHz to 580MHz square waveforms are generated [111-112]. Additionally, the experimental results are compared with theoretical estimates on generated square and sawtooth waveforms at 120MHz and 160MHz, respectively to show that the analytical estimates match the experimental results.

4.2. Digital Micro-mirror Device (DMD)

Digital micro-mirror device (DMD), a pixelated MEMS device based on extremely powerful and flexible DLP^{TM} technology (Texas Instruments, Dallas, TX), is an array of individually addressable opto-electro mechanical pixel units. Each pixel unit is compromised of aluminum micro-mirror, mechanical assembly and the control electronics, Fig.4.1. The mechanical assembly includes metal-3 layer, torsion hinge and the yoke. The micro-mirror is connected to yoke through the mirror post. The yoke, which is the base for the mirror, rotates over the two torsion hinges (diagonally placed) due to electrostatic attraction between the electrodes on the yoke and the metal-3 layer [113-115]. The metal-3 layer is the bottom layer landing on the memory cell composed of metal pads and mechanical stops (position determines the maximum angle of rotation) and enables the electrostatic attraction of the yoke, namely the tilting of the mirror according the state of memory cell. The state of each mirror is controlled by corresponding dual complementary metal oxide semiconductor

(CMOS) based static random-access (SRAM) memory cell. When CMOS SRAM is loaded with the binary data, the electrodes on the metal-3 layer are charged accordingly to produce electrostatic attraction of yoke and as well the mirror elements to rotate in the specific direction [113-114].

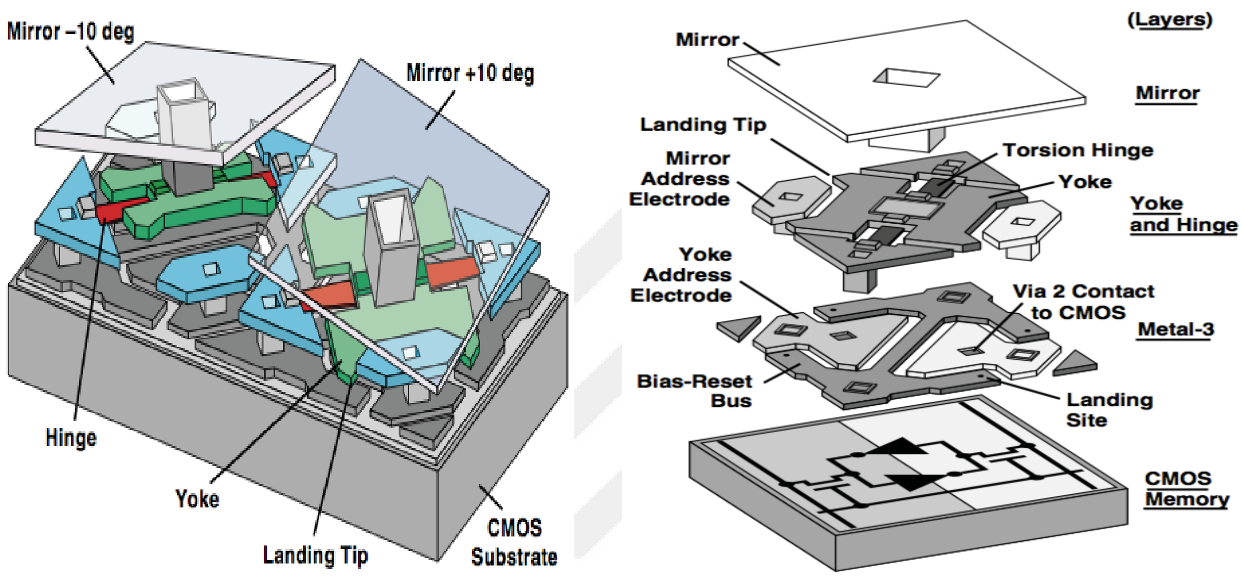

Fig. 4.1 The mechanical and electrical control assemblies of the digital micro-mirror memory cell [114].

The performance of the DMD is considered with respect to the capability of controller board in terms of the achievable frame rate and the physical properties of micro-mirrors in terms of the size, maximum tilt angle and the mirror pitch size. The DLP™ technology has substantially advanced over the years to achieve higher dimensions, higher speeds and better resolution [106]. The currently available MEMS mirror technology can provide down to 7.56µm pitch size and up to 1920x1080 array size. Various DMD chipsets have been commercialized with properties listed in Table 4.1.

Table 4.1 The currently available DMD chipsets [106].

Chipset	Mirror Pitch size	Mirror Tilt angle	DMD Array size
0.17 HVGA	7.56μm	12^0	480x320
0.55 XGA	10.8μm	12^0	1024x768
0.3 WVGA	7.6μm	12^0	608x684
0.7 XGA	13.6μm	12^0	1024x768
0.95 1080p	10.8μm	12^0	1920x1080

4.2.1. The Operation of DMD

The digital micro mirror device (DMD) reflects the incident light through the specific direction via changing the orientations of the micro-mirrors. Each micro-mirror can generally be assigned to such three different states defined as the flat, ON and OFF. Loading with binary data and applying the bias voltage (typically 5V) into the CMOS SRAM memory cell, DMD can switch the micro-mirrors between the pre-defined states. The flat state is the neutral position (0^0) of the mirror when there is no bias voltage and the ON-OFF states respectively correspond to position of mirror tilted either $+\theta_T$ or $-\theta_T$ degrees (typically 10^0 or 12^0) [15-116]. The reflected light deviates $+/-2\theta_T$ degrees from the specular reflection (in the flat state) for the ON/OFF state orientations, Fig 4.2.

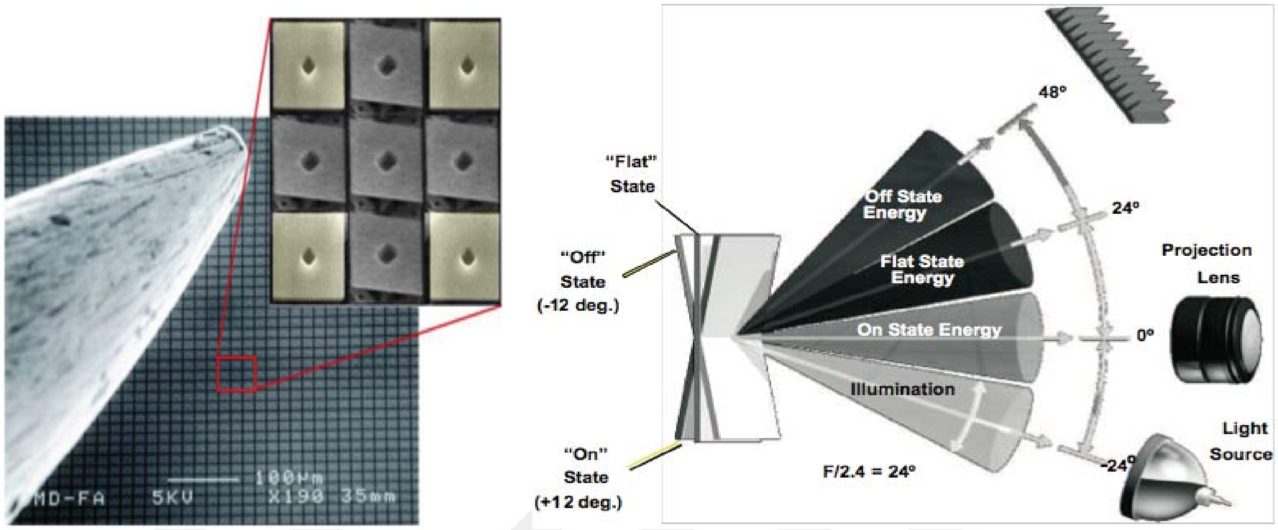

Fig. 4.2 The microscopic view (a) of DMD and the micro-mirrors in two different states. The optical function (b) of 12^0 micro-mirror tilt device [116].

Any desired illumination can be displayed by loading the DMD with appropriate image patterns. The black and white projection, for example, can be easily generated by using simple binary image patterns where the micro-mirrors are statically assigned either to ON or OFF states. On the other hand, gray scale intensities can be generated by dynamically switching the micro-mirrors between ON-OFF states and adjusting the percentage of time the mirror is at each state, namely by using pulse width modulation (PWM), during the refresh time. The N bit binary PWM system can be designed to obtain 2^N gray scale intensities where each i^{th} significant bit covers $2^{i-1}/(2^N-1)$ percentage of time. In order to obtain gray scale intensities quantized between 0 and 1, the binary code representation is employed over the PWM system as shown in the Fig 4.3 [114, 117].

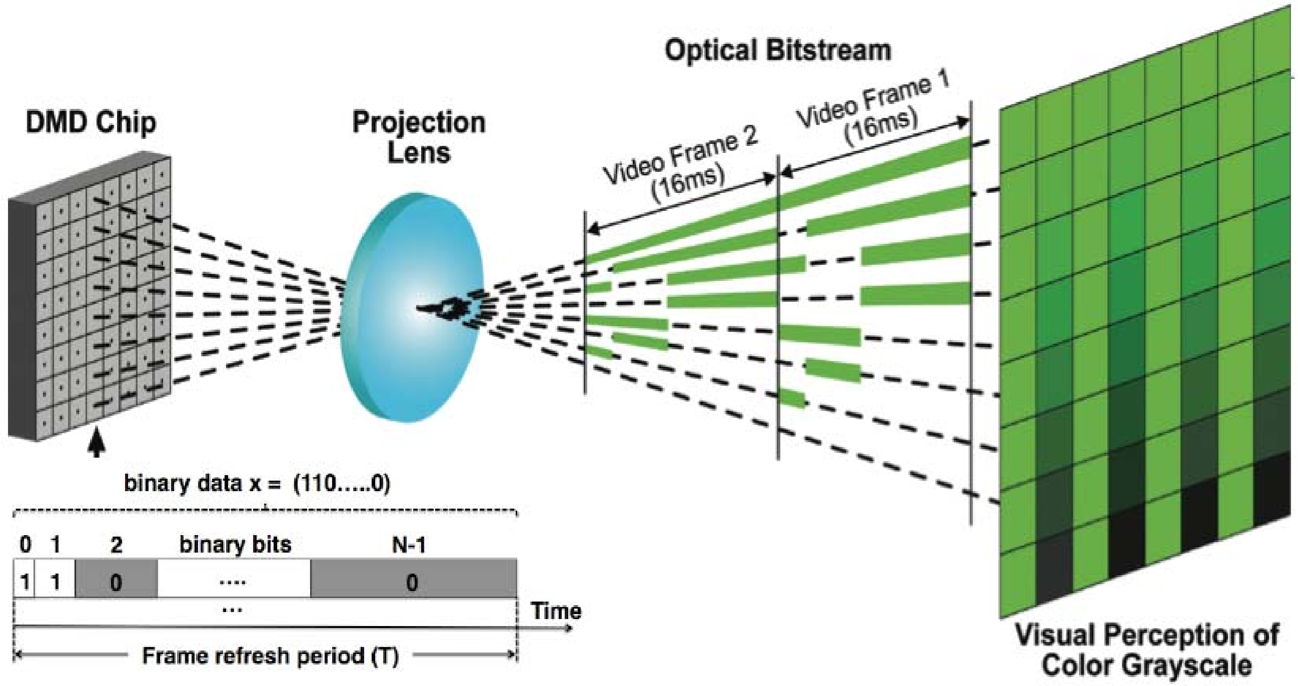

$$\text{grayscale intensity} = \frac{\sum_0^{N-1} x(i)\, 2^i}{\sum_0^{N-1} 2^i}$$

Fig. 4.3 The binary N bit PWM system designed to obtain grayscale intensity levels [117].

4.2.2. Optical Properties of DMD: Advantages and Disadvantages

DMD is a micro-optical device designed to be used as a digital spatial light modulator by providing much better optical performance in terms of speed, feasibility for broadband illumination, active area, contrast ratio and the diffraction efficiency than the other types of SLMs [118]. The main advantages and the deficiencies of the DMD in comparison to most commonly used liquid crystal display (LCD) technology are listed below:

Advantages :

1. With the recent MEMS micro-mirror technologies, up to 32.5 kHz pattern rate with a fast switching speed of approximately <30μs between the states allowing for fast display of

illumination patterns can be achieved compared to time scale of milliseconds for LC based SLMs.

2. The LC-SLM is a transmissive device causing more attenuation due to back reflection from cascaded glass layers and the absorbtion. Since the DMD is a reflective surface and the micro-mirrors are tightly inbuilted on the chipset with ~1µm gap in-between, the DMD can provide higher fill factor (ratio to pixel size of 10.8 µm) of %90 than the LC-SLM with %70.
3. The DMD can provide 6.6 times higher power transfer efficiency, which the ratio of reflected irradiance to incident irradiance, than the LC-SLMs which, as a result, makes DMD more suitable for high power applications and proportionally reduces the typical exposure time for the same irradiance.
4. The DMD performs ~11 times and ~ 3.3 times higher contrast ratio, which is defined as the ratio of maximum flux to minimum flux at the diffuser, for projected and holographic images, respectively.
5. The DMD generated images show slight artifacts mainly at the edges of micro-mirrors, however the LC-SLM generated images show much noticeable artifacts due to interference of multiple reflections from cascaded glass layers of the LCD.
6. The pixelated structure of both DMD and LC based spatial light modulators functions as a diffraction grating. The tilted surface due to states of micro-mirrors turns the DMD into a blazed diffraction grating with a blaze angle of θ_T (tilt angle). Thus, when illuminated at blaze angle (blaze condition $\alpha=\beta$) as twice as higher diffraction efficiency of %88 can be obtained than the LCD device.

7. DMD due its mirrored surface is capable of modulating broadband light ranging from ultraviolent (UV) to near infra red (NIR) wavelengths. The DMD mirrors are also protected by a cover glass, which is coated to operate for desired spectral window.

Disadvantages:

1. The DMD due its being reflective device can enable only amplitude modulation, however, the LC-SLMs can be used both in reflection and transmission modes enabling both amplitude and phase modulation.
2. The DMD mirror array as a 2D blazed diffraction grating with period of mirror pitch size (typically 10.8μm-13.6μm) distributes the incident beam into diffraction orders. The tilt of the micro-mirrors (orientation at ON or OFF state) has no effect on the diffraction grating (the number and the position of the diffraction orders stays fixed). The state of the micro-mirrors only changes the corresponding power distribution over the diffraction orders due to change in the angle of specular reflection. The diffractive nature of DMD causes degradation in the coupling efficiency and the higher diffraction orders creates interference patterns, which appear as background noise, for especially broadband applications [118].

4.3 AWG configurations and theoretical analysis

We investigated the optically assisted AWG system, which is mainly designed by combining the broadband illumination, wavelength-to-time mapping, space-wavelength mapping and spectral shaping modules, Fig 4.4. The supercontinuum (SC) pulses centered at 1590nm are used as 20nm wide broadband source to capture the spectral modulation that is transformed into RF signals after time wavelength mapping [105]. In the first stage, the broadband SC pulses are propagated through the dispersion compensation module (DCM) with -675 ps/nm dispersion to map the spectral information into temporal waveform. Then, the spectral content of the time stretched SC pulses are mapped over the focal plane by diffractive optics which is composed of a blazed diffraction grating with 600 lines/mm grove density and a Fourier lens with 200mm focal length to collimate the dispersed wavelengths and to focus the beam for better resolution. After being mapped over the focal plane, the spectrum of the pulses is shaped by 1024 X 768 micro-mirror arrays used as a digital spatial light modulator. The pattern on the DMD is electronically tunable and the pattern is set according to the desired waveforms. The temporally and spectrally modulated signals are captured by an optical detector connected to a real time oscilloscope [110-112].

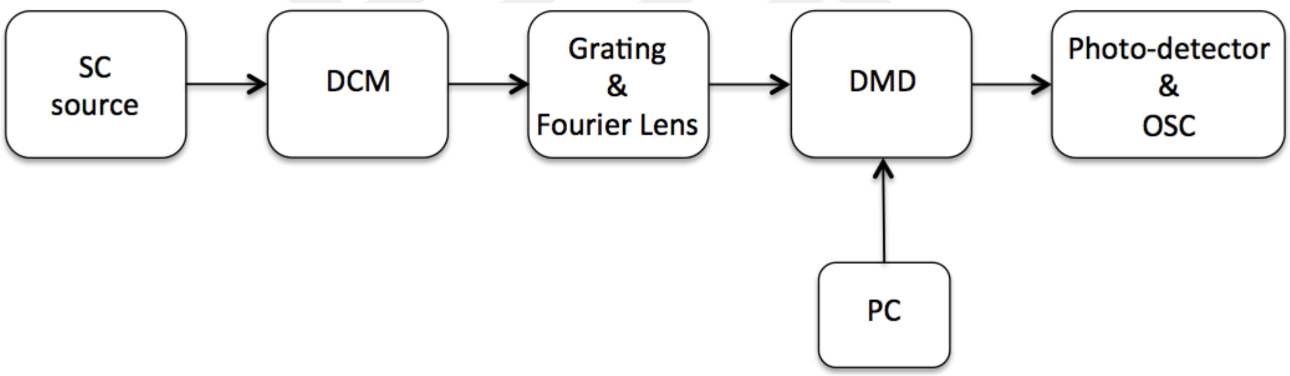

Fig. 4.4 Functional block diagram for all-optical arbitrary waveform generation by using micro-mirror arrays. SC: Supercontinuum, DCM: Dispersion compensating module, DMD: Digital micro-mirror device, PC: Personal computer, PD: Photo detector, OSC: Oscilloscope.

4.3.1 Resolution Analysis

The resolution of the proposed AWG system is analyzed in terms of the spatial and spectral resolution of the pulse shaping module [9-10] and the temporal resolution of the detection system to assess the limit on the achievable RF waveforms. The pulse shaping mechanism is the key module of the proposed AWG system and consists of space wavelength mapping, namely the spatial dispersion of wavelengths via diffractive element, and the focusing system which focuses the collimated beam on to the spatial light modulator by a cylindrical lens [104-105]. The spatial resolution of the focusing system, namely the minimum focal size, limits the smallest detectable feature on the image plane (refers to DMD). Due to the diffraction limit, the spatial resolution depends on the wavelength (λ), the focal length (f) of the Fourier lens and the beam size (d) which is defined as the aperture diameter if the plane wave is considered or the spatial full width at half maximum width (FWHM) if the Gaussian wave is considered, Fig 4.5(a). Here, we analyzed the spatial and spectral resolution performance of the pulse shaping module for both plane $E_p(x,d) \propto rect\left(\frac{x}{d}\right)$ and Gaussian waves $E_g(x,w) \propto exp\left(-\frac{x^2}{2w^2}\right)$ where $w = \frac{d}{2\sqrt{\ln(2)}}$. The intensity distribution of the focused beams at the image plane is calculated by Eq. (1) as:

$$I\left(x,\lambda_i,\frac{d}{f}\right) \propto \left\{ \begin{array}{ll} exp^2\left[-\frac{\pi^2\left(x-x_{pi}\right)^2}{2\ln(2)\lambda^2}\left(\frac{d}{f}\right)^2\right] & ,Gaussian\ wave \\ \sin c^2\left[\frac{\left(x-x_{pi}\right)}{\lambda}\left(\frac{d}{f}\right)\right] & ,Plane\ wave \end{array} \right\} \tag{1}$$

Here $x_{pi} \approx \frac{G}{\cos(\beta)} f(\lambda_i - \lambda_c) = G_\beta f(\lambda_i - \lambda_c)$ is the relative position of the first order diffraction peak for the wavelength λ_i with respect to the central wavelength λ_c. The $G_\beta = \frac{G}{\cos(\beta)}$ is the effective groove density defined as a function of 1st order diffraction angle (β). For the beam with wavelength (λ) and the incident angle (α), the first order diffraction angle (β) is calculated by the well known grating equation written as $\sin(\alpha) + \sin(\beta) = \lambda G$ which reduces to $2\sin(\beta) = \lambda G$ in a Littrow configuration$(\alpha = \beta)$. The spatial resolution (Δx) is defined as the full width at half maximum (FWHM) width of the focused beam. The spectral resolution (Δλ), on the other hand, is defined as the minimum wavelength separation corresponding to spatially focused beams, which are dispersed to a detectable spatial separation of Δx [110].

$$\Delta x \approx \begin{Bmatrix} \dfrac{2\lambda f}{d\pi}\ln(2) & ,Gaussian\ wave \\ \dfrac{2 * 1.39156\ \lambda f}{d\pi} & ,Plane\ wave \end{Bmatrix},$$
$$\Delta\lambda \approx \frac{\Delta x}{G_\beta f} = \begin{Bmatrix} \dfrac{2\lambda}{G_\beta d\pi}\ln(2) & ,Gaussian\ wave \\ \dfrac{2 * 1.39156\ \lambda}{G_\beta d\pi} & ,Plane\ wave \end{Bmatrix} \quad (2)$$

As calculated by Eq. (2), the spatial resolution is a function of the diffraction parameter (r), which is defined as the ratio of the beam size to the lens focal length, (d/f). The Fig 4.5(a) illustrates the spatial resolution (minimum detectable feature) achieved for both plane and Gaussian beams with respect to different "r" values (r=0.001 to 1). The spectral resolution, however, only depends on the beam size and the effective groove density of the diffraction grating. Since the spatially encoded spectral modulation is mapped to a temporal modulation via dispersive Fourier transformation through the DCM, the spectral resolution designates the temporal resolution of the generated arbitrary waveforms. By neglecting the higher order dispersion terms, namely assuming a uniform dispersion over a wide spectrum, the temporal mapping is modeled linear as $\Delta t \approx \Delta\lambda * D$. In addition to these, the temporal resolution of the AWG system is ultimately limited by the detection system that converts the optical signal into electrical waveforms. Here, the temporal resolution is mainly limited by the RF bandwidth of the photodetector and the electronics following the detector. The Fig 4.5(b) illustrates the spectral resolution and corresponding temporal resolution (via using DCM with -675ps/nm dispersion) for different beam size (0.4mm to 20mm) and the effective groove density (600, 900 and 1200 lines/mm) combinations.

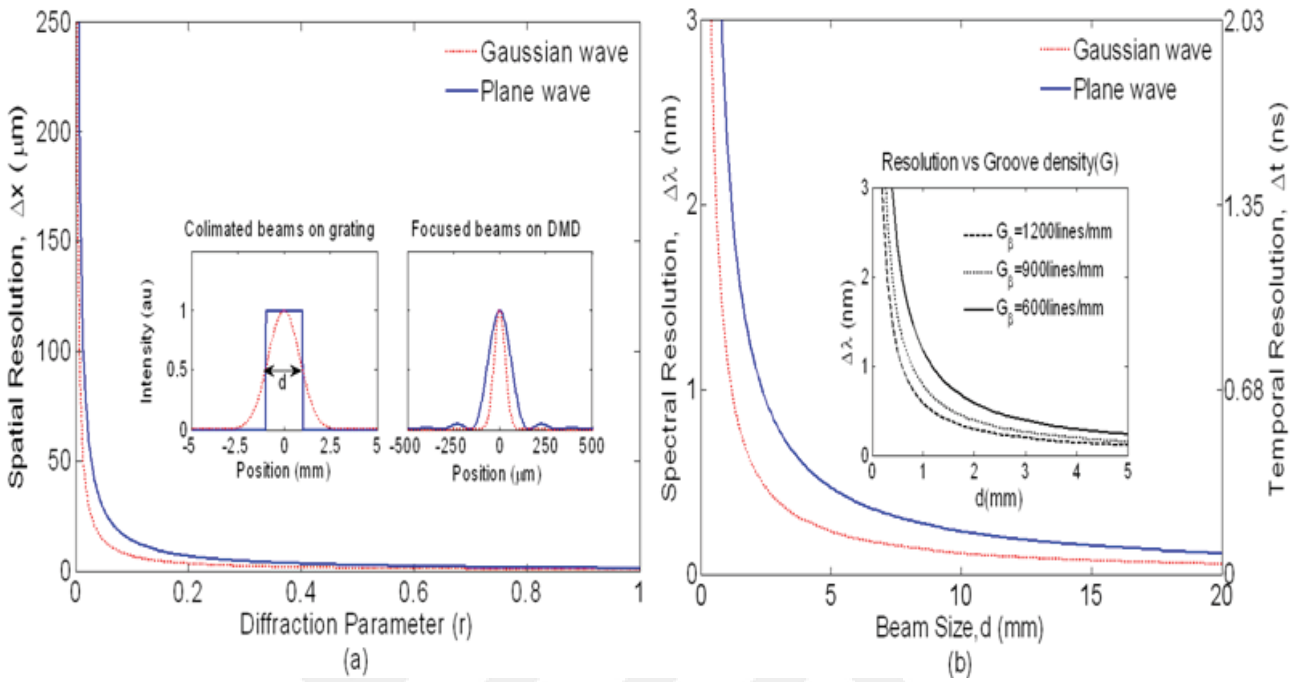

Fig. 4.5 The spatial resolution of the space-wavelength mapping (a) with respect to diffraction parameter (d/f) and the spectral /temporal resolution (for D= -675ps/nm) with respect to the beam size, d and the effective groove density, G_{β}.

4.3.2 Spatial Light Modulation

The spatial light modulator is placed at the focal plane to shape the spectrum of the broadband source properly for the desired waveform. The approach we propose uses the MEMS based micro-mirror arrays as a digital spatial light modulator. The particular DMD considered in the experimental setup and in these analytical calculations is a 0.55-inch diagonal mirror arrays consisting of 1024x768 individually addressable aluminum micro mirrors with 10.8μm pitch size, Fig 4.6(a). Each mirror can be assigned to discrete states of ON (+12^{o} rotation) or OFF (-12^{o} rotation), which can be refreshed at a frame rate of 5 kHz, to control the direction of light [106]. The DMD mirrors are also protected by a cover glass, which is coated to operate for desired spectral window [108]. Among these the frame rate is particularly important and it determines the ultimate rate at which we can reconfigure the whole waveform and also the maximum temporal width of a waveform package, as long as the laser repetition rate is adjusted accordingly. With the recent MEMS micro-mirror technologies, up to 32.5 kHz pattern rate with a fast switching speed of approximately 30µs between the states allowing for fast display of illumination patterns can be achieved.

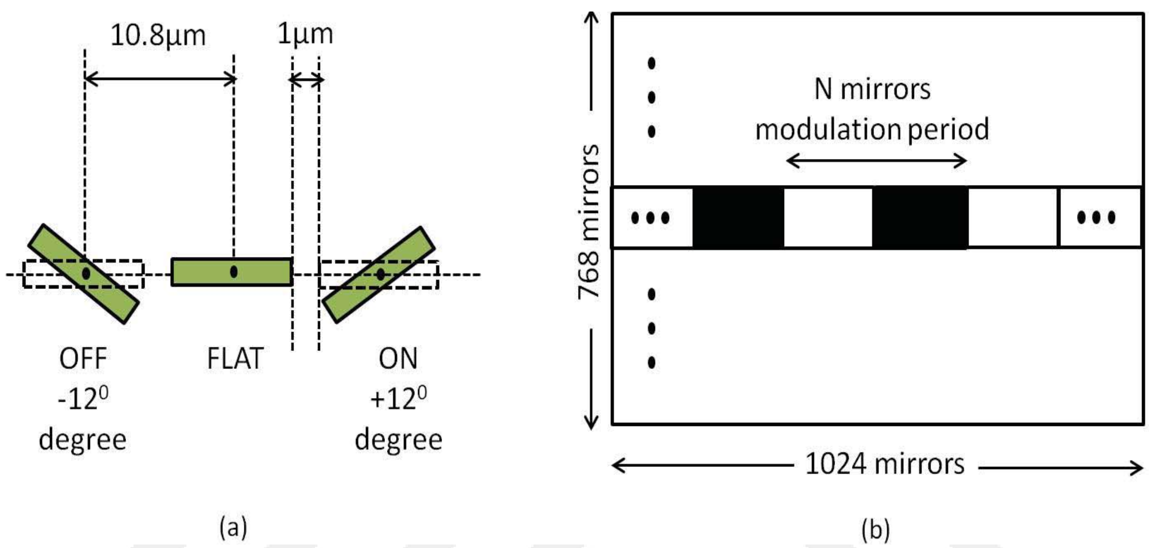

Fig. 4.6 The micro mirrors inbuilted on DMD with having 10.8 microns pitch size and ~1micron gap in between (a) can be oriented with high precision and speed at -12 or +12 degrees [14]. A sample (b) implemented ON-OFF modulation pattern on DMD [119].

a. Square Waveform Generation

In order to generate an arbitrary waveform with a desired shape and frequency binary image patterns are created on the DMD to set the states. The shape of the waveform corresponds to the image of the binary pattern. For instance, in order to generate square waveforms binary image patterns similar to the samples shown in Fig 4.7 are fed into the DMD. These vertical strip type patterns with varying spatial frequency (in terms of the number of mirrors) function as a periodic rectangular spectral filter. Black lines correspond to the OFF state of mirrors and white lines correspond to ON state of mirrors [110-112].

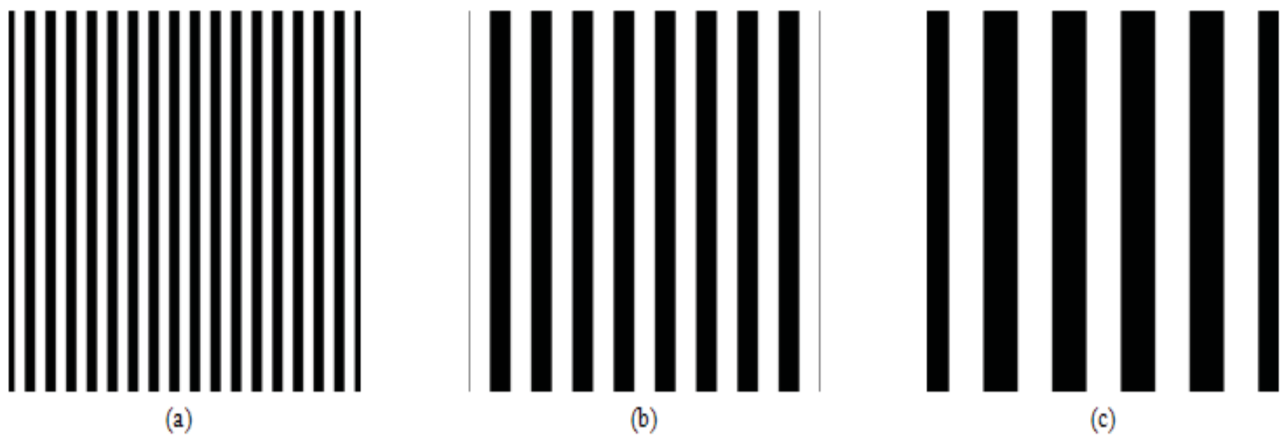

Fig. 4.7 The sample binary image patterns created on DMD to generate square waveforms with different spatial frequencies. Patterns with spatial period of 60mirrors/period(a), 120mirrors/period(b) and 200mirrors/period(c).

By carefully selecting the bandwidth of SC pulses we can generate periodic waveforms encoded on a single laser pulse. Using parallel system or utilizing the different diffraction orders from the digital light mirrors, on the other hand, waveforms which appear longer period of time, namely aperiodic with respect to laser repetition rate can also be generated. The frequency of the generated RF waveforms on a single pulse is basically determined by the spatial light modulator and the dispersive unit. As illustrated in Fig 4.8(a) that decreasing the pattern's spatial modulation down to single mirror pitch size (10.8μm) and using gratings with higher groove density improves the spectral allocation (up to 18GHz temporal repetition rates can be achieved by -675ps/nm) so that further by using lower dispersion DCMs (~17 times higher modulation rates can be obtained by using -40ps/nm dispersive fiber as employed in [105]), the temporal frequency of the output waveforms can be increased [110].

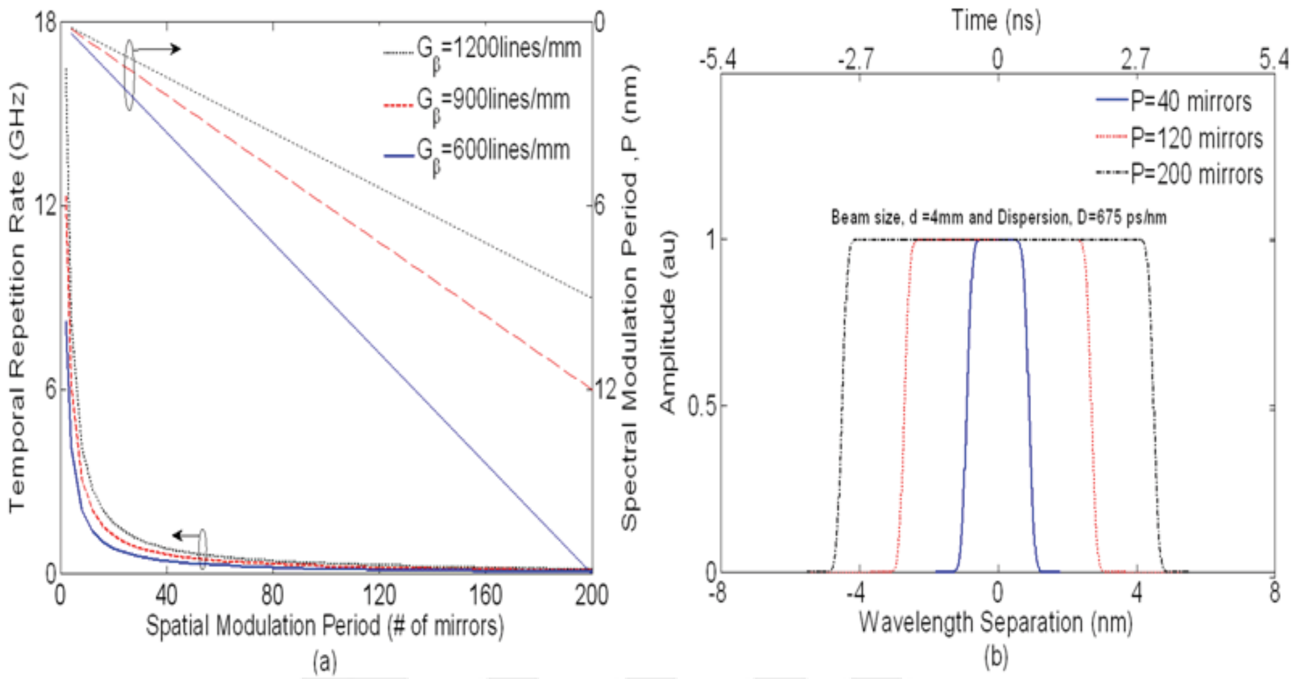

Fig. 4.8 The temporal frequency of the waveforms with respect to spatial modulation period and the effective groove density (a). The analytically generated waveforms for different spatial modulation periods, P (b).

The accuracy and the RF bandwidth of generated waveforms are also affected by the diffraction parameter (r) and the spatial period of the patterns. We analyzed the generated waveforms in terms of the modulation index and the sharpness of the rise/fall edges. The modulation index is defined as $m = (y_{max} - y_{min})/(y_{max} + y_{min})$ and mainly depends on the diffraction parameter (r). For the same spatial modulation frequency, increase in the ratio of the beam size to lens focal length improves the spatial resolution $\Delta x \propto \left(\frac{\lambda f}{d}\right)$ so that the RF waveforms which are the images of the patterns becomes sharper on the edges and higher in modulation index, Figs 4.9(b-d). In addition, for the same diffraction parameter (d/f), decrease in the pattern's spatial period causes the edges to get closer, rounds and thus reduces the modulation index, Figs 4.9(a-c). The minimum spatial modulation period required to obtain a modulation index >90 % is also calculated for each diffraction parameter, Figs 4.9(a-c) [110].

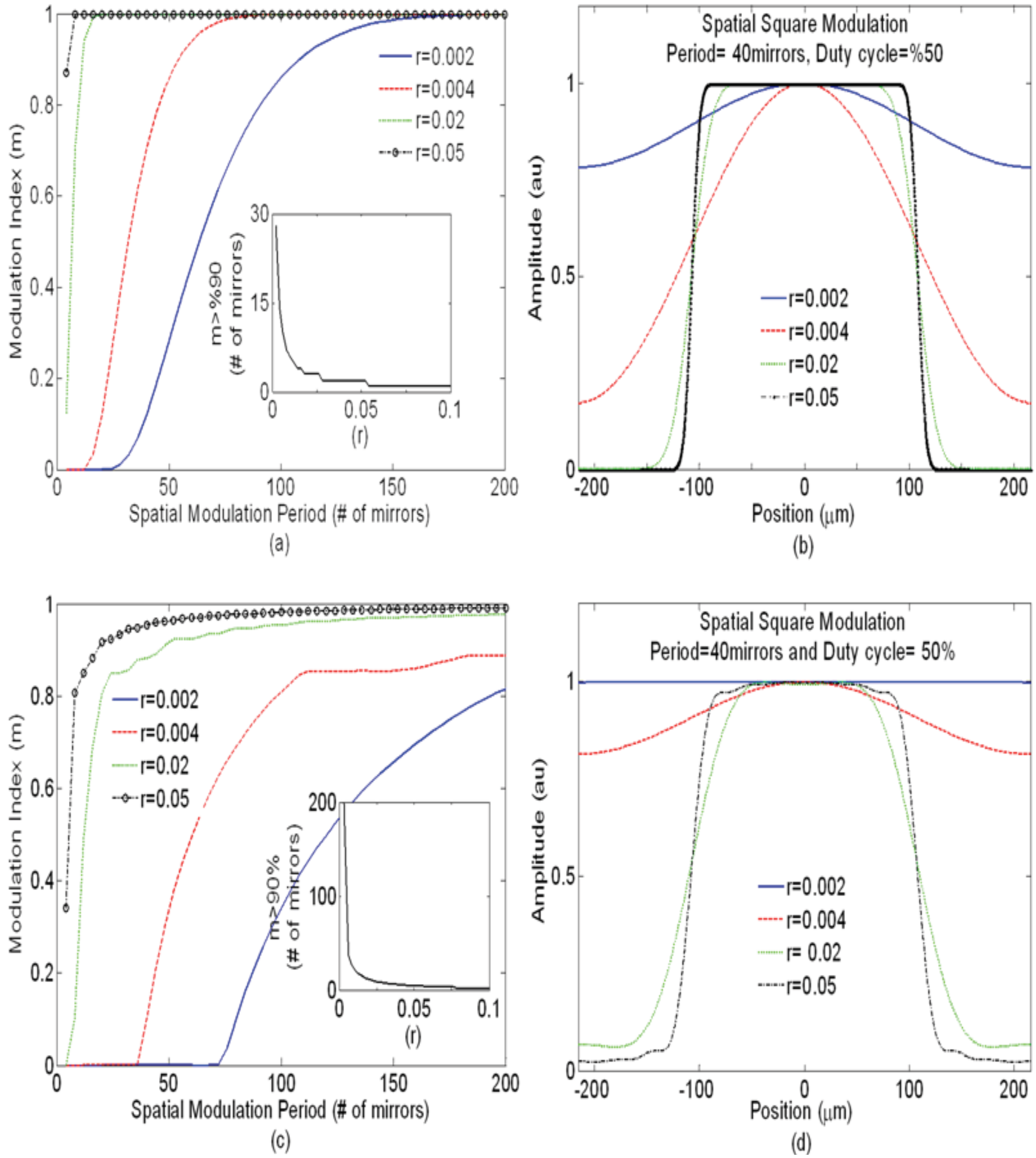

Fig. 4.9 The modulation index(m) due to spatial modulation period and diffraction parameter (r) for both Gaussian (a) and Plane (c) beams. The inset figures shows the required modulation period to obtain m>90%. The generated waveforms (b-d) for different diffraction parameters (r).

The other key concept to evaluate the characteristics of the generated waveforms is the maximum achievable RF bandwidth, namely the sharpness of the rise/fall edges. The spectral ($\delta\lambda_R$) or the temporal (τ_R) rise refers to the increment required for a waveform to change from a specified low value (10%) to a specified high value (90%). As the spatial modulation period increases, the rounding effects disappear, the edges become clearer and the edge slope becomes constant, Figs. 4.10(a-c). The actual rise/fall time can be improved by increasing the beam size, d (the effect of the lens focal length is almost negligible) and by using gratings with higher groove density (G), Figs 4.10(b-d) [110].

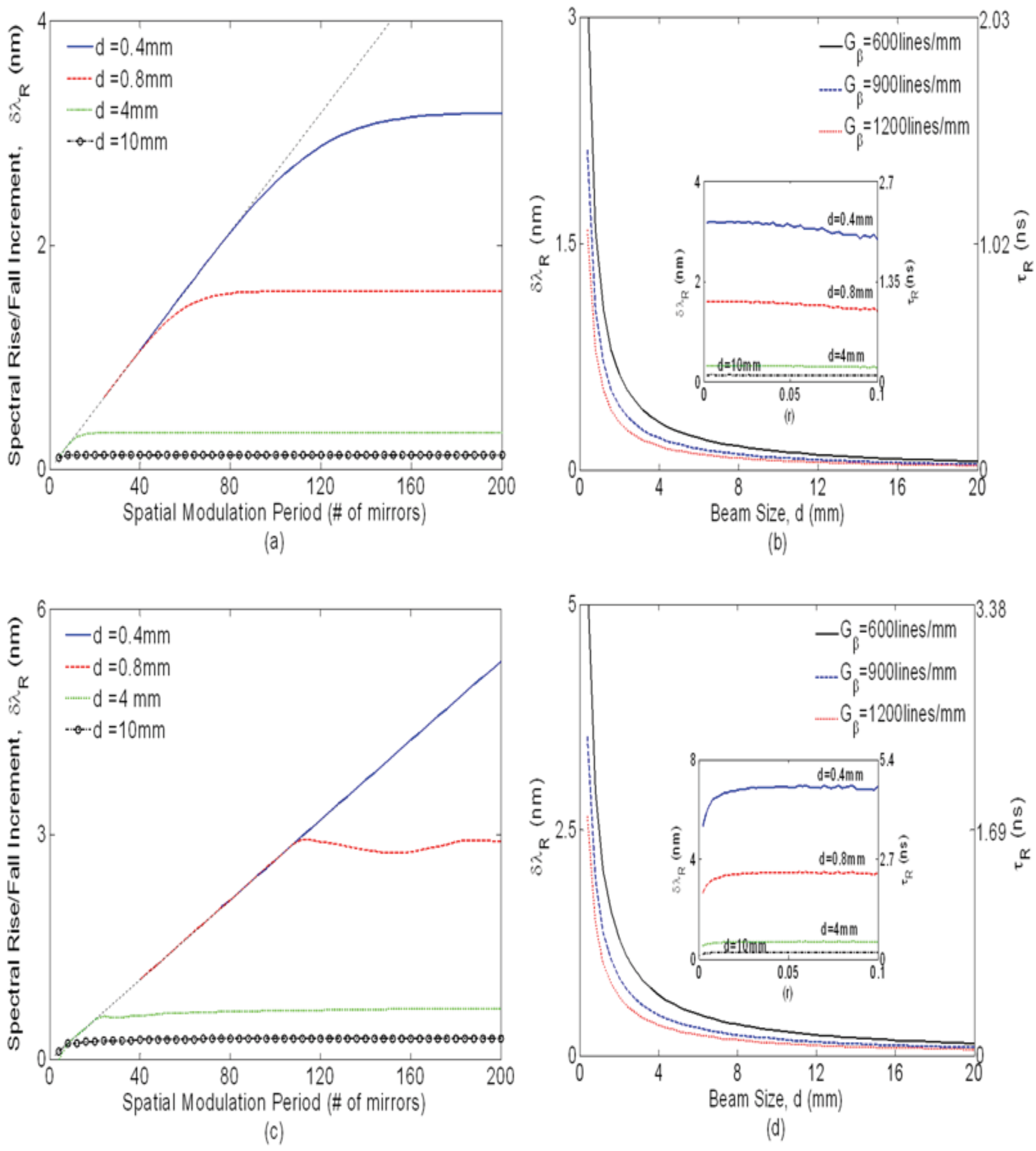

Fig. 4.10 The spectral ($\delta\lambda_R$) and the temporal (τ_R) rise at the waveform edges due to spatial modulation period (a-c) and the beam size (b-d) for Gaussian and Plane beams, respectively. The inset figures show the effect of lens focal length on $\delta\lambda_R$ and τ_R.

b. Sawtooth Waveform Generation

The DMD can display both binary and grayscale images with high frame rates. Contrary to binary images for which the micro mirrors are only assigned to either ON or OFF states, to achieve grayscale images, however, requires fast switching of the mirrors between two binary states by properly adjusting the percentage of the time the mirror is at ON state during the refresh time. The DMD chipset used in this experiment can be refreshed up to 5kHz (200μs refresh time) and 500Hz (2ms refresh time) for binary and grayscale (up to 8bits, 256 levels, toning) images, respectively [106]. However, since the temporal window (temporal width of the SC pulses) to catch the pattern modulation is much shorter than the DMD refresh time, it disables to utilize the averaging of dynamic patterns. Thus, static assignment of the micro mirrors can only be used for the waveform generation. On the other hand, to enable amplitude modulation or to generate complex waveforms such as sawtooth or triangle, which includes grayscale amplitudes, special patterns has to be created. Two different approaches have been proposed to create appropriate binary patterns to achieve grayscale modulation.

In the first approach, the two dimensional mapping/modulation capability of DMD via 1024 X 768 individually addressable digital micro mirror arrays is proposed to accomplish amplitude quantization. To enable 2D modulation, spatially dispersed and collimated beam (considered as 1D wavelength to space mapping) has to be expanded to illuminate a sufficient area over the DMD. Through assigning the mirrors in horizontal direction for the temporal sampling and the mirrors in the vertical direction for the amplitude quantization, it is possible to generate complex waveforms by adjusting the number of vertical ON state mirrors accordingly to set the quantization levels, Fig 4.11 [110].

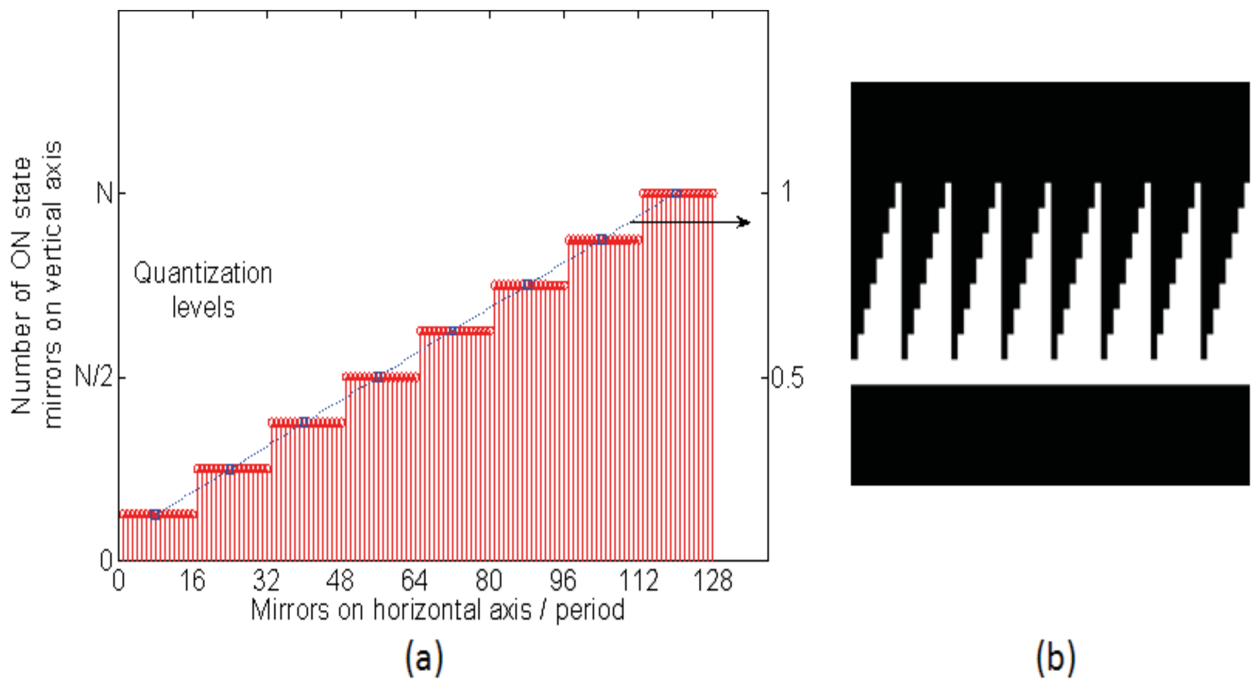

Fig. 4.11 The 2-D amplitude quantization model for sawtooth waveform generation. The sample modulation scheme employed on DMD with 128 horizontal mirrors/period and 8 amplitude quantization levels (a). The sample binary image pattern with 128 horizontal mirrors/period and 320 vertical mirrors (40 mirrors /each level) created on DMD to generate sawtooth waveform (b).

In the second approach, using so called pulse width modulation among the combined group of mirrors enables one dimensional amplitude quantization. The pre-defined modulation period (in terms of the pixels/mirrors), is divided into sub-periods to define each quantization level for which the number of the mirrors at ON state is set accordingly, Fig 4.12(a). The binary image patterns created due to second approach similar to the sample shown in Fig 4.12(b) are used in the experiment to generate the sawtooth waveforms with varying spatial period [110].

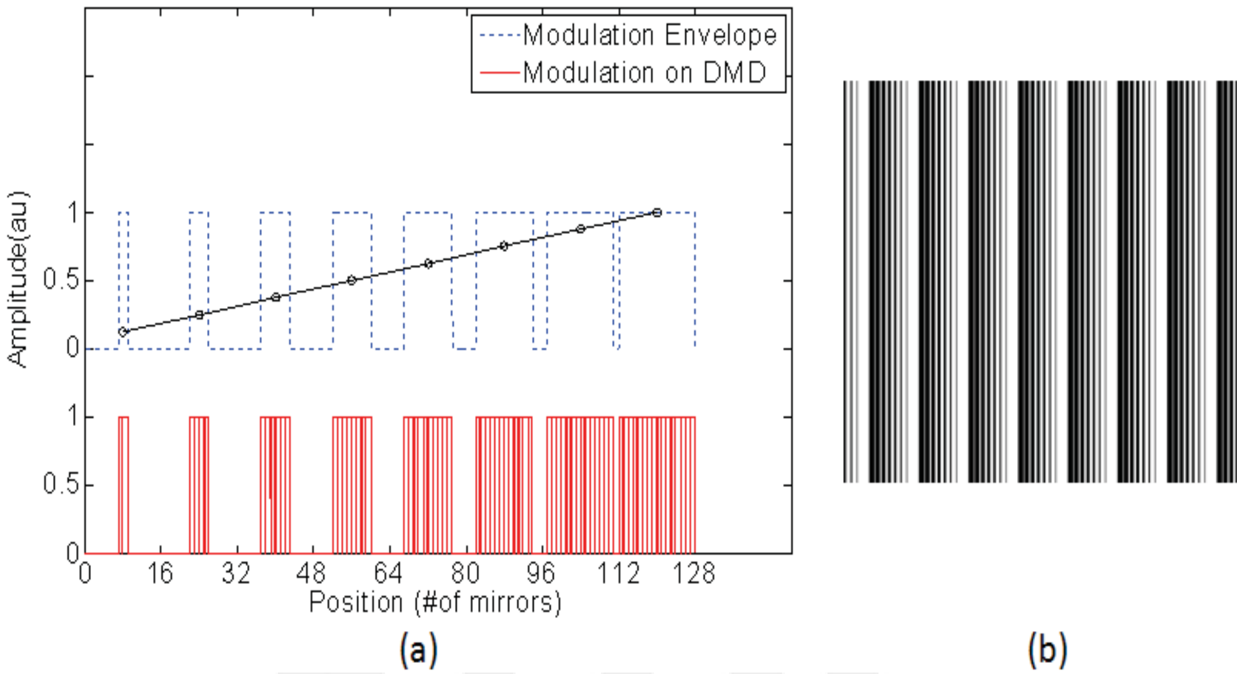

Fig. 4.12 The so-called pulse width modulation model for sawtooth waveform generation. The sample modulation scheme employed on DMD with 128 mirrors/period and 8 amplitude quantization levels (a). The sample binary image pattern with 128 horizontal mirrors/period created on DMD to generate sawtooth waveform (b).

4.4. Experimental Setup and Results

The experimental setup illustrated in Fig 4.14 is used to demonstrate DMD based optical AWG system [110-112]. Supercontinuum pulses are generated to provide broadband source by propagating the Mode Locked Laser pulses (at 1550nm with <1ps pulse width and 20MHz repetition rate) through the amplifier (EDFA: Erbium Doped Fiber Amplifier) and the cascaded single mode (SMF), dispersion shifted (DSF) and nonlinear fiber (NLF) patch cords [120]. Band pass filter (CWDM: Coarse Wavelength Division Multiplexing) centered at 1590nm is used to carve out ~20nm nearly-flat portion of the spectrum, Fig 4.13.

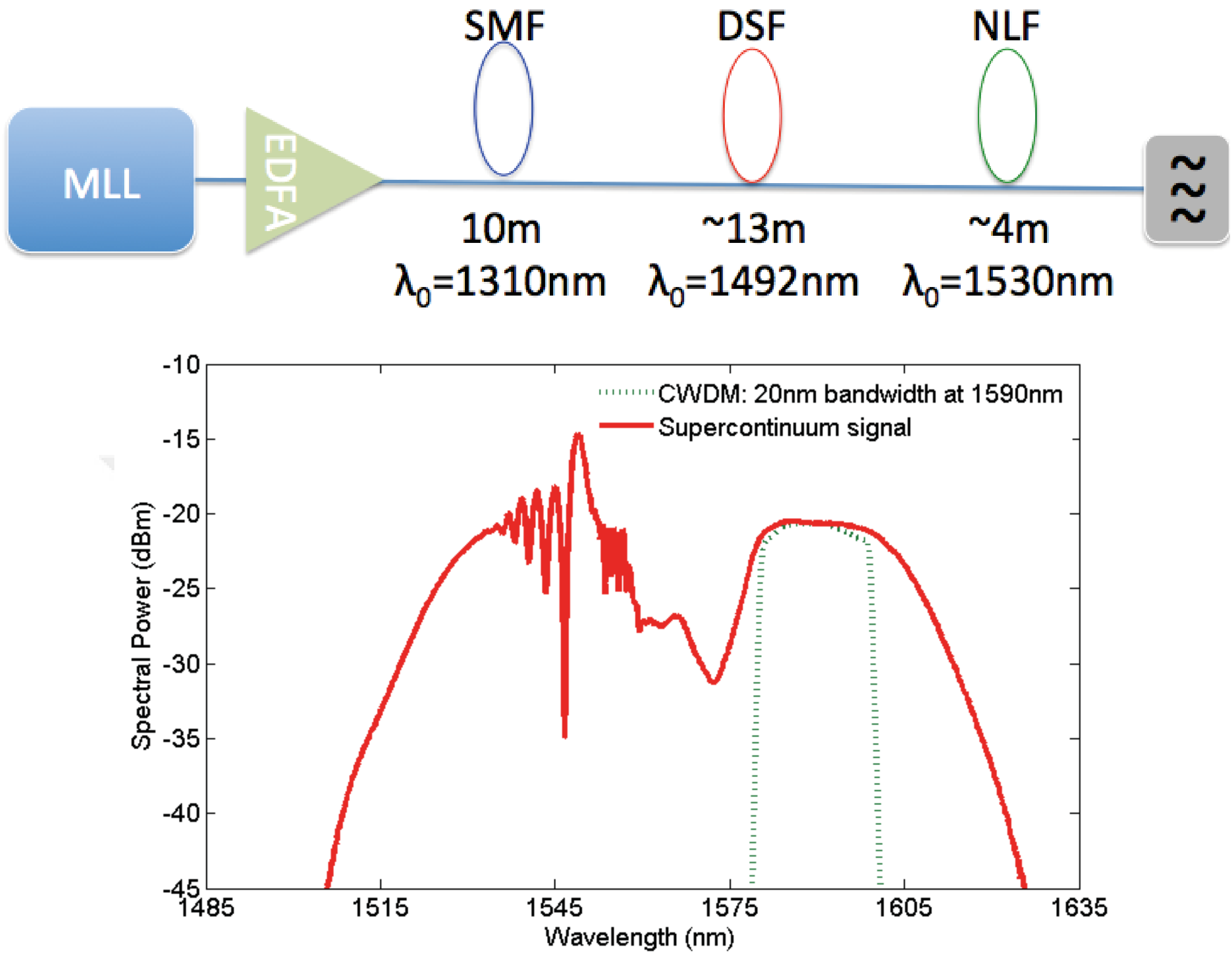

Fig. 4.13 The setup for supercontinuum pulse generation and the achieved broadband spectrum of the pulses. The nearly flat portion (20nm centered at 1590nm) is carved out by CWDM.

Generated SC pulses are then wavelength-to-time mapped through the dispersion compensation module (DCM with -675ps/nm) for real time detection. The optical pulses, on the other hand, are highly attenuated while passing through the system. The system losses are mainly due to the DCM (~2.1 dB insertion loss) and the DMD which induces single pass attenuation of ~45% by considering the beam wavelength (1590nm), micro-mirror reflectivity (~90%), active area (~90%), diffraction efficiency (%88) and the transmission of the protective cover glass on the micro mirrors (~90% if coated for NIR and ~75% if coated for visible) [109]. In order to compensate the system losses and to obtain a better signal to noise ratio, a flat gain Raman amplifier is designed to provide a uniform amplification through the DCM. The Raman amplification with ~10dB net gain and <0.5dB gain ripple is introduced by using four pump laser diodes at different wavelengths (1450nm, 1470nm, 1490nm and 1505nm) in a hybrid pumping configuration. Amplified and temporally stretched broadband pulses (collimated beam with a Gaussian profile having ~0.87mm beam diameter) are spatially dispersed by blazed grating (600lines/mm) and collimated on to the DMD (1024x768 mirror array) by the first cylindrical lens (L1: f=200mm). Since the pulses are stretched in time, namely a dispersive Fourier transform by the DCM, the DMD induced spatial modulation on the spectral domain are mapped into the temporal. The spectrally and temporally modulated pulses are then focused by the second spherical lens (L2: f=30mm) in to the photo detector (>1.2GHz bandwidth). The detector is placed through the mirrors' ON state direction, which is connected to real time storage oscilloscope with 8GHz bandwidth [110-112].

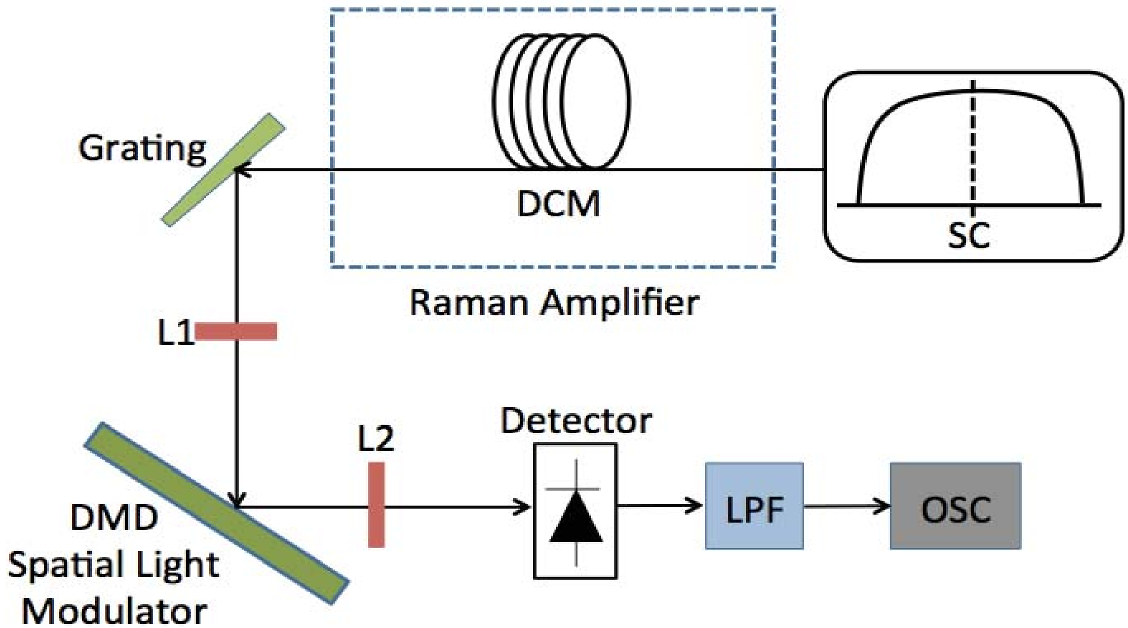

Fig. 4.14 The experimental setup of all optical arbitrary waveform generator (AWG). MLL: Mode locked laser, EDFA: Erbium doped fiber amplifier, SC: Supercontinuum, BPF: Band pass filter.

The DMD chipset used in the experiment is protected by a cover glass, which is anti-reflective (AR) coated for visible light. Under broadband and near infrared (NIR) illumination, a strong interference results from the Fabry Perot effect between the micro-mirrors and the cover glass. This spectral interference transforms to a temporal modulation of ~1.8GHz through the DCM (-675ps/nm) [111]. As a result, a low pass filter with 1GHz cut-off is used after the detector to eliminate this undesired interference. The detected unmodulated signal in which all the mirrors are assigned to ON state (white image pattern) and the etalon induced interference which occurs at ~1.8GHz are illustrated in Fig 4.15.

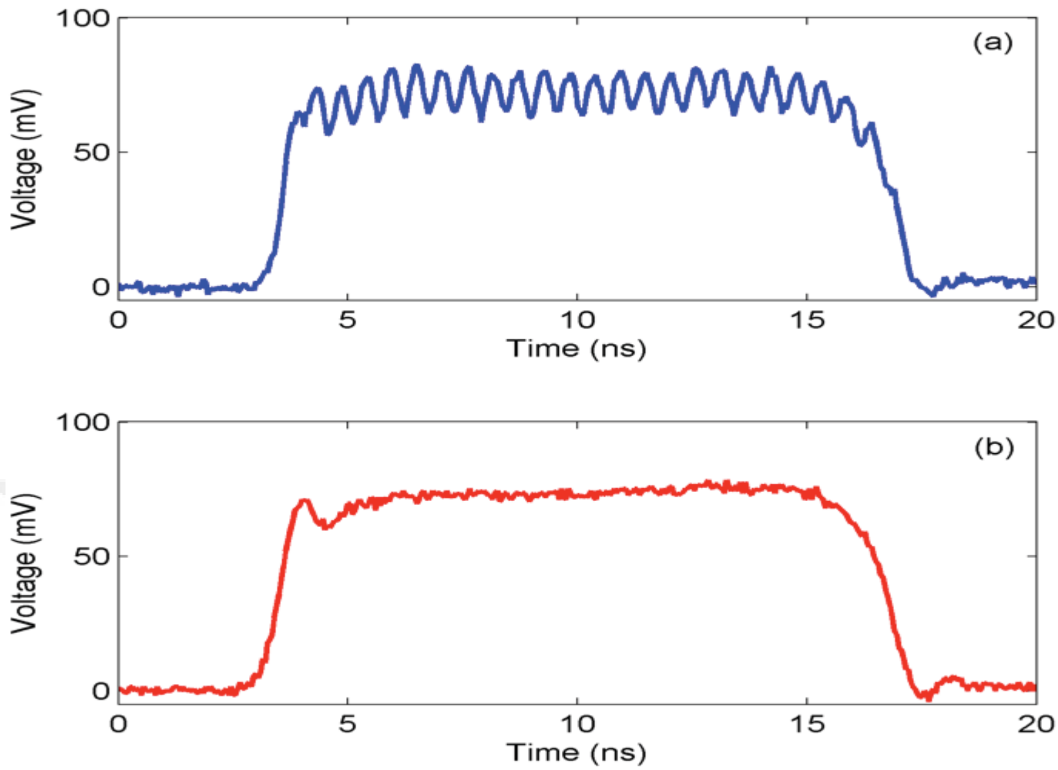

Fig. 4.15 The detected unmodulated signal (a) with ~1.8GHz etalon induced interference (a). Low pass filter at 1GHz is used to eliminate this undesired interference (b).

As illustrated in Fig 4.16, square waveforms with frequency ranging from 120MHz to 580MHz are generated for the proof of concept demonstration [111]. Due to the spatial resolution of the optical system, as the pattern modulation frequency increases, the waveforms approximates to sinusoidal rather than square wave due to the rounding of the edges, Fig 4.16(a-b). Increasing the spatial period of the patterns, namely exceeding the diffraction limit, results in a higher temporal modulation index and enables to achieve desired waveforms with high accuracy in terms of the shape and the fine features, Fig 4.16(c-d).

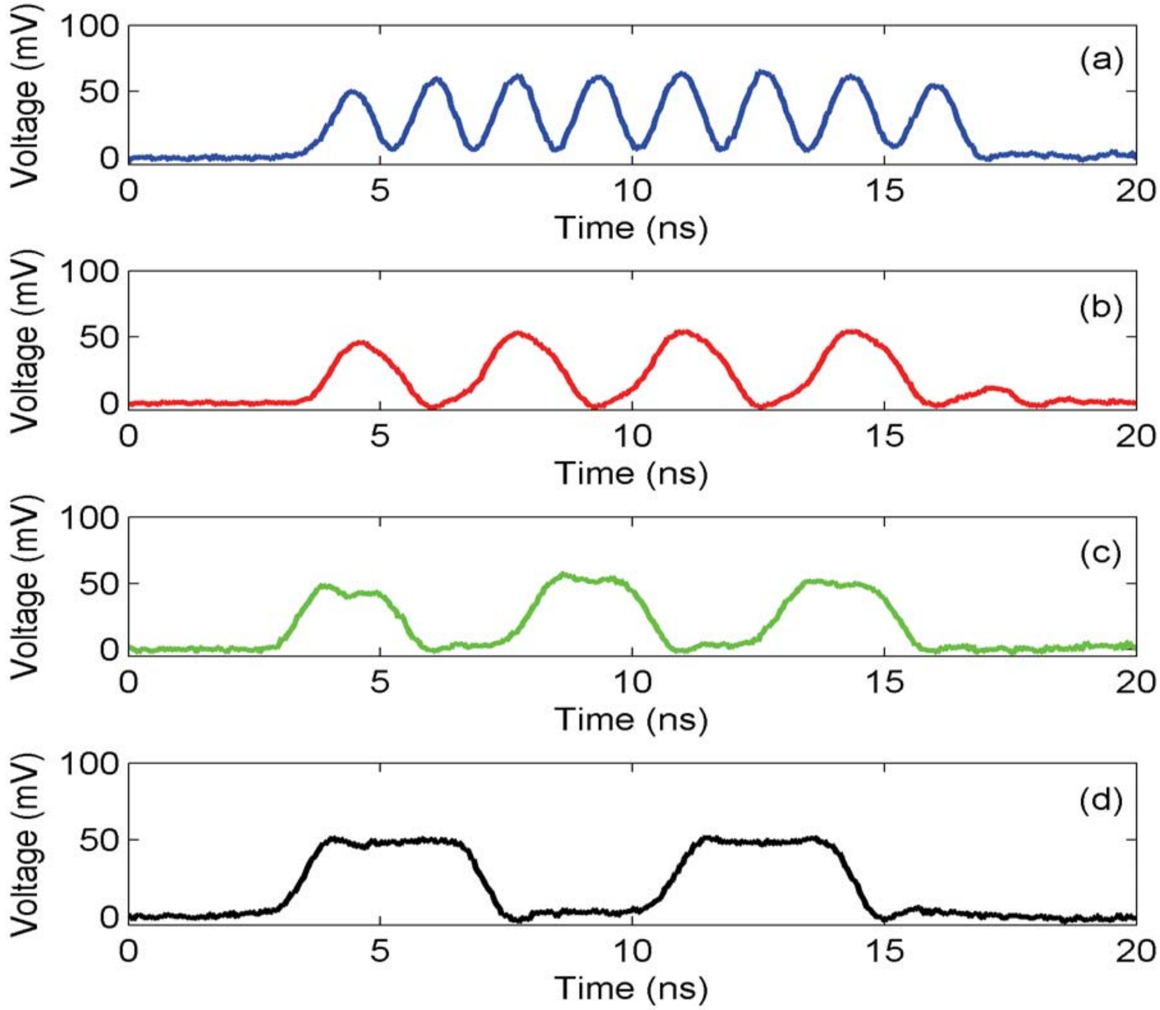

Fig. 4.16 The generated square waveforms with repetition rates of 580MHz(a), 300MHz(b), 200MHz(c), and 120MHz(d).

We have implemented second approach of amplitude quantization mentioned in previous section to generate a sawtooth waveform, a complex waveform including gray scale levels, similar patterns shown in Fig 4.7(b) are used. As illustrated in Fig 4.17, three different sawtooth waveforms with frequency of 280MHz (a), 160MHz (b) and 120MHz (c) are generated for demonstration [111]. The relative position of the spatial window of the space-wavelength mapping over the DMD pattern may cause irregularities such as the shearing and fading at the ends of the temporal window (Δτ≈Δλ*dispersion≅13.5ns) in which the RF waveforms are generated.

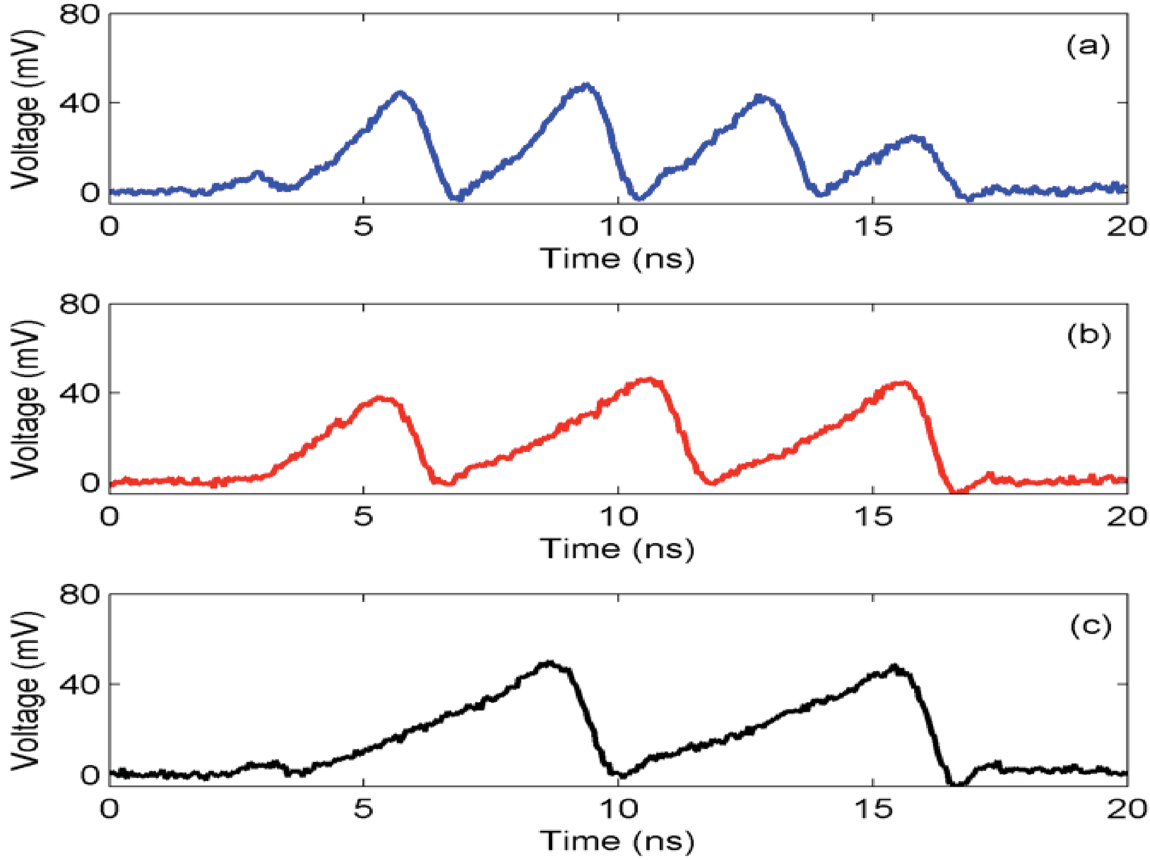

Fig. 4.17 The generated sawtooth waveforms with repetition rates of 280MHz (a), 160MHz (b) and 120MHz (c).

In addition, to test our analytical modeling we have experimentally generated another set of square and sawtooth waveforms. The DMD is loaded with the appropriate patterns, similar to Fig.4.7 and Fig.9b, with 180mirrors/period and 162 mirrors/period for square and sawtooth waveform generation, respectively [110]. The experimentally and analytically generated square and the sawtooth waveforms are illustrated to demonstrate the concept and the correctness of the analytical model, Fig 4.18.

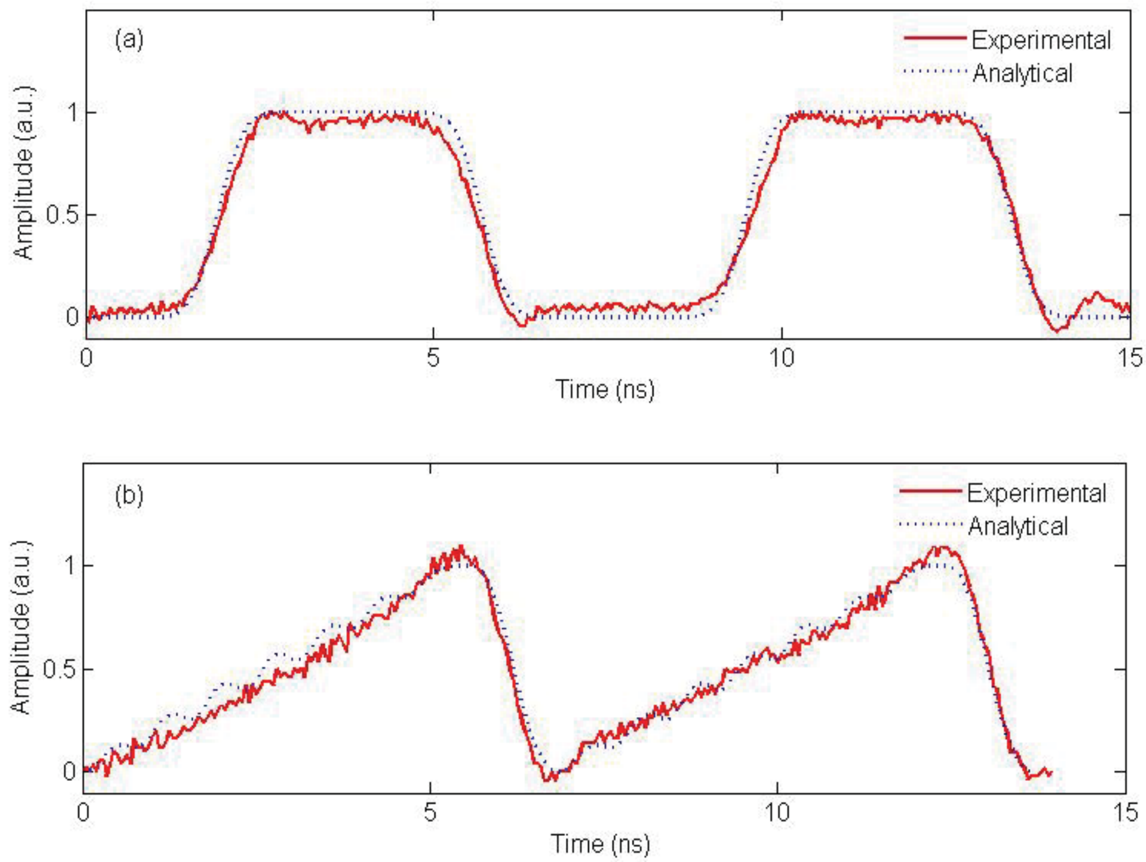

Fig. 4.18 The analytical and experimental results for the generated square waveform at 120MHz (a) and for the sawtooth waveform at 160MHz (b).

The weak high frequency modulation appears on the analytically generated sawtooth waveform (b) results from the individual square type modulation of the sub-periods of the pattern used to generate sawtooth waveforms (Fig 4.12). In addition, using LPF to eliminate the Fabry Perot interference between to cover glass and the mirrors limits the maximum detectable frequency bandwidth to 1GHz with ~1ns rise/fall time. By using a suitable cover glass which is AR coated for near infra red (NIR) illumination and high speed detectors enables to catch the higher harmonics so that increases the temporal resolution and hence the smearing of the fine details of the arbitrary waveforms can be avoided. These weak modulations, as a result, on the sawtooth waveform and the sharp edges of the square waveform are slightly smoothened due to the 1GHz LPF used in the experimental setup.

4.5. Conclusion

A new approach for all optical AWG is proposed by using MEMS based micro mirror arrays as a digital spatial light modulator. I described the procedure that is used in AWG in detail and provide analytical modeling. Additionally, I discuss the limits of the proposed technique based on currently available digital mirror technologies. As a performance criteria, the achievable temporal frequency, modulation index and the maximum frequency bandwidth of the modulated waveforms are investigated for such different optical system parameters as the beam size, lens focal length, effective groove density and the spatial modulation frequency. The results indicates that reducing the diffraction limit via increasing the ratio of beam size to lens focal length (>0.075) and spatial modulation down to single mirror pitch size (10.8μm), waveforms up to 18GHz repetition rates with >90% modulation index and <100ps rise/fall times can be achievable by utilizing -675 ps/nm dispersion. The system temporal performance mainly depends on the dispersive unit and can be improved proportionally with the amount of dispersion.

Using an initial experimental setup, we demonstrate 120MHz to 280MHz sawtooth and 120MHz to 580MHz square waveforms that are controlled by a 1024x768 mirror arrays. Additionally, another set of 160MHz sawtooth and 120MHz square waveforms are obtained and compared with analytical counterparts to illustrate the agreement with the analytical estimates. Based on the state of the art MEMS digital mirror technology, it is estimated that waveforms with 1GHz rate reconfigurable in ~30μs are achievable by using proposed approach. By compensating for the system non-idealities such as the non-uniformity of SC source and the system distortions through the patterns fed into the mirrors and by using an effective feedback algorithm, the system would converge to high accuracy waveforms with minimum achievable error.

Conclusion

This dissertation describes the dispersive and nonlinear interactions in optical fibers and analytical and numerical studies on for synchronous pulsed Raman laser up to second order in dispersion managed system. This dissertation further includes a theoretical and experimental investigation of the noise performance of time stretched systems with discrete and distributed amplifiers. Finally, this dissertation presents the spatiotemporal system incorporated with mature MEMS digital micro mirror technology for the all-optical arbitrary waveform generation.

Chapter 2 of this dissertation discusses the stability of dispersion managed (DM) synchronous Raman lasers up to second order both analytically and numerically. The variational analysis was conducted in order to derive the differential equations that explain the intracavity dynamics of Stokes pulses in terms of their pulse parameters. The resulting coupled differential equations with periodic boundary conditions are solved to obtain the Stokes pulse parameters at the steady state. The analytically and numerically derived pulse parameters of the Stokes pulses are compared to illustrate the correctness of the analytical predictions. The results show that stable second order Raman Stokes pulses with 0.02W to 0.1W peak power and 1ps to 2.1ps pulse widths can be achieved in a DM Raman laser system. The future works should be focused on optimizing the parameters of the dispersion management and designing complex dispersion managed systems for high order laser generation.

Chapter 3 of this dissertation discusses the noise performance and hence the signal to noise ratio (SNR) performance of time stretch ADCs with distributed and lumped amplifications. Erbium doped fiber amplifier (EDFA) and Raman amplifier is thought for the lumped and distributed amplification, respectively. All the major noise components mainly due to amplifiers such as the amplified spontaneous noise (ASE), relative intensity noise (RIN), double Rayleigh backscattering noise (DRB), and due to detection system as the shot noise, the thermal noise and the quantization noise are investigated individually. I conclude that the time stretch system with distributed amplification is limited by RIN transfer and discrete amplification system is limited by ASE noise. In addition, since the noise is mainly accumulated at low frequencies, using high pass RF filtering improves the SNR performance. Eventually, I estimate that distributed amplification in time stretch system with >10GHz analog bandwidth exhibit up to 16dB higher SNR corresponding to ~2.5 bit higher resolution. In future, the Raman gain optimization of the system can be extended to include the additive noise terms to achieve high SNR time stretched system.

Chapter 4 of this dissertation discusses a novel technique for all optical arbitrary waveform generation (AWG) by using MEMS based 1024x768 micro mirror arrays, which constitute a preferable alternative for digital spatial light modulator providing extremely faster switching speeds (<30μs) between different types of modulation patterns, excellent stability, higher diffraction and power transfer efficiency and feasibility for wide range of wavelengths (UV to NIR). I described the detailed procedure and provide an analytical modeling to discuss the limits of the proposed technique in terms of the frequency, the modulation index and the RF bandwidth which mainly depend on the spatial (diffraction limited) and the spectral resolution of space-to-wavelength mapping and the spatial modulation. The results indicate that reducing the diffraction limit, using more powerful gratings and increasing the spatial modulation frequency. The system temporal performance mainly depends on the dispersive unit and can be improved proportionally with the amount of dispersion. Additionally, an experimental generation of 200MHz square and 280MHz sawtooth waveforms at different frequencies by individually controlling the states of micro mirrors is demonstrated as a proof-of concept. Based on currently available digital mirror technologies, I estimate that 1GHz waveforms reconfigurable in ~30μs are also achievable by using the proposed approach. By compensating for the system non-idealities such as the non-uniformity of SC source and the system distortions through the patterns fed into the mirrors and by using an effective feedback algorithm, the system would converge to high accuracy waveforms with minimum achievable error. The future works should be focused on utilizing the mature DMD technology for wide area fast scanning real-time dispersive imaging applications which is highly desired for biological imaging, surface metrology, micro manufacturing monitoring.

References

[1] R. Ramaswami and K. Sivarajan, Optical Networks: A Practical Perspective, 2nd edition (Morgan Kaufmann Publisher, San Francisco, 2002)

[2] I. P. Kaminov, T. Li, Eds., Optical Fiber Telecommunications, Vols. 4A and 4B (Academic Press, Boston, 2002)

[3] Born, Max; Wolf, Emil (October 1999). Principles of Optics. Cambridge: Cambridge University Press. pp. 14–24. ISBN 0-521-64222-1.

[4] G.P. Agrawal, Nonlinear Fiber Optics 4th edition. (Academic Press 2009)

[5] T. Miya, Y. Terunuma, T. Hosaka and T. Miyashita, “Ultimate low-loss single-mode fiber at 1.55 μm,” Electron. Lett. 15, 106, (1979).

[6] N. Bloembergen, Nonlinear Optics (Benjamin, Reading, MA, 1977), Chap.1.

[7] Y. R. Shen, Principles of Nonlinear Optics (Wiley, New York,1984).

[8] P. N. Butcherand, D. N. Cotter, The Elements of Nonlinear Optics (Cambridge University Press, Cambridge, UK, 1990).

[9] R.W. Boyd, Nonlinear Optics, 2nd edition. (Academic Press 2003)

[10] G. P. Agrawal, in Properties of Glass and Rare-Earth Doped Glasses for Optical Fibers, D. Hewak, Ed. (IEE, London, 1998), pp. 17–21.

[11] R. H. Stolen and C. Lin, “"Self-phase-modulation in silica optical fibers,” Phys. Rev. A **17,** 1448 (1978).

[12] A. Hasegawa and F. Tappert, “Transmission of stationary nonlinear optical pulses in dispersive dielectric fibers. II. Normal dispersion,” Appl. Phys. Lett. 23, 142 (1973).

[13] R. H. Stolen, E. P. Ippen, and A. R. Tynes, “Raman oscillation in glass optical waveguide,” Appl. Phys. Lett. **20,** 62 (1972).

[14] E. P. Ippen and R. H. Stolen, "Stimulated Brillouin scattering in optical fibers," Appl. Phys. Lett. **21,** 539 (1972).

[15] R. G. Smith, “Optical Power Handling Capacity of Low Loss Optical Fibers as Determined by Stimulated Raman and Brillouin Scattering,” Appl. Opt. **11,** 2489 (1972).

[16] C. Lin and R. H. Stolen, "Backward Raman Amplification and Pulse Steepening in Silica Fibers," Appl. Phys. Lett. **29,** 428 (1976).

[17] M. Ikeda, "Stimulated Raman amplification characteristics in long span single- mode silica fibers," Opt. Commun. **39,** 148 (1981).

[18] L. F. Mollenauer, R. H. Stolen, and M. N. Islam, “Experimental demonstration of soliton propagation in long fibers: loss compensated by Raman gain,” Opt. Lett. **10,** 229 (1985).

[19] L. F. Mollenauer, J. P. Gordon, and M. N. Islam, “Soliton propagation in long fibers with periodically compensated loss,” IEEE J. Quantum Electron. **QE-22,** 157 (1986).

[20] K. O. Hill, B. S. Kawasaki, and D. C. Johnson, “Low-threshold CW Raman laser,” Appl. Phys. Lett. **28,** 608 (1976).

[21] R. K. Jain, C. Lin, R. H. Stolen, W. Pleibel, and P. Kaiser, "A high- efficiency tunable CW Raman oscillator," Appl.Phys.Lett.30, 162 (1977).

[22] M. Nakazawa, "Synchronously pumped fiber Raman gyroscope," Opt. Lett. **10,** 193 (1987).

[23] R. Pini, R. Salimbeni, M. Vannini, A. F. M. Y. Haider, and C. Lin, “High conversion efficiency ultraviolet fiber Raman oscillator—amplifier system,” Appl. Opt. **25,** 1048 (1986).

[24] D. Marcuse, Light Transmission Optics (Van Nostrand Reinhold, New York, 1982), Chaps. 8 and 12.

[25] R. R. Alfano (ed.), The Supercontinuum Laser Source (Springer-Verlag, New York, 1989).

[26] B. J. Ainslie and C. R. Day, "A review of single-mode fibers with modified dispersion characteristics," J. Lightwave Technol. **LT-4,** 967 (1986).

[27] D. J. Richardson, R. P. Chamberlain, L. Dong, and D. N. Payne, "A review of single-mode fibers with modified dispersion characteristics," Electron. Lett. **30,** 1326 (1994).

[28] A. H. Gnauck and R. M. Jopson, Optical Fiber Telecommunications III, I. P. Kaminow and T. L. Koch, eds. (Academic Press, San Diego, CA, 1997), Chap. 7.

[29] F. Coppinger, A.S. Bhushan, and B. Jalali, "Time magnification of electrical signals using chirped optical pulses," Electronics Letters 34, 399 (1998)

[30] Y. Han and B. Jalali, "Photonic time-stretched analog-to-digital converter: fundamental concepts and practical considerations," Journal of Lightwave Technology 21, 3085 (2003)

[31] B. Jalali, K. Goda, A. Fard, and S. Kim, "From Analog to Digital Conversion to Blood Screening; Evolution of Photonic Time Stretch," in CLEO:2011 - Laser Applications to Photonic Applications, OSA Technical Digest (CD) (Optical Society of America, 2011), paper CWC3.

[32] P. Kelkar, F. Coppinger, A. S. Bhushan, and B. Jalali, "Time-domain optical sensing," Electronics Letters 35, 1661 (1999)

[33] K. Goda, K. K. Tsia, and B. Jalali, "Serial time-encoded amplified imaging for real-time observation of fast dynamic phenomena," Nature 458, 1145 (2009)

[34] Bahram Jalali, Patrick Soon-Shiong, Keisuke Goda, "Breaking Speed and Sensitivity Limits Real-Time Diagnostics with Serial-Time Encoded Amplified Microscopy," Optik & Photonik, No. 2, 32 (2010)

[35] Bahram Jalali, Daniel R. Solli, Keisuke Goda, Kevin Tsia, Claus Ropers, "Real-time Time-stretch Instruments, Rogue Events, and Photon Economics" The European Physical Journal Special Topics. Vol. 185 (July 2010)

[36] A. M. Weiner, "Femtosecond pulse shaping using spatial light modulators," Rev. Sci. Instrum., 2000, 71, 1929. 53

[37] D. Goswami, "Optical pulse shaping approaches to coherent control," Phys. Rep., 2003, 374, 385.

[38] A. M. Weiner, D. E. Leaird, J. S. Patel and J. R. Wullert, "Programmable femtosecond pulse shaping by use of a multi element liquid-crystal phase modulator," Opt. Lett., 1990, 15, 326.

[39] A. M. Weiner, D. E. Leaird, J. S. Patel, and J. R. Wullert, "Programmable shaping of femtosecond optical pulses by use of a 128-element liquid crystal phase modulator," IEEE J. Quantum Electron. 28, 908–920 (1992).

[40] W. Hillegas, J. X. Hull, D. Goswami, D. Strickland and W. S.Warren, "Femtosecond laser pulse shaping by use of microsecond radio-frequency pulses," Opt. Lett., 1994, 19, 737–739.

[41] M. A. Dugan, J. X. Tull and W. S. Warren, "High resolution acousto-optic shaping of unamplified and amplified femtosecond laser pulses," J. Opt. Soc. Am. B.,1997, 14(9), 2348–2358.

[42] C. Radzewicz, P. Wasylczyk, W. Wasukewsju and J. S. Krasin´ ski, "Piezo-driven deformable mirror for femtosecond pulse shaping," Opt. Lett., 2004, 29, 177–179.

[43] K. Li, U. Krishnamorthy, J. P. Heritage and O. Solgaard, “Coherent micromirror arrays,” Opt. Lett., 2002, 27, 366–368.

[44] M. Hacker, G. Stobrawa, R. Sauerbrey, T. Buckup, M. Motzkus, M. Wildenhain and A. Gehner, “Micromirror SLM for femtosecond pulse shaping in the ultraviolet,” Appl. Phys. B, 2003, 76, 711–714.

[45] G.P. Agrawal, Fiber Optic Communication Systems 3rd edition. (Academic Press 2002)

[46] M.N. Islam, L.F. Mollenauer and R.H. Stolen, “Cross-phase modulation in optical fibers”, Opt. Lett., vol. 12, no. 8, 1987.

[47] B. Washburn, “Numerical Solutions to Nonlinear Schrödinger Equation”. http://www.phys.ksu.edu/personal/washburn/pdf/washburn_thesis_chapter4.pdf

[48] T.E. Murphy, “Soliton Pulse Propagation in Optical Fiber” (2001). http://www.photonics.umd.edu/pubs/misc-presentations/MP-1/solitons.pdf

[49] C.V. Raman, Indian Journal Phys. 2,387 (1928).

[50] E.J. Woodbury and W.K. Ng, “Ruby laser operation in near IR” Proc IRE 50, 2347 (1962).

[51] M. Nakazawa, K. Suzuki, Y. Kimura, “3.2-5 Gb/s, 100km error free soliton transmissions with Erbium amplifiers and repeaters” IEEE Photon. Techno. Lett. 2, 216 (1990).

[52] H.A. Haus, M. Nakazawa, “Theory of fiber Raman soliton laser”, J. Opt. Soc. Am. B/Vol. 4, No. 5, (1987).

[53] H. Rong, S. Xu, O. Cohen, O. Raday, M. Lee, V. S and M. Paniccia, “A Cascaded Silicon Raman Laser”, Nature Photonics 2, 170-174 (2008).

[54] R.H. Stolen, Raman Amplifiers for Telecommunications, Part 1, M.N. Islam, Chap. 2 (Springer 2004).

[55] G. Vareille, O. Audouin, and E. Desurvire, "Numerical optimization of power conversion efficiency in 1480 nm multi-Stokes Raman fiber lasers," Electron. Lett. 34, 675-676 (1998).

[56] D. Hollenbeck, C.D. Cantrell, "Multi-vibrational-mode model for fiber-optic Raman gain spectrum and response function", J. Soc. Am. B/Vol. 19, No. 12 (2002).

[57] Jake Bromage, "Raman Amplification for Fiber Communications Systems," Journal of Lightwave Technology, Vol. 22, Issue 1, pp. 79- (2004).

[58] A. A. M. Staring, L. H. Spiekman, J. J. M. Binsma, E. J. Jansen, T. V. Dongen, P. J. A. Thijs, M. K. Smit, and B.H. Verbeek, "A compact nine-channel multiwavelength laser," IEEE Photon. Technol. Lett. 8, 1139-1141 (1996).

[59] M. Zirngibl, C. H. Joyner, C. R. Doerr, L. W. Stulz, and H. M. Presby, "An 18-channel multifrequency laser," IEEE Photon. Technol. Lett. 8, 870-872 (1996).

[60] M. D. Mermelstein, C. Horn, S. Radic, and C. Headley, "Six-wavelength Raman fiber laser for C- and L-band Raman amplification and dynamic gain flattening," Electron. Lett. 38, 636-638 (2002).

[61] C.J.S. Matos, S.V. Popov, and J.R. Taylor, "Short-pulse, all-fiber, Raman laser with dispersion compensation in a holey fiber," Optics Letters, Vol. 28, Issue 20, pp. 1891-1893 (2003).

[62] C. J. S. De Matos, D. A. Chestnut, P. C. Reeves-Hall, F. Koch, and J. R. Taylor, "Multi-wavelength, continuous wave fiber Raman ring laser operating at 1.55 μm," Electron. Lett. 37, 825-826 (2001).

[63] X. Y. Dong, P. Shum, N. Q. Ngo, and C. C. Chan, "Multiwavelength Raman fiber laser with a continuously tunable spacing," Opt Express 14, 3288-3293 (2006).

[64] J.H.V. Price, K. Furusawa, T.M. Monro, L. Lefort, and D.J. Richardson, "Tunable, femtosecond pulse source operating in the range 1.06–1.33 mm based on an Yb^{3+-}doped holey fiber amplifier," J. Opt. Soc. Am. B 19, 1286-1294 (2002).

[65] M. D. Mermelstein, C. Headley, J.-C. Bouteiller, P. Steinvurzel, C. Horn, K. Feder and B. J. Eggleton., "A High-Efficiency Power-Stable Three-Wavelength Configurable Raman Fiber Laser", in Proc. Optical Fiber Communication Conference (OFC), 2001, paper PD3-1.

[66] M.D. Mermelrtein, C. Horn, Z. Huang, M. Luvalle, X. Routeiller, C. Headley, B.J. Eggleton, "Configurability of a Three-Wavelength Raman Fiber Laser for Gain Ripple Minimization and Power Partitioning", in Proc. Optical Fiber Communication Conference (OFC), 2002, paper TuJ2.

[67] C. Headley, "Configurable multiple-wavelength all-fiber laser for efficient stable Raman amplification", in Proc. Optical Fiber Communication Conference (OFC), 2002, paper TuB1.

[68] X. Normandin, F. Leplingard, E. Bourova, C. Ledere, T. Lopez, L. J. Guerin, D. Bayart, "Experimental assessment of phospho-silicate fibers for three-wavelength (1427 nm, 1455 nm, 1480 nm) reconfigurable Raman lasers", in Proc. Optical Fiber Communication Conference (OFC), paper TuB2.

[69] M. Müller, J. M. Schins, "Imaging the thermodynamic state of lipid membranes with multiplex CARS microscopy", Journal of Physical Chemistry B 106, 3715-3723 (2002).

[70] J. X. Cheng and A. Volkmer, L. D. Book, and X. S. Xie, "Multiplex coherent anti-Stokes Raman scattering micro spectroscopy and study of lipid vesicles," J. Phys. Chem. B 106, 8493-8498 (2002).

[71] T. W. Kee and M. T. Cicerone, "Simple approach to one-laser, broadband coherent anti-Stokes Raman scattering microscopy," Opt. Lett. 29, 2701-2703, (2004).

[72] H.A. Haus and M. Nakazawa, “Theory of the fiber Raman soliton laser,” J. Opt. Soc. Am. B 4, 652-660 (1987).

[73] S.K. Kalyoncu, S. Gao, E.K. Tien, Y. Huang, D. Yildirim, E. Adas. S. Wabnitz and O. Boyraz, “Stability analysis of second order pulsed Raman laser in dispersion managed systems”, Proc. SPIE 8071 (2011).

[74] S. K. Kalyoncu, S. Gao, E. K. Tien, Y. Huang, D. Yildirim, E. Adas, S. Wabnitz, and O. Boyraz, "Stability analysis of pulsed cascaded Raman lasers in dispersion-managed systems," J. Opt. Soc. Am. B **28**, 2812-2819 (2011).

[75] OFS Specialty Photonics Division. http://ofscatalog.specialtyphotonics.com.

[76] C. Antonelli, J. Chen, F. X. Kartner, “Intracavity pulse dynamics and stability for passively mode-locked lasers,” Optics Express, Vol. 15, Issue 10, 5919-5924 (2007).

[77] A. Hook, D. Anderson and M. Lisak, “Effects of cross-phase modulation and pump depletion on Stokes pulse dynamics in stimulated Raman scattering,” J. Opt. Soc. Am. B 6, 1851-1858 (1989).

[78] Bahram Jalali, Keisuke Goda, Ali Fard, and Sang Hyup Kim, "From Analog to Digital Conversion to Blood Screening; Evolution of Photonic Time Stretch," CLEO 2011 Conference, paper CWC3.

[79] Y. Han and B. Jalali, “Photonic time-stretched analog-to-digital converter: fundamental concepts and practical considerations,” Journal of Lightwave Technology 21, 3085 (2003)

[80] Chou, J., Boyraz, O., Solli, D. & Jalali, B. Femtosecond real-time single-shot digitizer. Appl. Phys. Lett. 91, 161105

[81] P. Kelkar, F. Coppinger, A. S. Bhushan, and B. Jalali, “Time-domain optical sensing,” Electronics Letters 35, 1661 (1999)

[82] K. Goda, K. K. Tsia, and B. Jalali, “Serial time-encoded amplified imaging for real-time observation of fast dynamic phenomena,” Nature 458, 1145 (2009).

[83] Bahram Jalali, Patrick Soon-Shiong, Keisuke Goda, "Breaking Speed and Sensitivity Limits Real-Time Diagnostics with Serial-Time Encoded Amplified Microscopy," Optik & Photonik, No. 2, 32 (2010)

[84] K. K. Tsia, K. Goda, D. Capewell, and B. Jalali, “Performance of serial time-encoded amplified microscope,” Optics Express 18, 10016 (2010).

[85] Ozdal Boyraz, Jaeyoun Kim, Mohammed N. Islam, Fred Coppinger, and Bahram Jalali, “10 Gb/s multiple wavelength, coherent short pulse source based on spectral carving of supercontinuum generated in fibers”, IEEE J. Lightwave Tech., 18, 2, pp.1167-2175, 2000.

[86] Encyclopedia of Laser Physics and Technology, “Erbium-doped Gain Media “. http://www.rpphotonics.com/erbium_doped_gain_media.html

[87] S. Konkanen et al., “High Er concentration phosphate glasses for planar waveguide amplifiers”, Proc. SPIE 2996, 32 (1997).

[88] G. P. Agrawal, Raman Amplification in Fiber Optical Communication Systems. (Elsevier Academic Press 2005)

[89] Victor E. Perlin and Herbert G. Winful, ”Optimal design of flat-gain wide-band Raman amplifiers”, IEEE J. Lightwave Tech., 20, 2, pp. 250-254, 2002.

[90] Qun Han, Jiping Ning, Huayong Zhang and Zhiqiang Chen, “Novel shooting algorithm for highly efficient analysis of fiber Raman Amplifiers”, IEEE J. Lightwave Tech., 24, 4, pp. 1946-1952, 2006.

[91] Bernard Widrow and István Kollár, Quantization Noise: Roundoff Error in Digital Computation, Signal Processing. (Cambridge University Press 2008).

[92] C.R.S. Fludger, V. Handerek, “Pump to signal RIN Transfer in Raman fiber amplifiers”, IEEE J. Lightwave Tech., 19, 8, pp. 1140-1148, 2001.

[93] M.D. Mermelstein, C. Headly and J. C. Bouteiller, “Rin transfer analysis in pump depletion regime for Raman fiber amplifiers”, Elect. Lett., 38, 9, pp. 403-405, 2002.

[94] Ping Wan and Jan Conradi, “Impact of double Rayleigh backscatter noise on digital and analog fiber systems”, IEEE J. Lightwave Tech., 14, 3, pp. 288-296, 1996.

[95] Salih K. Kalyoncu, Yuewang Huang, En-Kuang Tien, Enver Adas, Dogukan Yildirim, and Ozdal Boyraz, “Noise Performance of Time Stretch System with Distributed and Discrete Amplifiers”, in Conference on Lasers and Electro-Optics CLEO 2011, paper CTuA7.

[96] L. Mullen, A. Vierina, P. Herczfeld, and V. Contarino, “Application of RADAR technology to aerial LIDAR systems for enhancement of shallow underwater target detection,” IEEE Trans. Microwave Theory Tech. 43, 2370–77 (1995).

[97] B. Jalali, P. Kelkar, and V. Saxena, “Photonic arbitrary waveform generator,” in Proc. 14th Annu. Meeting IEEE Lasers Electro-Optics Soc. 1, 253-254 (2001).

[98] S. Poinsot, H. Porte, J.-P. Goedgebuer, W. T. Rhodes, and B. Boussert, “Continuous radio-frequency tuning of an optoelectronic oscillator with dispersive feedback,” Opt. Lett. 27, 1300–1302 (2002).

[99] T. Yilmaz, C. M. DePriest, T. Turpin, J. H. Abeles, and P. J. Delfyett, “Toward a photonic arbitrary waveform generator using modelocked external cavity semiconductor laser,” IEEE Photon. Technol. Lett. 14, 1608–1610 (2002).

[100] H. Chi and J. Yao, "Symmetrical waveform generation based on temporal pulse shaping using amplitude-only modulator," Electron. Lett. 43, 415–417 (2007).

[101] C. Wang and J. Yao, "Large time-bandwidth product microwave arbitrary waveform generation using a spatially discrete chirped fiber Bragg grating," J. Lightwave Technol. 28, 1652–1660 (2010).

[102] M. Bolea, J. Mora, B. Ortega, and J. Capmany, "Optical arbitrary waveform generator using incoherent microwave photonic filtering," IEEE Photon. Technol. Lett. 23, 618-620 (2011).

[103] J. D. McKinney, D. E. Leaird, and A. M. Weiner, "Millimeter-wave arbitrary waveform generation with a direct space-to-time pulse shaper," Opt. Lett. 27, 1345–1347 (2002).

[104] A. M. Weiner, "Femtosecond optical pulse shaping and processing," Prog. Quantum Electron. 19, 161–237 (1995).

[105] J. Chou, Y. Han, and B. Jalali, "Adaptive RF-Photonic arbitrary waveform generator," IEEE Photon. Technol. Lett. 15, 581-583 (2003).

[106] DLP Texas Instruments, "MEMS DLP Technology - Getting Started," (Texas Instruments 2010).

http://www.ti.com/dlp

[107] I.W. Jung, J. S. Wang, O. Solgaard, "Optical pattern generation using a spatial light modulator for maskless lithography", IEEE Journal of Selected Topics in Quantum Electronics, 13, 147-154 (2007).

[108] D. Dudley, W. Duncan, J. Slaughter, "Emerging Digital Micromirror Device (DMD) applications," Proc. SPIE 4985, 14-25 (2003).

[109] S.K. Nayar, V. Branzoi, T. E. Boult "Programmable imaging using a digital micromirror array," In Proc. of IEEE Conference on Computer Vision and Pattern Recognition (CVPR) I, 436–443 (2004).

[110] S. K. Kalyoncu, Y. Huang, Q. Song and O. Boyraz, "Analytical study on arbitrary waveform generation by MEMS micro-mirror arrays", Optics Express, Vol.20, No. 25 (2012).

[111] S.K. Kalyoncu, Y. Huang, Q. Song and O. Boyraz, "Fast arbitrary waveform generation by using digital micro mirror arrays," IEEE Photonics Conference, paper TuK 4, San Francisco, Sept. 2012.

[112] S. K. Kalyoncu, Y. Huang, Q. Song and O. Boyraz, "Fast arbitrary waveform generation by using digital micro mirror arrays," (To be Appear In IEEE Photonics Journal).

[113] L. J. Hornbeck, "Digital light processing: a new MEMS-based display technology," in Technical Digest of the Institute of Electrical Engineers of Japan 14th Sensor Symposium (The Institute of Electrical Engineers of Japan, Tokyo, 1996), pp. 297–304.

[114] L. J. Hornbeck, ''Digital light processing for high-brightness, high- resolution applications,'' Proc. SPIE 3013, 27 – 40 (1997).

[115] DLP Texas Instruments, "DMD 101: Introduction to Digital Micromirror Device (DMD) Technology," (Texas Instruments 2008).
http://www.ti.com/lit/an/dlpa008/dlpa008.pdf

[116] DLP Texas Instruments, "Application Report: DLP System Optics," (TI 2010).
http://www.ti.com/lit/an/dlpa022/dlpa022.pdf

[117] DLP Texas Instruments, "The Digital Micromirror Device A Historic Mechanical Engineering Landmark", (Texas Instruments 2008).
http://files.asme.org/asmeorg/Communities/History/Landmarks/14607.pdf

[118] R. S. Nesbitt, S. L. Smith, R. A. Molnar and S. A. Benton, "Holographic recording using a digital micromirror device," Proc. SPIE 3637, 12-20 (1999).

[119] M.L. Hsieh, "Modulation transfer function of Digital Micromirror Device," Optical Eng. 45, 034001-5 (2006).

[120] O. Boyraz, J. Kim, M. N. Islam, B. Jalali, "10 Gb/s multiple wavelength, coherent short pulse source based on spectral carving of supercontinuum generated in fibers," Journal of Lightwave Technol. 18, 2167-2175 (2000).